PSFC/RR-04-01 DOE-ET-54512-349

Study of Recycling Impurity Retention in Alcator C-Mod

Taekyun Chung

August 03, 2004

Plasma Science and Fusion Center
Massachusetts Institute of Technology
Cambridge, MA 02139 USA

This work was supported by the U.S. Department of Energy, Cooperative Grant No. DE-FC02-99ER54512. Reproduction, translation, publication, use and disposal, in whole or in part, by or for the United States government is permitted.

Study of Recycling Impurity Retention in Alcator C-Mod

by

Taekyun Chung

M.S., Nuclear Engineering, Seoul National University, Korea (1997)

Submitted to the Nuclear Engineering Department
in partial fulfillment of the requirements for the degree of

Doctor of Philosophy in Applied Plasma Physics

at the

MASSACHUSETTS INSTITUTE OF TECHNOLOGY

September 2004

Author .....
Nuclear Engineering Department
Aug. 5, 2004

Certified by .....
Ian H. Hutchinson
Professor, Head of Department of Nuclear Engineering
Thesis Supervisor

Certified by .....
Bruce Lipschultz
Senior Research Scientist, Plasma Science and Fusion Center
Thesis Supervisor

Accepted by .....
Professor Jeffery A. Coderre
Chairman, Department committee on Graduate Students

Study of Recycling Impurity Retention in Alcator C-Mod

by

Taekyun Chung

Submitted to the Nuclear Engineering Department
on Aug. 5, 2004, in partial fulfillment of the
requirements for the degree of
Doctor of Philosophy in Applied Plasma Physics

Abstract

This work was aimed at reproducing experimental results in impurity compression of Ar, as well as the screening of recycling and non-recycling impurities from reaching the core plasma. As part of the study the code was upgraded in order to track the impurity flow from source till it reaches the core, include the energy dependence on recycled impurity atoms, and allow for more realistic impurity recycling in the SOL. This added capability allows the determination of which source locations are dominant in determining the core impurity level, where they cross the separatrix into the core and where they leave the core.

The modeling reproduces within a factor of 2 the experimentally observed compression of Ar in the divertor of Alcator C-Mod. In addition it was found that under attached conditions recycling at the outer plasma edge (limiters located there) was the dominant source of Ar ions reaching the core (over 60%). For detached conditions divertor recycling replaces the outer edge in supplying the majority of Ar ions reaching the core. There appear to be two general flow patterns of impurities through the core plasma: Outboard launched impurities enter the core at the outside edge and flow out of the core on the inboard edge; Divertor launched impurities enter the core just outboard of the x-point and return to the divertor just inboard of the x-point.

The study of non-recycling impurities was also carried out and it was found that the penetration factor (PF) for outboard-launched impurities (Carbon was used as the prototype) were a factor of 3 times more likely to reach the core than inboard-launched impurities (experimental result gave the ratio as 20). Increasing the background SOL plasma flow to the experimental levels doubles the model ratio and other factors capable of reducing the discrepancy are studied. Thus the experimental poloidal variation in PF is qualitatively reproduced. Values of PF for recycling impurities (a global quantity) matched the experimental magnitudes when experimental values for SOL flow were used.

Thesis Supervisor: Ian H. Hutchinson
Title: Professor, Head of Department of Nuclear Engineering

Thesis Supervisor: Bruce Lipschultz
Title: Senior Research Scientist, Plasma Science and Fusion Center

Acknowledgments

Trust in the Lord with all your heart and lean not on your own understanding;
in all your ways acknowledge HIM and HE will make your paths straight.
(Proverbs 3:5-6)

Every moment whether it was joyful or full of grief, my Father in Heaven was always with me. He had filled every single moment with His unfathomable love and blessing. To every person that He allowed me to meet with, I would like to express my deepest gratitude. First I would like to thank Professor Ian Hutchinson and Dr. Bruce Lipschultz for their supervising my thesis with patience and generosity. The ability to diagnose what I don't understand and what I'm in lack of is the most precious thing I've obtained from their teachings. I'm obliged to say thank you to my former advisor Dr.Spencer Pitcher. I can not forget his encouragement and kindness. Prof. Peter Stangeby and Dr. David Elder in Univ. of Toronto helped me to learn the code.

I want to thank many colleague students. My senior colleague, Yongkyoon In always showed his care, love, and advice on my life in this foreign land. Maxim Umansky was really a good friend to me. I profitted tremendously from discussions, co-works, even casual conversations with fellow graduate students; Chris Boswell, Howard Yuh, Jerry Hughes, Sanjay Gangadhara, Khashayar Shadman and Jinseok Ko. I specially thank to John Liptac for his commitment to proof-reading my thesis.

My family was the source of energy, driving force and motiviation when I was out of breath. Love and sacrifice that my parents show me through my life over thirty years are indeed what I am and what I have at present. How can I thank too much for the trust, patience, lavish support from my father and mother-in-law! I could not have made even an inch of progress without support from my wife, Heejin. She is my strength and hope when I'm exhausted and in despair. Her persistent praying lets me stand tall. I dedicate this thesis to my beloved other-half, Heejin. Finally I wish that this thesis should be a pride to my daughter, Janice, some day in the future.

Contents

List of Figures

Chapter 1

Introduction

The energy source required for sustaining life on earth comes from the sun. The sun sustains itself burning by fusion reactions of protons confined by gravity. The *self-sustaining* nature of the sun was the motivation of fusion research launched about a half century ago as a promising method for the electricity production. Since the beginning, the fusion research has achieved outstanding progress in spite of many challenges. This chapter will review briefly fusion, the tokamak (fusion reactor) and the outline of thesis including the goals of the study.

1.1 Fusion

Fusion is the atomic reaction which combines two light nuclei into heavier nucleus releasing energy in the form of the kinetic energy of the fusion reaction products. Compared to other methods (e.g. burning fossil fuels) for electricity production, fusion has attractive advantages which make fusion a promising energy solution. First, fusion taps very high density of energy compared to the conventional fossil energy : 1 gram of deuterium fuel in fusion produces equivalent amount of energy which 6,000 liters oil produces. Secondly, the abundance in fuel. The fuel abundance is a critical issue to conventional fossil power plant. Fusion is able to resolve this problem as it uses as fuel the hydrogen isotopes (e.g. D and T) which can be extracted from the sea water(H_2O).

There can be various types of fusion reactions. Among them the fusion of hydrogen isotope is of most interest. Examples of fusion reactions of hydrogen isotopes are as follows

$$\begin{aligned} D_1^2 + D_1^2 &\longrightarrow He_2^3 + n_0^1 + 3.27MeV \\ D_1^2 + D_1^2 &\longrightarrow T_1^3 + H_1^1 + 4.03MeV \\ D_1^2 + T_1^3 &\longrightarrow He_2^4 + n_0^1 + 17.6MeV\,. \end{aligned} \tag{1.1}$$

The deuterium hydrogen isotope, D_1^2, consists of one proton and one neutron and the tritium, T_1^3, consists of one proton and two neutrons. For the sake of convenience, the first two reactions in Eq. 1.1 are referred to as the **DD** reaction, and the last reaction referred to as the **DT** reaction. In a fusion reaction, the fuels exist in an ionized gas state, called a *plasma*. One may note the advantage of the DT reaction for its huge amount of energy release over other isotopes reactions. The fusion power from a DT reaction is expressed as

$$P_{fusion} = n_D n_T < \sigma v >_{DT} E_\alpha\,, \tag{1.2}$$

where $n_{D,T}$ is the density of fusion plasma, $< \sigma v >_{DT}$ is the reaction rate of DT fusion which is a function of temperature, and E_α is the energy of alpha particle (or He_2^4) from the reaction, $\sim 3.5\,MeV$[1]. One of the critical conditions to achieve a reasonable fusion reaction rate is high temperature ($\sim 10\,keV$) at which the reaction rate $< \sigma v >_{DT}$ peaks. An example of a calculation of the fusion reaction rates for different reactions is plotted in Fig. 1-1. In this plot, the average reaction rate, $< \sigma v >$, is calculated as a function of relative kinetic energy of colliding isotope. The DT reaction has the high value of the reaction rate at a lower temperature, which makes the DT reaction favored in fusion research. Unless the plasma is confined with a proper method, the highly energetic fusion plasma moves freely in a container and

[1] $1eV$ energy is equivalent to a particle energy with the temperature of $11,600^oK$.

results in a severe impact on the container material. The electromagnetic properties of plasmas, however, provide the solution for the confinement, i.e. the concept of magnetic confinement fusion.

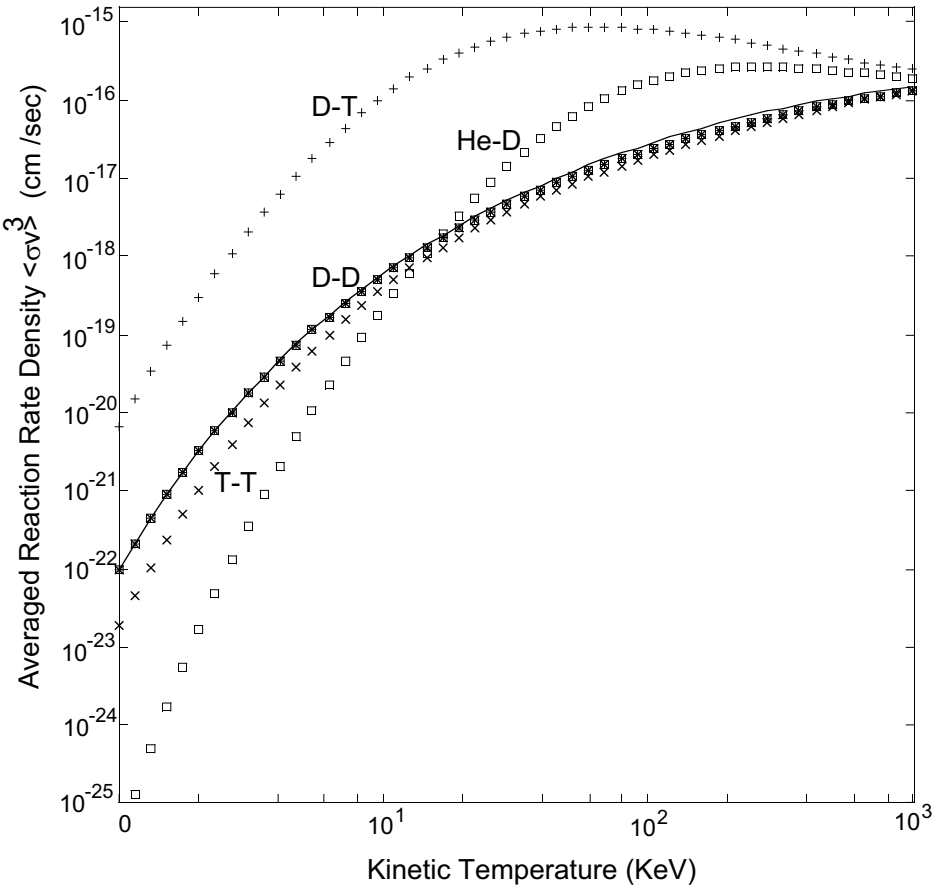

Figure 1-1: The reaction rates of various fusion reactions as a function of the relative energy (keV) of reaction ions. The DT fusion reaction has the highest value of reaction rate among other isotopes.

In plasmas, the charged particles are subject to the magnetic field, i.e. plasmas will be tied to the externally applied magnetic field. Fig.1-2 shows how the plasmas (composed of electrons and ions) are trapped on the magnetic field lines. Their motions are governed by the Lorentz force ($\vec{F} = \vec{v} \times \vec{B}$) resulting in the gyro-motion along the magnetic field lines. In the early stages of fusion research, a cylindrical-type fusion machine (with straight field structure) was devised. The straight field

line structure, however, had plasma losses at both ends. One solution to this end loss problem was to bend the magnet field lines into a closed donut-shape. The donut-shape fusion machine was named a *tokamak*[2]

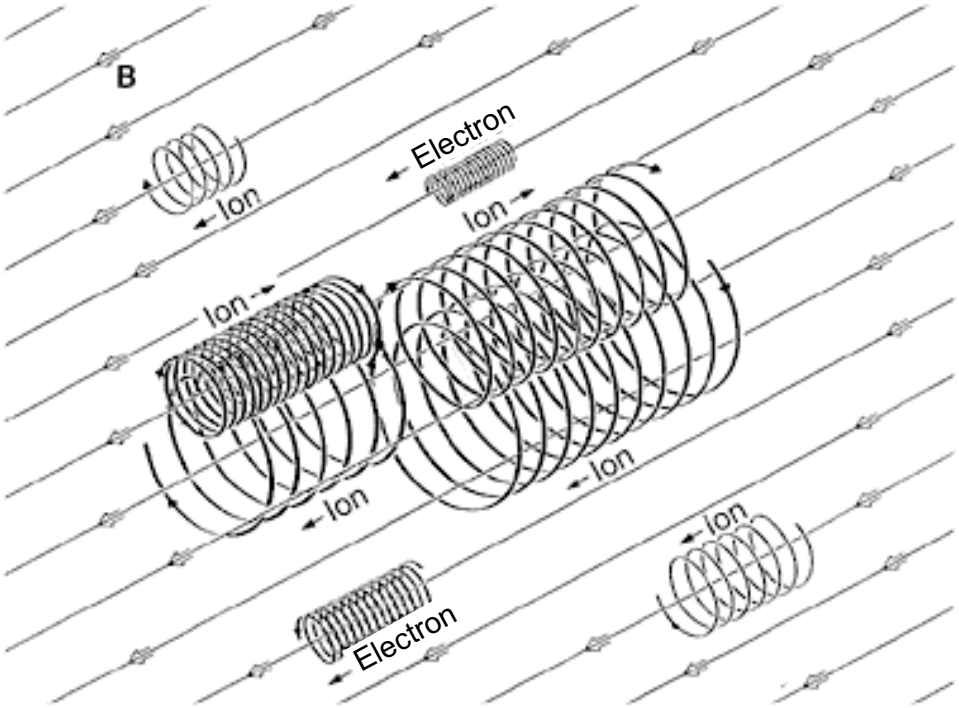

Figure 1-2: The plasma consists of electrons and ions in electrically neutral state. Each charged species tied to the magnetic field line makes a gyration motion along it (figure courtesy of IPP Garching [1]).

[2]acronym from the Russian words *TOroid KAmera MAgnit Katushka which means the toroidal chamber and magnetic coil*

1.2 Tokamak

The tokamak has been a successful and promising machine among other magnetic confinement fusion devices. It is characterized by donut-shape (a cylinder bent around to close both ends) high-vacuum chamber containing a large amount of toroidal plasma current ($\sim$ million amperes) initially induced by the central solenoid (ohmic transformer) in high temperature state ($\sim 10^8$ degree Kelvin). A schematic picture of a tokamak is shown in Fig.1-3.

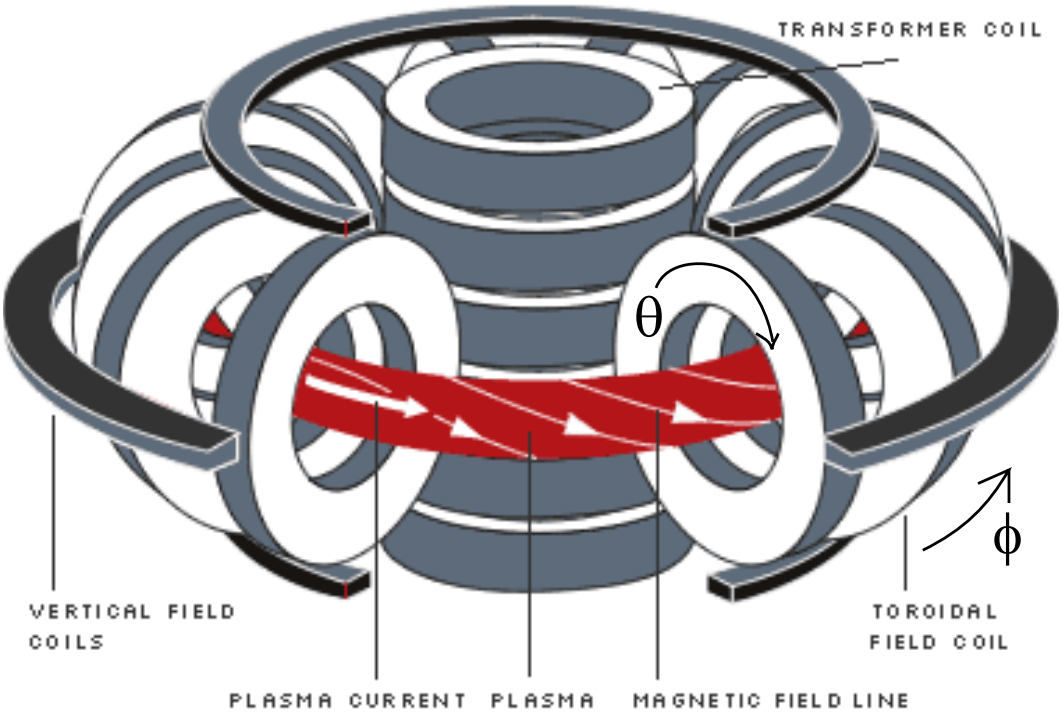

Figure 1-3: The conceptual view of tokamak with plasma column inside the chamber. The central solenoid is used to ionize the gas into a plasma and then induces the plasma current. The toroidal and poloidal magnet coils provide the control of stable plasma confinement (figure courtesy of IPP Garching [1]).

The toroidal field coils provide the primary magnetic field (in ϕ direction) for the

plasma confinement. The vertical field coils are also needed to control the plasma position with poloidal (θ direction) magnetic field. In addition, the plasma current in the toroidal direction produces poloidal magnetic field, which provides the plasma equilibrium. The combination of toroidal and poloidal field structure results in helical field lines inside the chamber. The performance of a tokamak can be expressed by the power balance as follows

$$\begin{aligned}
\frac{dW}{dt} &= P_{fusion} + P_{aux} - P_{loss} \\
&= P_{fusion} + P_{aux} - P_{tran} - P_{rad} \\
&= P_{fusion} + P_{aux} - \frac{3}{2}(n_e T_e + n_D T_D + n_T T_T)/\tau_E - n_z n_e L_z(T_e) \qquad (1.3) \\
Q &= \frac{P_{fusion}}{P_{aux}}, \qquad (1.4)
\end{aligned}$$

where P_{fusion} is the same as Eq. 1.2, P_{aux} is the auxiliary input power or the heating power required to compensate for the energy losses due to P_{tran} and P_{rad}. P_{tran} is the energy loss due to the particle transport (mainly by the radial diffusion) and P_{rad} is the energy loss due to the impurity radiation. The ultimate goal of tokamak reactor is to operate in steady state ($\frac{dW}{dt} = 0$) and in self-sustaining condition. By self-sustaining condition we mean the condition in which $P_{aux} = 0$, which is called as *Ignition Condition*. For the ignition condition (for 50:50 D-T mixture plasmas), the fusion reaction is sustained by the α particle (He^4) heating as

$$\begin{aligned}
n_D n_T < \sigma v >_{DT} E_\alpha &> \frac{3}{2}(n_e T_e + n_D T_D + n_T T_T)/\tau_E \\
\frac{1}{4} n_e^2 < \sigma v >_{DT} E_\alpha &> \frac{3 n_e T}{\tau_E} \\
n_e \tau_E &> \frac{12 T}{< \sigma v >_{DT} E_\alpha}, \qquad (1.5)
\end{aligned}$$

where $T_D = T_T = T_e = T$ is assumed. The right hand side of Eq. 1.5 is a function of temperature which has a minimum at $T \sim 30\, keV$. In addition, τ_E in the LHS of equation is also dependent on the temperature. Then the optimum T for the ignition is around $10 \sim 20\, keV$. With an approximate expression for $< \sigma v >_{DT}$ in this

temperature range, $< \sigma v >_{DT} = 1.1 \times 10^{-24} T^2\, m^3/sec$, one can obtain a convenient expression for ignition condition as

$$n\tau_E T > 3 \times 10^{21} \;\; (m^3\, sec\, keV)\,, \tag{1.6}$$

where $E_\alpha = 3.5\, MeV$ is used and T is in keV. This expression is similar to one identified by Lawson in early days of fusion research. He had recognized $n\tau_E$ as the critical parameter for the ignition and expressed the ignition condition. For detailed analysis of the fusion ignition see Ref.[2].

The progress and current status of controlled fusion research is indicated in Fig. 1-4.

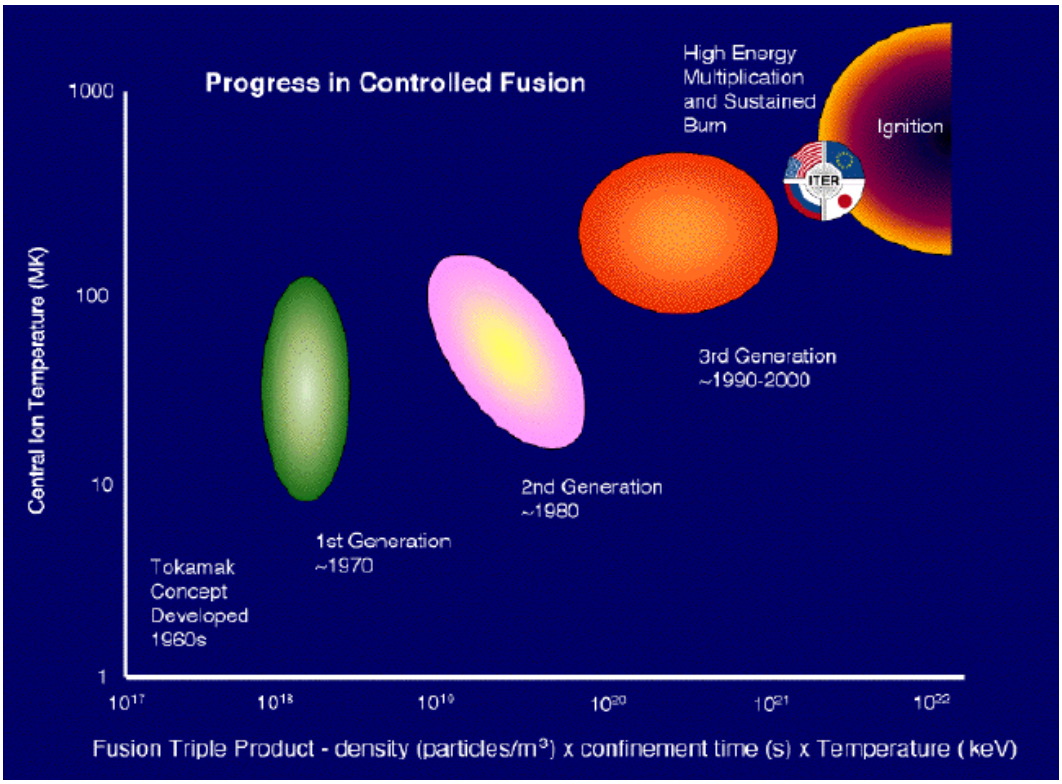

Figure 1-4: The progress and current status of fusion research in the world (figure courtesy of ITER website, http://www.iter.org

1.3 Impurities in Tokamak Plasmas

As far as the efficient power production is concerned, any impurities (non-plasma species) in a tokamak are unfavorable. Impurities are generated from the interactions between the plasma and the tokamak structure materials. Energetic plasma particles may escape from the confined region (core plasma) via diffusion and drift radially outward finally striking the tokamak surfaces such as chamber walls, antennas, etc. The lattice atoms of those target materials gain sufficient energy to break the binding forces and leave the surfaces. This mechanism is known as the *sputtering process*. In addition to the particle-surface interactions, high heat loads on the structure materials can cause the evaporative erosion at the heated surfaces and thus produce impurities. The detailed explanations of impurity generations are given in Ref. [3]. Major concerns about impurities are their negative effects on energy confinement: contamination of core plasma by impurities enhances the power loss by radiation and degrades the fusion reaction rate. The power loss by impurity radiation is expressed by $P_{rad} = n_e n_z L_z(T_e)$ which includes different types of radiations such as dielectronic/radiative recombination radiation, Bremsstrahlung radiation, and collisional recombination radiation. In this expression, n_e is the electron density, n_z is the impurity ion density in the core plasma, and $L_z(T_e)$ is the impurity emission coefficient which is a function of electron temperature. The calculation of L_z for different species can be found in Ref. [4]. The degree of the plasma tolerance to impurity radiation in a tokamak depends on the impurity species. For example, ITER [5] is envisaged to allow the following concentrations of impurities in the core plasma: $\sim 1\%$ $(n_z/n_e(\%))$ of low-Z elements (C, O), or $\sim 0.1\%$ of mid-Z elements (Ar, Fe), or $\sim 0.01\%$ of high-Z elements (W, Mo). It is, therefore, necessary to control the impurity transport and sources in order to reduce the plasma contamination and to reduce the effects of impurities on tokamak operations.

The surface treatments on the internal structures are the preliminary measures for the reduction of impurity generation; low-Z (B, C) material coating, baking the walls, and discharge cleaning are the typical methods. The applications of surface treatments in

different machines are reviewed in Ch.7 of Ref.[6]. In addition to the surface treatments, the plasma edge (the region close to the walls) can be used to minimize the loss of plasma via radial transport (and the resultant impurity generation at surfaces) and to remove helium ash from the confined plasma by controlling magnetic geometry. The *limiter* and *divertor* structures are used to change the magnetic geometry in a tokamak and will be reviewed in the next section.

1.4 Tokamak Divertor

It is required to keep plasma-wall interactions within acceptable limits. This can be achieved either by localizing the plasma-wall interaction on a *limiter plate* or by diverting the plasma from the edge region onto a remote surface (*divertor plate*) [7]. The use of limiter/divertor establishes a region where the plasma ions are swept rapidly toward the limiter/divertor. This narrow transport region is called *scrape-off layer* or *SOL*. Such structures are, however, also the sources of impurity generation due to interactions with colliding plasmas. In general, the limiter is placed near the confined plasma region, while the divertor is far from it. Therefore, the impurities generated on the limiter surface penetrate more easily into the plasma than those generated on the divertor surface.

Fig.1-5 shows an example of limited (left panel) and diverted operations in C-Mod [8]. The thick solid line defines the LCFS (last closed flux surface) or the separatrix. The region inside the LCFS is called core plasma, where the magnetic field lines close on themselves. On the other hand, in the region outside the LCFS which is called the SOL, the field lines end on the walls or the targets (called *open field region*).

The separatrix and SOL region are produced by a combination of plasma current and divertor coil currents. The coil in the divertor structure carries current with the same direction as the plasma current. Accordingly, the magnetic field lines produced by the divertor coil currents annihilate the magnetic field lines generated by the plasma currents. The location at which the both magnetic fields annihilate each other is called *null-point* or *X-point*. The equilibrium magnetic flux surface on which the x-

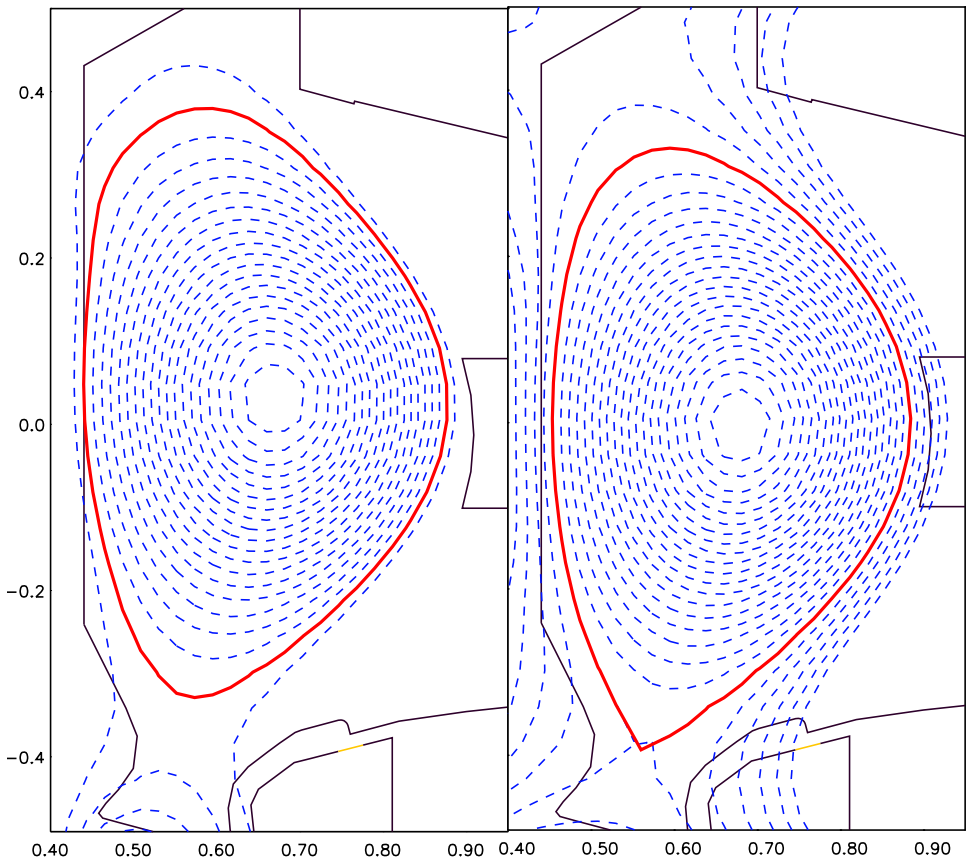

Figure 1-5: The examples of equilibrium magnetic flux surfaces in poloidal plane generated by limited(left) and diverted(right) operations in C-Mod. The thick closed line defines the LCFS. The region outside the LCFS is the SOL. The divertor surfaces are marked by thick lines.

point is located is called the separatrix. The flux surface which is located just inside the separatrix is called *last closed flux surface* (LCFS). The SOL, typically a few *cm* thick, plays a role of an insulating layer between the confined plasma (should be clean and pure) and the impurity sources at walls/limiters. For example, in C-Mod, a substantial amount of main chamber fueling (or main chamber recycling) of order of $\sim 10^{22}\, s^{-1}$ is estimated [9]. The subsequent active interactions between the recycling plasmas and surface (wall, antenna limiter) materials generate the impurities. The impurities that originate from the walls or limiters will penetrate into the SOL and further into the core to contaminate the fusion plasma. However if there are strong flows in the SOL, a significant portion of the impurity ions is expected to be drained away from the core down into the divertor targets. It is also observed that there can

exist very strong outward, cross-field, radial transport in tokamaks [10, 11, 12, 13, 14]. Such strong radial transport in the SOL reduces the impurity penetration into the core plasma.

One of challenges which the diverted tokamak operation faces is handling of huge amount of particle and heat fluxes on the target which may cause severe damage on the surface material. The large amount of heat flux parallel to the magnetic field ($\sim 1\,GWm^{-2}$) is predicted for future fusion reactors with divertor operation [15]. The C-Mod divertor typically has parallel heat flux incident on the target surface of $q_{||}^{SOL} \sim 0.5\,GWm^{-2}$. As one of the solutions, divertor operation where the parallel heat flux is dissipated before reaching the divertor plates is suggested. This scenario achieves a cold (few eV) and dense ($\geq 10^{21}\,m^{-3}$) plasma region in front of the target[16]. This cold and dense region can radiates significant amount of power in the divertor region. Impurity ions are typically used for this purpose. If well constrained near the divertor region, the impurities reduce the heat flux onto the targets via radiation without causing radiation in the core plasma. For further study of divertor, we refer you to a recent review of divertor experiments in Ref. [17].

1.5 Goals and Outline of This Thesis

Experiments studying impurity screening from, and penetration into, the core plasma, along with the confinement of impurities in the C-Mod divertor have motivated this study. The goal of this thesis is to explore the underlying physics to these results which have not been clearly understood. The general review of the experiments is presented in Ch.2. As a tool of modeling study, the DIVIMP Monte-Carlo code is employed. Details of the DIVIMP code are described in Ch.3. The changes to the DIVIMP code to allow for measurement of impurity ion fluxes and modifications of physics descriptions to better handle impurity recycling are introduced in Ch.4. The modifications are regarded as necessary to explain the physics of recycling impurity retention. Descriptions of background plasmas specified for modeling input are given in Ch.5. The modeling of impurity screening is briefly described in Ch.6. Details of

the underlying physics of the impurity screening and penetration is presented in Ch. 7, which covers a number of issues:

- influx study: What are the characteristics of impurity influx through the separatrix ?
- recycling study: What is the relative importance of the different recycling sources for determining impurity concentrations in the core plasma ? Those recycling locations are the antenna limiter, inboard wall, outboard wall, or targets.
- screening study: What physics processes or quantities control the screening of impurities ?
- flow study: How is the impurity ion parallel flow determined by background plasma forces (thermal and frictional) ? How sensitive is the screening of impurities to those flows ?

The conclusion and summary will be given in Ch.8.

Chapter 2

Experimental Results on C-Mod Impurity Retention

Experimental studies of impurity penetration, screening [18, 19] and compression [20] in C-Mod will be reviewed in this chapter. All of the experiments discussed in this chapter are for Ohmic L-mode discharges with no RF input power applied. Impurity neutrals are injected by NINJA from the vacuum region into the SOL. The poloidal location of the gas injection was varied for the purpose of the study. The details of the impurity injection method is described in Ref. [21].

2.1 Impurity Penetration and Screening Experiments

The main parameter to be measured in the experiments is the impurity density in the core plasma. The radiation in the core plasma from high Z impurity ions are measured by the HIREX (High Resolution Xray spectroscopy) [22] instrument. For the low Z impurity measurement in core, a VUV spectrometer is used [21]. The emission intensities from the above spectrometers are used as input to the MIST 1D impurity transport code [23] to determine the impurity content in the core. Two different types of impurities were measured. One is the recycling impurity such as argon, neon and

helium. Another is the non-recycling impurity such as nitrogen, carbon and metals (W, Mo). Recycling impurities reaching the walls or targets may be backscattered and re-enter the SOL. Non-recycling impurities, in contrast, are expected to have very low backscattering probability. The number of recycling impurities in core was found to be proportional to the total number of injected atoms while the number of non-recycling impurities in core was proportional to the injection rate. Differences between recycling and non-recycling impurities were also found in the dependency of impurity screening on the poloidal position of the injection: inner midplane, outer midplane, bottom of the divertor (in PFZ). Screening of recycling impurities did not show dependence on the varying injection location. The number of recycling impurities in the core for inner wall injection, outer midplane injection and divertor injection cases were of comparable levels. The core population of non-recycling impurities varied as the injection location varied. The screening for the injection at the inner wall was better (fewer of the injected impurities reached the core) than the outer wall injection case. It was observed, however, that the screenings of both recycling and non-recycling impurities were enhanced as the plasma density increased.

The effect of different magnetic configuration on the impurity screening was also studied. The impurity screenings were compared between a limiter plasma (Fig.1.5 (a)) and a divertor plasma(Fig.1.5 (b)) for both the recycling and non-recycling impurities by measuring the penetration factors. The penetration factor for recycling impurity was defined as [19]

$$PF_R = \frac{\text{total number of impurity ions in core}}{\text{total number of impurity atoms injected}} \tag{2.1}$$

which is non-dimensional parameter. On the other hand, the penetration factor for non-recycling impurity was estimated in different way as

$$PF_{NR} = \frac{\text{total number of impurity ions in core}}{\text{rate at which impurity atoms were injected}} \tag{2.2}$$

which has units of time.

The limiter plasma case obtained PF values dependent on the gas puff location for

both recycling and non-recycling impurities: the inboard gas puff case had a PF much higher than the outboard/divertor launch cases. Note that these plasmas were limited on the inner limiter so that an impurity injected from the surface was immediately inside the LCFS. In addition limiter plasmas had poorer screening performance than divertor plasmas by a factor of ≥ 10. The high penetration of impurity injected in limiter inboard plasma is attributable to more ionization occurrences deeper into the core than the outboard launch, i.e. the limiter inboard launch has all impurity ionizations inside the LCFS whereas the outboard launch leads to many, if most, ionizations outside the LCFS.

In summary, the screening for a recycling impurity in diverted plasma has no dependency on the poloidal launch position. Non recycling impurities in diverted plasmas have penetration factors varying with the different launch position: inboard launch has better screening than other launch positions. The comparison between the limiter and diverted plasma has shown that the limiter case has the poor screening than the divertor one. Both the recycling and non-recycling impurities have a penetration factor dependent on the launch position in the limiter plasma cases. The penetration factor decreases as the plasma density increases. A review of screening dependency on the background plasma density is presented in the next section.

2.2 Impurity Compression Measurement

One of the principal functions of the divertor is to minimize the number of impurities reaching the core plasma and degrading fusion reactions. In addition to reduction of the impurity core level, it is also important to retain both the impurity neutrals and ions in the divertor region to better pump out the neutrals (typically helium ash) and to dissipate the high heat flux transmitted unto the divertor plate by utilizing impurity ion radiation. The impurity level in the divertor region which the above experiments lacked has been estimated in the compression measurement campaign in C-Mod. The compression for Ohmic L-mode with single-null diverted discharges will be reviewed in this section. As well as the compression's dependence on plasma

density, the effect of gas leakage from the divertor plenum controlled by the unique bypass structure [24, 25] was measured in this campaign.

2.2.1 Definition of Impurity Compression Ratio

The impurity compression ratio is one of the measurements of the divertor performance of impurity retention in the divertor region. In C-Mod the (neutral) impurity compression ratio, c_z, is defined as

$$c_z = \frac{n_{div}^{zo}}{n_{core}^{z+}} \tag{2.3}$$

where n_{div}^{zo} and n_{core}^{z+} are the impurity neutral density in the divertor plenum and the impurity ion density in the core plasma, respectively. The impurity neutral density is obtained from the neutral gas partial pressure measurement with an RGA [26], where the impurity neutral is assumed to be in equilibrium at room temperature, $\sim 0.03eV$. Fig. 2-1 shows both the cross section in poloidal plane and the top view of C-Mod with bypass structure.

2.2.2 Compression Measurements

C-Mod has conducted a series of experiments to measure the argon impurity compression for Ohmic L-Mode shots during run #990429. The variation of compression ratio as the plasma density changes is plotted in Fig.2-2.

For closed bypass, the argon neutral density in divertor (n_{div}^{o}) at moderate density ($\bar{n_e} = 1.4 \sim 1.9 \times 10^{20} m^{-3}$) is higher by a factor of ~ 2 than that at low and high (detached) density discharges. The argon ion density in core (n_{core}^{z}) behaves in the opposite way, although the density (n_{core}^{z}) change from moderate to high density (detached) discharge is less significant. The resultant compression ratio, c_z, increases as density increases before the detachment and then rolls over as the detachment occurs. The open bypass, in general, drops the argon neutral density in the plenum by a factor of ~ 1.6 and raises the argon ion density in the core by a factor of ~ 1.2. The compression ratio for open bypass case, therefore, reduces by a factor of ~ 2

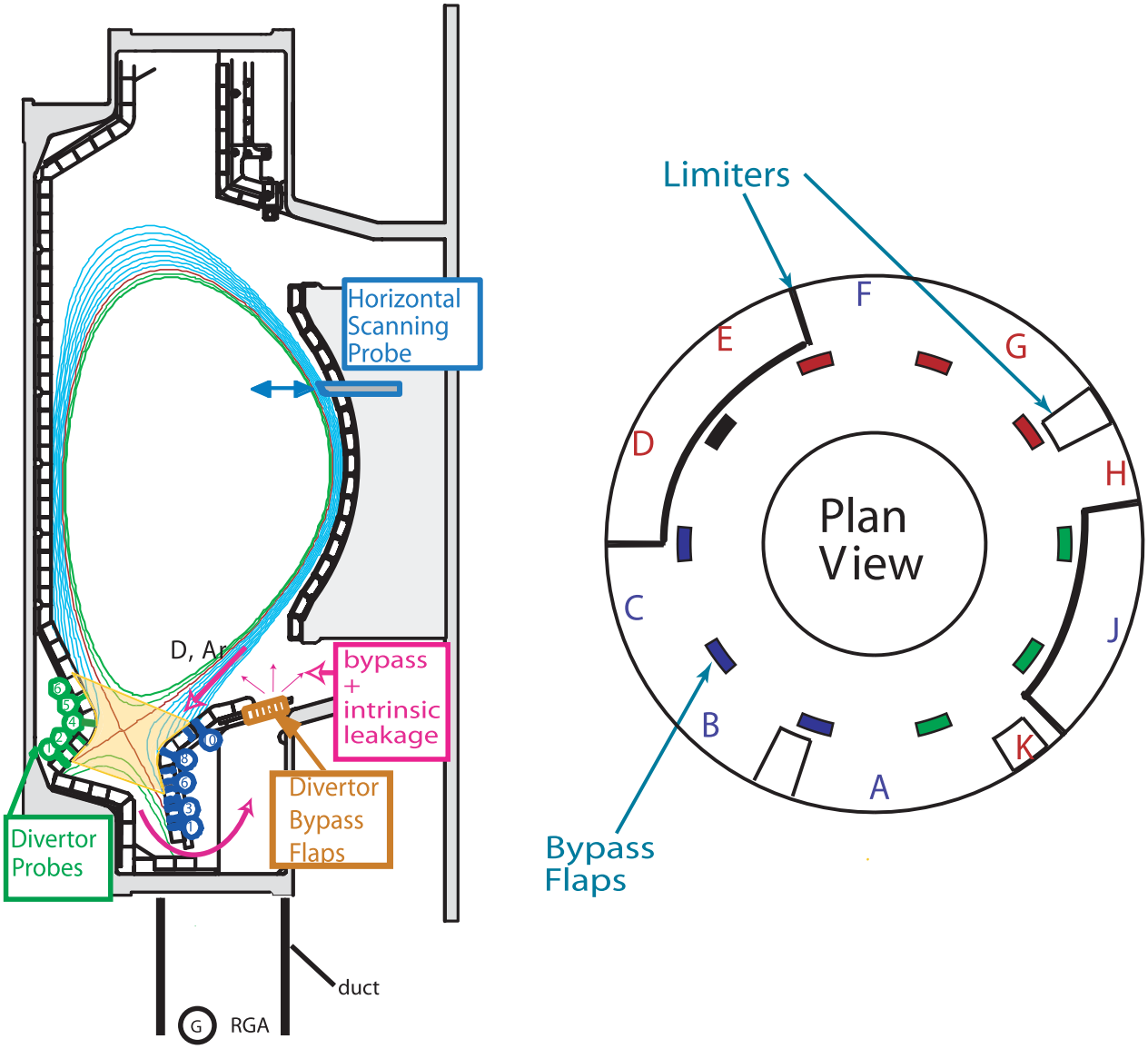

Figure 2-1: The cross section in poloidal plane (left) and the top view (right) of C-Mod. The 10 bypass flaps are located uniformly in the toroidal direction. There are 10 ports (named with alphabet letters) around the torus to provide the diagnostic access. Some of the ports (D,E,G,H,K) are called *open ports* due to a toroidal gap between divertor sectors to allow diagnostic access.

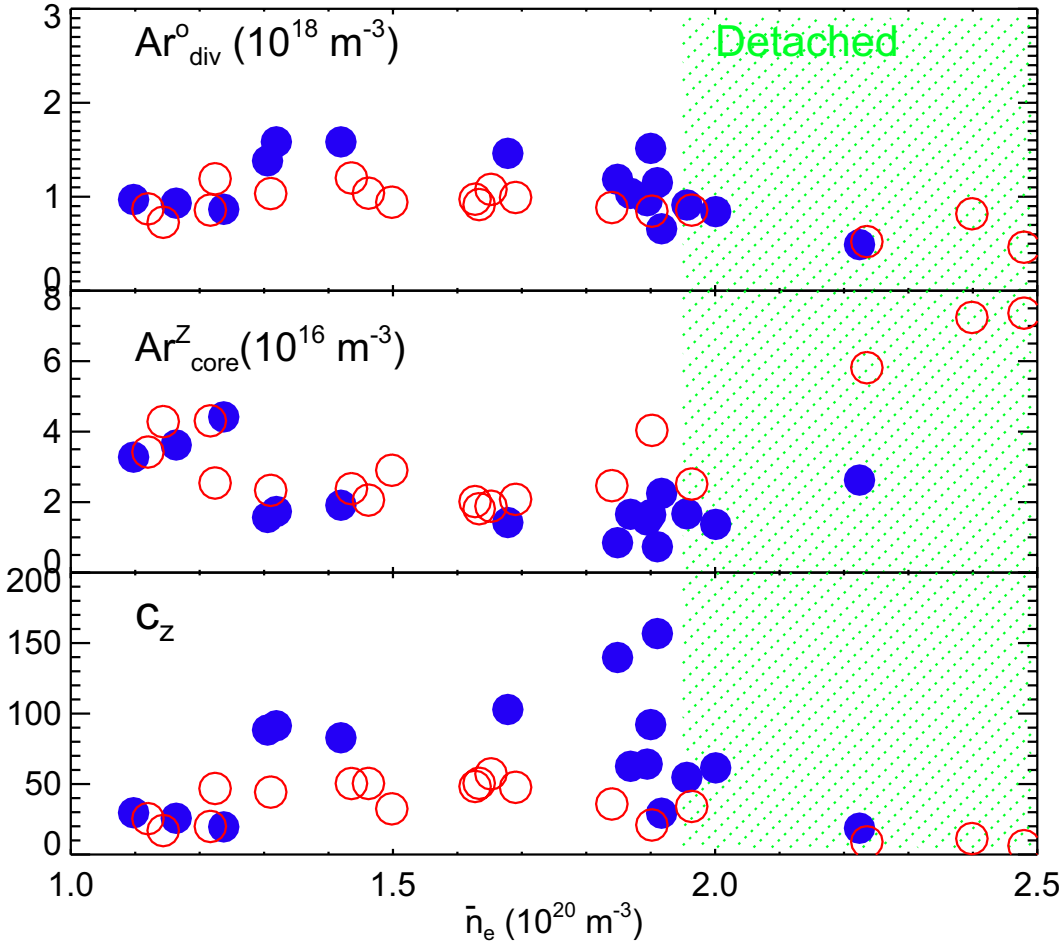

Figure 2-2: Experimental measurements of argon compression ratio for different discharges with line averaged core density ranging $1.2 \sim 2.4 \times 10^{20} m^{-3}$. The top panel shows the Ar neutral density in divertor, the middle panel shows the Ar ion density in the core, and the bottom panel shows the Ar compression ratio. Closed symbols correspond to closed bypass cases and open symbols to open bypass cases.

mainly due to the neutral pressure drop in the plenum.

In summary, the compression ratio increases as the density increases, which is similar to the results observed in the impurity screening experiments. The compression ratio drops as the plasma detaches. The effect of gas leakage on the compression was also measured using the bypass. The open bypass reduces the impurity neutral density in the plenum by a factor of ~ 1.6 while it increases slightly the impurity ion density in the core. This implies that the leaking neutrals may not directly penetrate through the SOL into the core. The study of neutral sources in C-Mod [27] suggested that the neutrals leaking through the bypass reach the main chamber region just outside the divertor and then are ionized. Thus, instead of traveling directly to the midplane, leakage neutrals are redirected most likely by ionization and/or collisions. The detailed study of divertor neutral baffling using the bypass and its effect on impurity compression is presented in Refs. [28] and [29], respectively.

Chapter 3

Impurity Transport in DIVIMP Monte Carlo Code

The DIVIMP (*DIV*ertor *IMP*urity) Monte Carlo code [30] has been employed for modeling of impurity retention in C-Mod. The code was developed at the University of Toronto to model impurity production and transport in axisymmetric divertor geometry in two-dimensions. The code consists of two main routines [31] for neutral (neut.d6a) and ion (div.d6a) transport which follow an individual impurity particle in time as it moves within a specified background plasma. The 2D spatial distribution of background plasma parameters such as $n_e, T_e, T_i, v_{||}$, and $E_{||}$ are given as input to the code. Typically the background plasmas are obtained by a fluid code such as UEDGE[32], B2[33], or EDGE2D[34] which can be coupled with DIVIMP. In this study a simplified method based on OSM (Onion Skin Method, Ch.12 in [35]) is used to calculate the plasma parameters as simply as possible.

Brief descriptions of the code (principles, computational grid), impurity neutral and impurity ion transport will be presented in this chapter. The details of background plasma descriptions including the OSM are given in Ch. 5.

3.1 Introduction to DIVIMP

DIVIMP initially launches a certain number of impurity neutrals from the vacuum region into the computational grid and calculates the trajectories of impurities. This is a typical way of modeling gas injection experiments such as ones reviewed in Ch.2. The computational grid shown in Fig. 3-1 is generated by the SONNET [37] grid generator with information of equilibrium magnetic flux given as input. The code EFIT [36] is used to calculate equilibrium magnetic flux.

There are three distinctive regions in the computational grid: core, SOL and PFZ regions. The core region consists of 7 rings (or flux tubes). Each core ring has 36 cells in poloidal direction. The SOL region consists of 12 radial rings and each ring has 54 poloidal cells. The PFZ region consists of 7 rings $\times$ 18 poloidal cells. Each ring is distinguished by radial index IR and each poloidal cell (on a ring) is distinguished by poloidal index IK. In the SOL and PFZ regions, IK starts from the inner target and ends on the outer target. In the core region, IK starts from a cell which contacts x-point and ends advancing clock-wise at a cell which also contacts x-point. The inner most core ring (IR=1 is a virtual ring for boundary condition) has a reflecting boundary condition: impurity ions reaching this ring are reflected off to the position occupied at previous time step. Different types of boundary conditions for the outer most SOL (IR=19) and PFZ (IR=20) rings can be applied: absorbing wall condition, reflecting wall condition or recycling wall condition. With absorbing condition the ions reaching the edge ring (IR=19 or 20) will be discarded. With reflecting wall condition all the ions reaching the edge rings will be reflected back into the incident cell. Recycling wall allows the ions to be recycled as neutrals (the FP option is employed in this case and the FP option is explained in Ch.4).

Impurity neutrals are injected (from the vacuum region) or recycled on the targets/walls and travel until they are ionized inside grids where the background plasmas are specified. Ionized impurities or impurity ions are subject to the forces generated by background plasmas and travel until they reach the targets, walls or limiters. Some of the ions may move out of the grid into vacuum region where no plasmas are

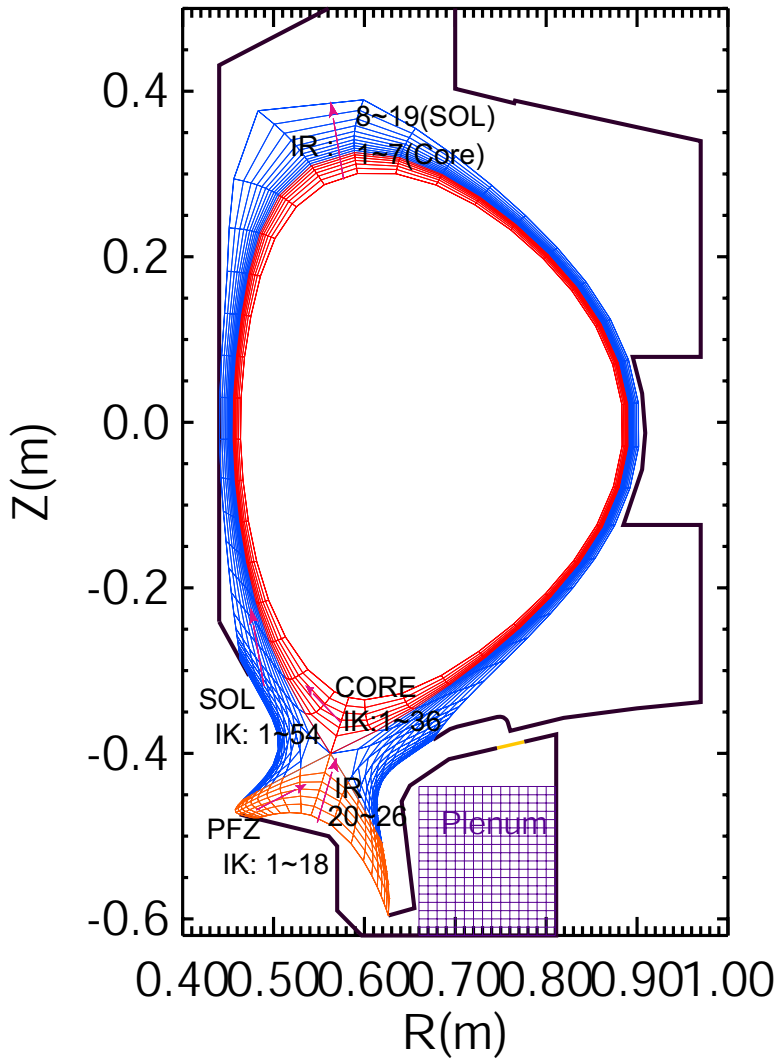

Figure 3-1: Computational grid for the DIVIMP modeling. The grid is generated by SONNET grid generator with the information of equilibrium magnetic flux calculated by EFIT code. The core region has 7 rings (distinguished by radial index IR ranging from 1 to 7) on which the background plasmas are specified. Each ring has 36 cells in poloidal direction (each poloidal cell is distinguished by poloidal index IK). The SOL region has 12 rings (IR = 8-19) $\times$ 54 poloidal cells. The PFZ region has 7 rings (IR = 20-26) $\times$ 18 poloidal cells. The inner most core ring (IR=1) is a virtual ring for a reflecting boundary condition. The outermost SOL/PFZ rings (IR = 19 and 30) are virtual rings for edge boundary conditions.

described (with a recycling wall condition turned on). Those ions are handled by the *FP* option which calculates the ions positions in that region in an approximate way. As the code follows an impurity neutral or ion in a computational grid cell the code counts the number of time steps recorded in the cell and then converts those step counts into impurity ion number density. Typically the impurity ion number density in the core region and the impurity neutral number density in the plenum are used for the estimation of impurity compression ratio.

3.2 Neutral Transport

In the simplest treatment the impurity neutrals are assumed to move in a straight line until they are ionized or reflected at the walls or the targets. The code follows the neutrals in time with a time step δt_o specified to be smaller than the ionization time,

$$\tau_{iz} = (n_e < \sigma v >_{iz})^{-1} \tag{3.1}$$

where 'iz' denotes the neutral ionization. The typical time step size is given as :

$$\delta t_o \sim 10^{-8} < \tau_{iz} \sim 10^{-7}(sec) \tag{3.2}$$

For the calculation of atomic processes such as ionization and recombination, the relevant rate coefficients are taken from ADAS [38]. As the code follows the neutral, it checks if any of the following events have occurred; reflection at the walls or targets, ionization in plasma, momentum-transfer collisions (MTC). The MTC event deflects the neutral's trajectory by 90^o. Detailed descriptions for atomic processes such as ionization, recombination and MTC are presented in Appendix A.

When an impurity neutral strikes a wall or a target element, it is reflected off the surface. For a reflection check, the code tries to find an intersection point between a wall line segment and a trajectory line made by the neutral. For example in Fig. 3-2, the (R,Z) coordinates of a neutral made between computational time steps $t = t_o$

and $t = t_o + \delta t$ produce a trajectory line. Then the code checks if this line has an intersection with a line segment of nearest wall. The neutral which has an intersection is then reflected at the intersection point on the wall into a cosine angular distribution with an emission energy of $0.03\,eV$ assumed.

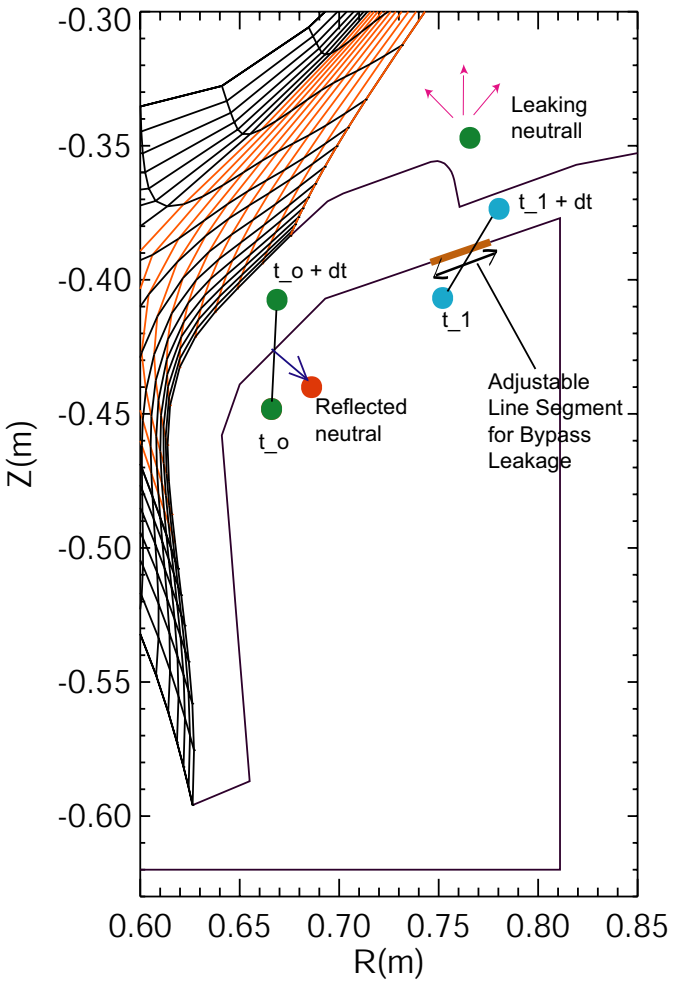

Figure 3-2: The cartoon of the neutral reflections and bypass leakage inside the plenum. A neutral of which trajectory is made between t_o and $t_o + \delta t$ has an intersection with a wall line segment is reflected on the intersection point into a cosine angular distribution with launch energy of $0.03\,eV$. When a neutral trajectory has an intersection with the line segment designated for bypass exit , the neutral is launched from the main chamber just above the bypass exit.

In the plenum region neutrals will experience many reflections at the plenum wall surfaces. When a neutral trajectory made by particle coordinates between time steps $t = t_1$ and $t = t_1 + \delta t$ has an intersection with a certain line segment designated

for the leakage exit, then the neutral position is relocated to a location outside the plenum ((R,Z) = (0.76, -0.35) as in Fig. 3-2.) and launched with cosine angular distribution into a main chamber region. Fig. 3-2 describes the neutral reflection and leakage from the plenum. The length of the segment for leakage is adjustable. For an intrinsic leakage (with closed bypass) model, the length of exit line segment is specified as $16\,mm$ which gives the equivalent gas leakage area ($\sim 0.08\,m^2$) estimated in C-Mod [24]. For an additional leakage (with open bypass) which produces another $0.08\,m^2$ of leakage area the length of line segment will be doubled ($32\,mm$). Current modeling assumes that the gas leakage occurs in toroidal symmetric way. In the real machine, however, the gas leakage occurs non-axisymmetrically. Comparison of the modeling of axisymmetric gas leakage and the non-axisymmetric gas leakage in the experiment is illustrated in Appendix C.

3.3 Ion Transport

When neutrals are ionized, an ion transport routine is called to follow impurity ions until they reach the walls, targets or limiters. The ion transport consists of perpendicular and parallel components. This section describes briefly how the step size of impurity ion is determined both in the perpendicular and parallel direction. For detailed descriptions including the subroutines associated with impurity ion transport, please refer to Appendix B.

The perpendicular transport shifts the impurity ions radially by a step size $\delta s_\perp$ estimated by

$$\delta s_\perp(m) = \pm\sqrt{D_\perp \delta t} + (v_{convection} + v_{pinch})\delta t \tag{3.3}$$

where $D_\perp$ is the radial diffusion coefficient, $v_{convection}$ and v_{pinch} are the impurity ion radial convective and pinch velocities respectively. In the current model only diffusion is included to determine the radial step ($v_{convection} = 0$ and $v_{pinch} = 0$).

For the radial diffusion coefficient, a constant value of $0.1\,m^2/sec$ is assumed in this model. The changes in parallel position, $s_{||}(m)$, and velocity, $v_{||}(m/sec)$ during the computational time step δt ($= 0.1\mu sec$ in this model) are determined by the following governing equations[1]

$$s_{new} = s_{old} + v_z^{old}\delta t + \frac{1}{2}\delta t^2\frac{F}{m_z} = s_{old} + v_z^{old}\delta t + \frac{1}{2}\delta v_z\delta t \tag{3.4}$$

$$v_z^{new} = v_z^{old} + \delta v_z \tag{3.5}$$

$$\delta v_z = \frac{v_p - v_z^{old}}{\tau_s}\delta t + \sqrt{\frac{T_z}{m_z}}\sqrt{\frac{2\delta t}{\tau_{||}}}r_G + \left(ZeE + \alpha_e\frac{dT_e}{ds} + \beta_i\frac{dT_i}{ds}\right)\frac{\delta t}{m_z} \tag{3.6}$$

$$\alpha_e = 0.71Z^2 \tag{3.7}$$

$$\beta_i = \frac{3(\mu + 5\sqrt{2}Z^2(1.1\mu^{5/2}0.35\mu^{3/2}) - 1)}{2.6 - 2\mu + 5.4\mu^2} \tag{3.8}$$

$$\mu = \frac{m_z}{m_z + m_i} \tag{3.9}$$

$$\tau_s = \frac{1.47\times 10^{13} m_z T_i\sqrt{(T_i/m_i)}}{(1 + m_i/m_z)n_i Z^2 ln\Lambda} \tag{3.10}$$

$$\tau_{||} = \frac{1.47\times 10^{13} m_z T_z\sqrt{(T_i/m_i)}}{n_i Z^2 ln\Lambda} \tag{3.11}$$

where r_G (Eq. 3.6) is a random number from a Gaussian distribution, τ_s (Eq. 3.10) and $\tau_{||}$ (Eq. 3.11) are Spitzer's stopping and parallel diffusion coefficients [39], T_i, T_e, and T_z are plasma ion, electron and impurity ion temperatures (in eV units) respectively, n_i (in $\tau_{||}$ and τ_s) is the background plasma density (m^{-3}), m_z is the impurity ion mass, m_i is the plasma ion mass (both masses are in amu units), v_p (m/s, Eq. 3.6) is the parallel flow of background plasma and Z is the atomic number of impurity ion. The typical value of $ln\lambda$ (in the equations (3.10) and (3.11)) is 30. The electric field E in the parallel direction is calculated by Ohm's law with an assumption of ambipolarity ($j = -n_e(v_e - v_i) = 0$) as

$$E = -\frac{0.71}{e}\frac{dT_e}{ds} - \frac{1}{en}\frac{dp_e}{ds}, \tag{3.12}$$

[1]P.C.Stangeby, Sec. 6.5.3, *The Plasma Boundary Of Magnetic Fusion Devices*

where p_e is the electron pressure (nT_e).

The first term in RHS of Eq.(3.6) corresponds to the frictional force due the background plasma flow, the second term corresponds to diffusion in velocity space (i.e., changes in v_z due to collisions between impurity ions and background plasmas), and the last two terms correspond to thermal forces due to the plasma temperature gradients. After the updates of s and v are finished, the ion transport routine checks if the ions have struck the targets or have moved out of the grid edge to reach the walls in the vacuum region. When the ions are found to reach walls and targets the neutral transport routine is called to launch the recycling neutrals (*recycling* event).

3.4 Recyclings of Impurity Ions

Most of the DIVIMP runs used in this thesis model an impurity gas puff by launching a certain number of initial neutrals, N_o, from the outside midplane. The neutral transport routine neut, follows neutrals until they are ionized. The ion transport routine div, follows the ionized impurities until they strike the targets or diffuse out to the walls in vacuum region. Then, div routine stops following the ions. At this point, the one cycle of neut-div routine circulation is completed and one recycling event is recorded. The maximum number of recycling events, before the code is stopped N_{recycl}, is specified as input. Every recycling neutral has a recycling coefficient *sputy*, assigned to it as a weight factor. With N_{recycl} of recyclings and $sputy = 1$ specified as input, total of $N_o \times N_{recycl} \times sputy^{N_{recycl}}$ ions/neutrals are followed. This is the typical way of modeling 100% recycling impurities, such as He, Ne and Ar. For the non-recycling model, *sputy* is specified as less than 1.0. After m recyclings, the non-recycling particle has the weight factor of $sputy^m << 1.0$. When this number, $sputy^m$ drops to a certain limit, then this particle is discarded and a particle loss is recorded. In this case the total number of ions followed is less than $N_o \times N_{recycl}$. Another simple way of modeling non-recycling impurities is to *kill* the ions when they strike the targets or the walls.

For proper modeling of a recycling impurity, wise selections for N_o and N_{recycl} are

required. Usually a large ratio of N_{recycl}/N_o(with N_o small) is preferred. N_o should be smaller than N_{recycl} to have the initial launch condition negligible but should be large enough for good statistics. Usually N_o of $40 \sim 50$ is used. Then the optimum value of recycling numbers should be found. Let's consider a case which has the maximum recycling number of 10,000 (the 40 initial particle launch and 10,000 recyclings case takes approximately 20 hours on a Pentium III machine). The time history of variation in impurity ion density will be used for the selection of optimal value. Fig. 3-3 shows variation of poloidal distribution of impurity ion density in a ring as the recycling number changes. The results show that the case run reaches close to an equilibrium state after the recycling number exceeds 1,900. Thus the value of 2,000 for seems to be reasonable value for the minimum recycling number to reach an equilibrium state. The run with 40 initial launches and 2,000 recyclings takes about 6 hours in the same machine.

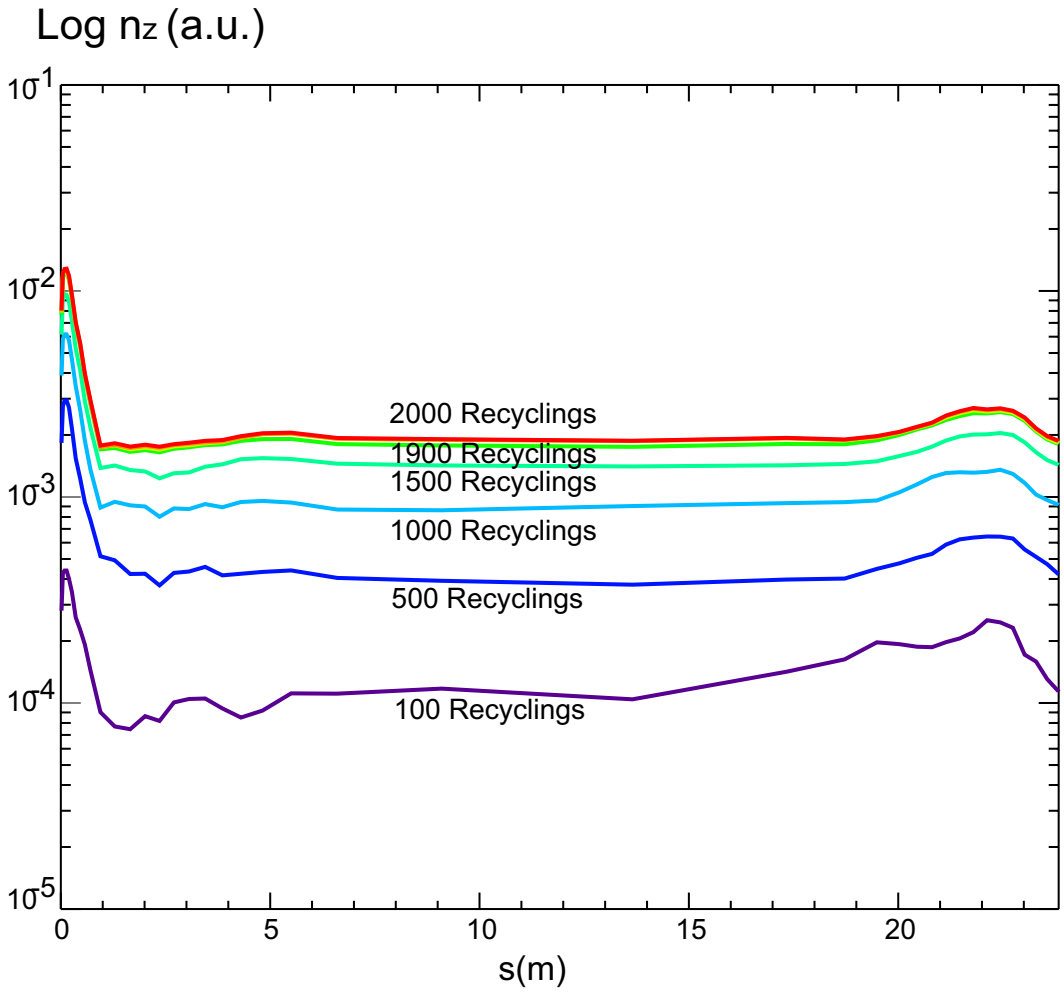

Figure 3-3: Variation of poloidal distribution of impurity ion density in a SOL ring at different recycling stage. As recycling number increases the density profile reaches an equilibrium state.

Chapter 4

New Diagnostics and Descriptions in DIVIMP

Impurity retention study should provide answers to physics questions, such as *how do impurity ions reach the core plasma? where do they come from? what's the role of impurity recyclings?* The answer to the question of first type requires a description of the impurity ion flow pattern. For the other question a method of identifying the connection between the recycling source with its core penetration is needed. Implementation of new diagnostics and modifications of existing diagnostics were needed for the purposes of providing the impurity ion flow model, the tracking of recycling neutral sources, and a better description for target recycling and main chamber recycling. We have modified the version of DIVIMP received to implement these capabilities.

4.1 New Methods for Flux Density Measurements

The flux densities (nv and $-D\nabla n$ will be called *conventional flux densities* through this thesis) obtained from the continuity or momentum equations in a fluid code are based on time-averaged quantities. In DIVIMP, however, the flux densities are based on statistical quantities as the code uses the number of steps made in a cell for the number density calculation. We evaluated several possibilities to expand flux density measurements to all parts on the grids. It turned out that the conventional expres-

sions for flux densities (nv or $-D\nabla n$) did not give an accurate enough representation of the impurity ion flow pattern. We have found that a less 'noisy' description of impurity ion flow is to count ions crossing the boundary at all cells. The principle is simple: first, count the number of events when a particle crosses the cell boundary either in the parallel or the perpendicular directions and then convert this count into an arrow vector (this vector will be used for plotting impurity ion flow). The method of counting the cell boundary crossings will be called *facecrossing*. The parallel component of *facecrossing* will be called *parafxing* (parallel face crossing) and *perpfxing* (perpendicular face crossing) will be used for the radial component. In some cases it is interesting to see the radial facecrossings through the separatrix only. For this purpose the *sepxing* is used. The *perpfxing* counts every radial facecrossings on cell boundaries. The *sepxing*, however, counts an ion's initial crossing the separatrix (into the core) and final crossing the separatrix (out of the core into the SOL) before the ion is recycled. In this section we will compare flux density measurements made by the conventional methods and the alternative methods.

4.1.1 Radial Flux Density Measurement

The comparison of flux density measurements on the separatrix by $-D\nabla n$ and *sepxing* will be presented here. For the study, the medium density plasma is used. Plasma density and temperature values are $8 \times 10^{19} m^{-3}$ and $52eV$ at the separatrix and decrease radially outward in the SOL. The sign convention used for facecrossing is that as a particle of charge state iz crosses the separatrix into the core, it results in a $sepxing_{iz} = -1$. There were various studies for the comparison between the two methods. One example case of various comparison studies is presented here. Argon ions (Ar^{+1}) used as test particles are launched at the edge of SOL (inside the grid). For the purpose of study, all the parallel forces are turned off, i.e., only the radial diffusion acts on the ions to move them across the cells. An absorbing wall is used as the boundary condition: when the ions reach the outermost cell in the edge of SOL they will be discarded (sink at wall). The resultant flux density, therefore, is expected to have direction toward the absorbing wall outside the source location. No net flux

density inside of the source location is expected.

Absorbing wall model

Fig. 4-1 shows the radial distribution of argon ion densities at the outer midplane where they (50,000 ions) are launched.

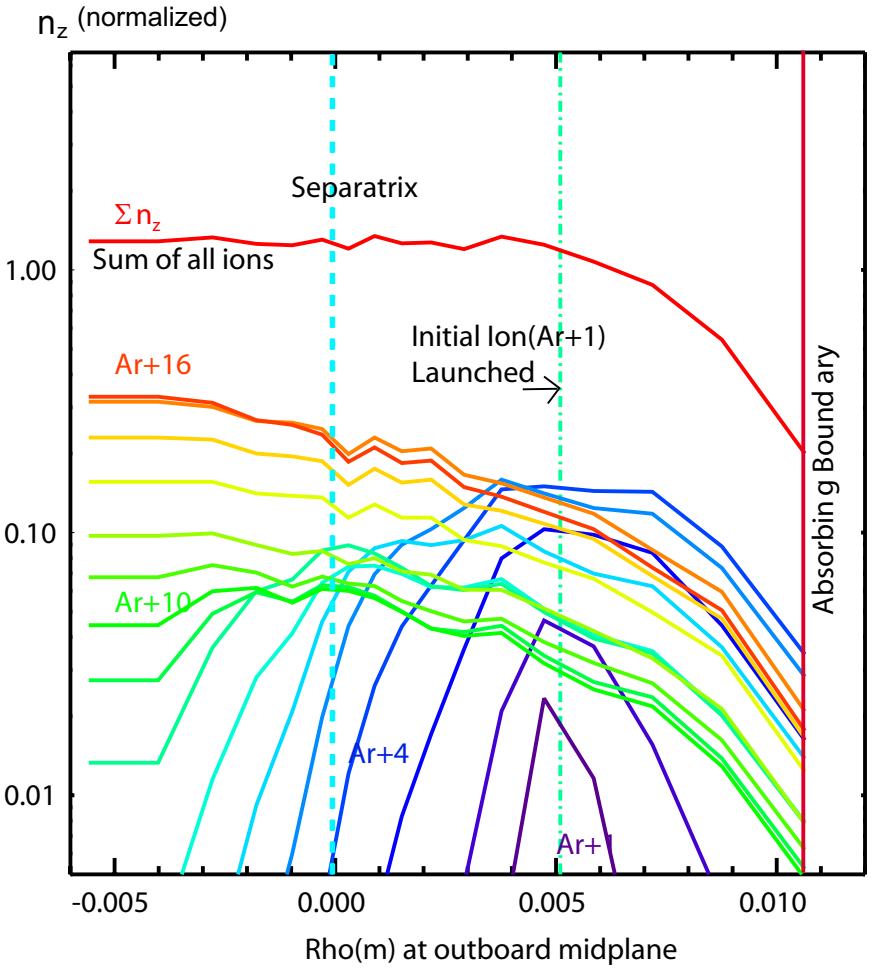

Figure 4-1: The radial distribution of Ar ions for absorbing wall model.

The lower-Z ions are distributed near the edge of SOL and the higher-Z ions are peaked inside the SOL and the core region. The plot indicates that the ions with $Z \leq 8$ enter the core ($-D\nabla n_z < 0$) and the high Z (≥ 9) ions cross out of the core ($-D\nabla n_z > 0$). The radial distribution of all ions was expected to be flat in the core and the SOL near the separatrix. However the radial profile is not flat but a bit bumpy which results in non-zero net flux across the separatrix based on the

"conventional" method. Near the edge of SOL the radial profile has a finite gradient (ion flux toward the edge wall due to the sink action). The details of flux density patterns on the separatrix are plotted in Fig. 4-2. In that figure, the flux densities estimated by $-D\nabla n_z$ and *sepxing* are compared. Both estimations indicate that the ions are entering the core plasma in lower charged states and coming out to the SOL in higher charged states. However only the *sepxing* measurements result in particle conservation, i.e. the net flux density on the separatrix is zero, while the $D\nabla n_z$ does not conserve particle balance. The conservation of particles, therefore, favors *sepxing* over $D\nabla n_z$.

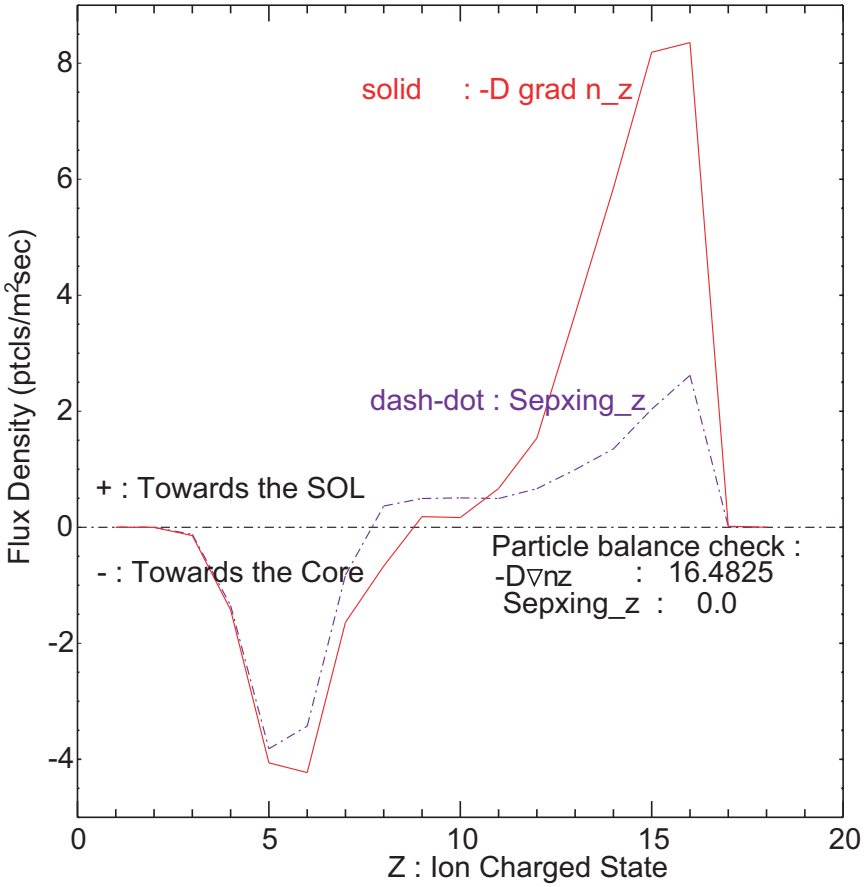

Figure 4-2: The comparison of flux densities estimated both by $-D\nabla n_z$ and *sepxing*. The solid line indicates the $-D\nabla n_z$ flux density per charged state and the dashed-dot indicates the one for *sepxing*.

There are several other comparison studies performed with different statistics, different boundary/initial conditions, and different plasma parameters. The statistics were

improved by either increasing number of test particles (250,000 test ions) or reducing computational time step (by a factor of 4) which increased particle dwellings in a cell. The enhanced statistics, however, didn't guarantee the particle conservation in $D\nabla n_z$ flux density measurements. The effect of different boundary/initial conditions were investigated. The boundary condition was changed by using the reflecting wall condition to allow all the ions reaching wall surfaces would be reflected back to the plasma. The initial condition was changed by launching ions at the edge of the SOL near the absorbing wall (sink) instead of launching ions in the middle of the SOL (the reference case). The conventional flux density measurements didn't result in particle conservations in any cases.

In summary, $D\nabla n_z$ measurement never provided the particle conservations while the facecrossing measurement always guaranteed the particle conservations.

4.1.2 Parallel Flux Density Measurement

Similar comparisons have been made for the parallel flux density. $parafxing_{iz}$, the parallel component of facecrossing, is compared with $(nv_{||})_{iz}$. The positive *parafxing* means that the particle has crossed in the direction to the outer target. One of the example cases is given here. The ions are launched in front of the inner target and move only by parallel diffusion, i.e. there are no other parallel forces to move the ions. The absorbing condition is applied on the inner target while the reflecting condition is applied on the outer target (the ions are discarded at the inner target and reflected at the outer target). It is therefore expected that the resultant net flux density is zero above the launch point and negative (ions flow toward the inner target) below this point. The resultant comparison is plotted in Fig. 4-3. Fluxes directed toward the outer target have positive values. Although the discrepancies for nv_z are not large, particle conservation is obtained only by the facecrossing method.

There were additional comparison studies performed on parallel flux density measurements. In all test cases set up with different conditions (launch locations, reflecting condition at both the targets, and parallel plasma forces turned-on), only the facecrossing method resulted in full particle conservation.

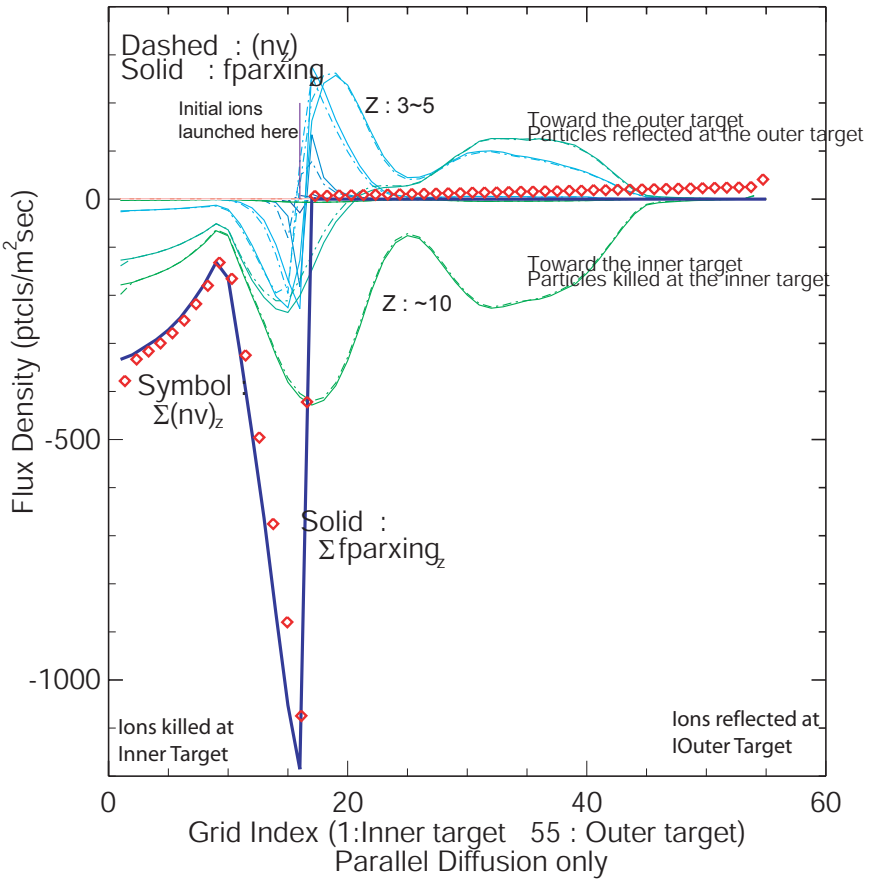

Figure 4-3: Comparison of two flux densities, nv and $parafxing$. The ions are launched above the inner target which has the absorbing wall condition. All the ions will be reflected at the outer target. In the region between the source location and the outer target it is expected that the net ion flux should be zero. The zero net flux density is obtained only by the face crossing method.

4.2 Recycling Descriptions

We discuss here two types of recyclings in DIVIMP. One is the target recyclings of impurity ions. Another is the far periphery (FP) recyclings of ions striking the main chamber surfaces. The recycling description has been modified in the course of this work. In the previous descriptions, an impurity ion recycling on the target is launched as a neutral with an energy of $0.03\,eV$ and an ion recycling in the FP region (or vacuum region) is launched as a neutral at one of the edge of targets. The modified target recycling allow relaunched neutrals to have a certain amount of emission energy greater than $0.03\,eV$. Revised FP recycling model launches the recycling ions as neutrals from various locations in the main chamber region.

4.2.1 FP(Far Periphery) Recyclings

The code calculates the impurity ion transport based on the forces produced by background plasma. In the case that impurity ions move out of the plasma grid, an approximation described by the *FP* option is applied to determine the transport there. There are 3 fates which an ion transport in the FP region may have: diffusing back to the plasma grid from which they left (called RES1), diffusing radially further out to the wall (RES3), or diffusing in parallel direction to the nearest surfaces in the main chamber (RES4). When an impurity ion's dwell time in the FP exceeds a computation time limit, it is discarded (RES2). The ions which have the fate of either of RES3 or RES4 will be re-launched at specified locations as recycling neutrals. All the recycling neutrals are launched into cosine angular distribution back toward the plasma with a fixed energy ($0.03\,eV$). The previous version of FP option had all ions crossing the edge of the grid launched as neutrals at the edge of inner or outer targets. It is known that impurities can be generated and recycle in the main chamber. With the previous FP option the effects of various recycling mechanisms on the impurity retention would be lost.

The details of the ion recycling process in the new FP option are summarized here. There are two geometry parameters specified for the modified FP option. One is the

virtual wall distance d_{fpw} which defines the limit of distance by which the RES3 ion can travel via radial diffusion in the FP region beyond the edge of the grid. Typically $2.5\,cm$ of distance (d_{fpw_o}) is specified in the outboard region and $0.5\,cm$ (d_{fpw_i}) for the inboard region. Another is the parallel loss spot on which the RES4 ions are recycled. There are four spots for RES4 recycling ions in the outboard SOL: upper SOL (PL1), antenna limiter spots (PL2 and PL3), and the edge of outer target (PL4) indicated in Fig. 4-4.

In the event of ion's entering the FP, the initial position $(x_{||}, x_{\perp})$ is assigned to the ion. The initial position in the parallel direction, $x_{||}(m)$ is the value of $s(m)$, the distance from the inner target to the cell from which the crossing into the FP has occurred. The initial position for the perpendicular transport is zero ($x_{\perp}(m) = 0$). At each computational time step δt, the radial position is updated as $x_{\perp} = x_{\perp} + \delta s_{\perp}$, where $\delta s_{\perp}(m) = \pm\sqrt{D_{FP}\delta t}$ and the parallel position is updated as $x_{||} = x_{||} + \delta s_{||}$. The parallel step size is determined by $\delta s_{||}(m) = \pm C_s \delta t$, where $C_s = \sqrt{\frac{2T}{m_H}}$. The sign $\pm$ depends on from which cell the ions escape. If the exit cell is closer to the top of machine (in Fig. 4-4) than to the antenna limiter, the $-$ve sign will be assigned, i.e. the ion is assumed to travel in direction to upper chamber. The fate of ion is determined based on the following conditions

- RES1 : $x_{\perp} < 0.0$ and $x_{||} < L_m$
- RES3 : $x_{\perp} \geq 2.5\,cm$ and $x_{||} < L_m$
- RES4 : $x_{\perp} < 2.5\,cm$ and $x_{||} \geq L_m$,

where L_m is the distance to the nearest wall from the inner target. RES1 ion diffuses back to the plasma grid. RES3 and RES4 ions recycle on the corresponding recycling spots. Typical value of T in C_s is $5\,eV$ which makes the parallel transport dominant over the radial transport in the outboard SOL FP. For the inboard SOL FP, however, the radial transport is dominant due to the close distance to the inner wall. For example, the ions diffusing out of the inboard cells will have RES3 fate while the ions diffusing out of the outboard cells will have RES4 FP fates. Fig. 4-4 shows the

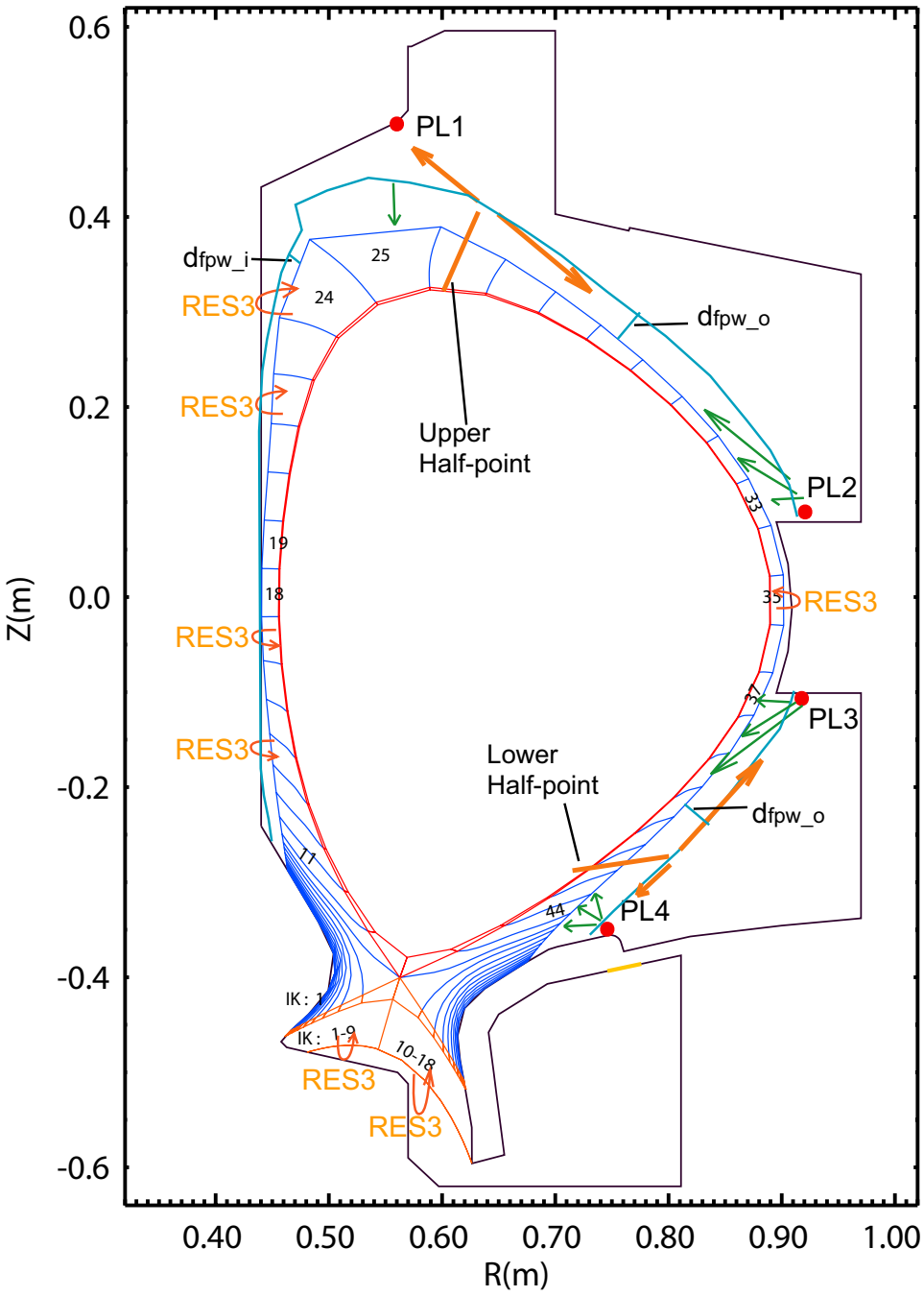

Figure 4-4: Illustration for the modified FP options. The ions in the inboard FP region promptly diffuse radially out to the wall (located at a distance, $d_{fpw\_i} = 0.5\,cm$, from the grid edge) before they diffuse in parallel. Thus the inboard region has RES3 recyclings only. FP regions in PFZ and in front of the antenna limiter have also RES3 recyclings only. On the other hand, the outboard FP regions ($PL1 \sim PL2$, $PL3 \sim PL4$) have only RES4 recyclings (with $d_{fpw\_o} = 2.5\,cm$): all the ions in this FP region diffuse parallel into PL1, PL2, PL3, or PL4 recycling locations. The direction of parallel diffusion is determined based on whether the ion is located on the left/right side to the upper/lower half point.

description of FP model, especially for the RES4 fate. The ions diffusing out from the left side of the upper half-point (the cell 25 and a part of the cell 26) will be recycled at PL1 and the ions diffusing out from the right side of the upper half-point (the cells $26 \sim 33$) will be recycled at PL2 (the upper part of antenna limiter). The similar rule is applied to the lower part of the outboard. RES3 recycling ions are launched as neutrals back to the cells where the ions left while RES4 recycling ions are launched as neutrals at one of PL's into cosine angular distribution.

We tested how the change of T in C_s affects the competition between RES3 and RES4 in the outboard region. Fig. 4-5 shows variation of dominance of each recycling (RES3 or RES4) in the outboard FP SOL. With $d_fpw = 2.5\,cm$ in the outboard region RES4 recycling (or the parallel diffusion) is dominant over RES3 recycling (or the radial diffusion) over $T \geq 0.05\,eV$ range.

In summary, FP ions are recycled via either parallel diffusion (RES4) or perpendicular diffusion (RES3). The outboard regions, (PL1-PL2) and (PL3-PL4), have only RES4 recyclings while rest of the regions (inboard FP SOL, PFZ, and antenna limiter) have RES3 recyclings.

4.2.2 Target Recyclings

The impurity ions striking the targets are launched at the target surfaces as recycling neutrals. Some of them will be recycled (launched) as thermalized neutrals (with $0.03\,eV$ energy) and some of them (determined by the particle reflection coefficient, R_N) will be reflected with a certain portion of incident energy (determined by the energy reflection coefficient, R_E) into a cosine angular distribution. R_N and R_E respectively, for $Ar - Mo$ model are taken from the TRIM model of $He - C$ due to the limitation of data availability. The reason for taking $He - C$ model is that it has the similar parameters dictating the reflection model, i.e., the incident angle ($\sim 60^o$) and the mass ratio, $\frac{M_{He}}{M_C} \sim 3$ (the mass ratio for $Ar - Mo$, $\frac{M_{Ar}}{M_{Mo}} \sim 2.6$). The reference model is Eckstein's model [40] in which R_N and R_E are fitted into the

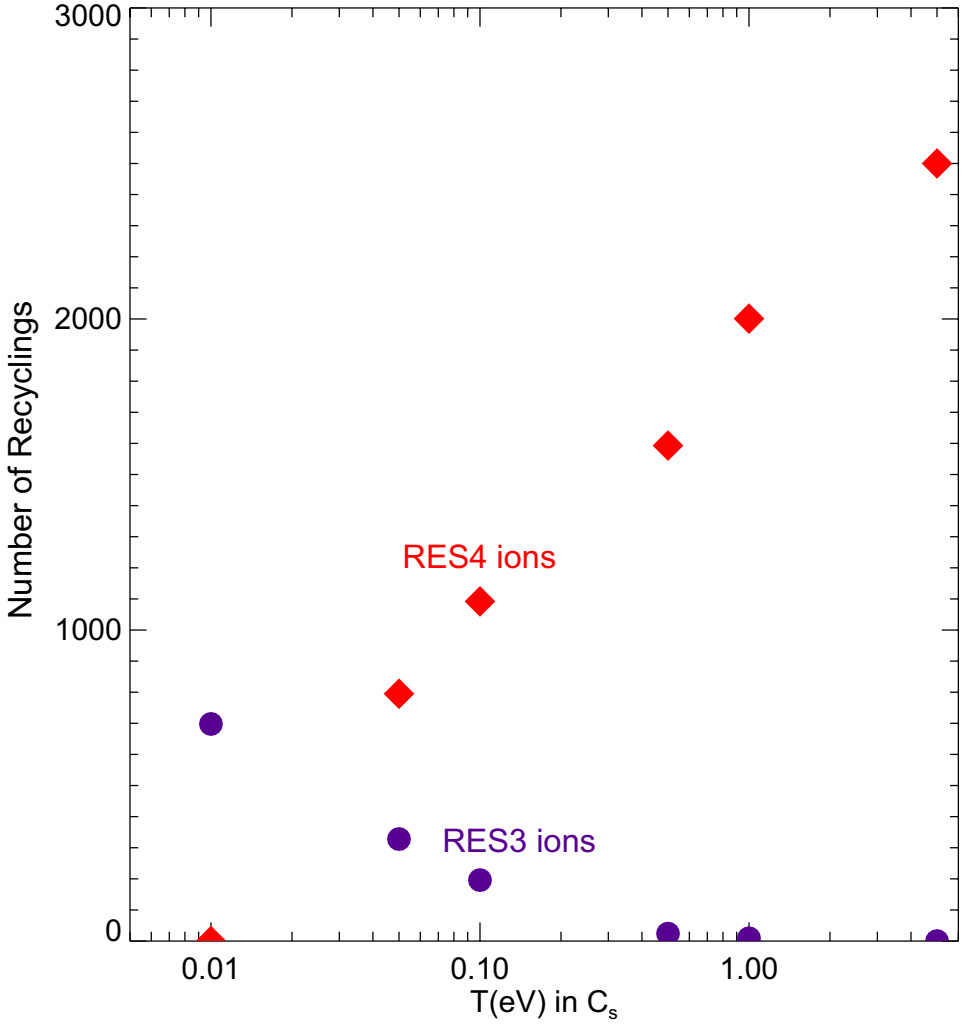

Figure 4-5: The sensitivity of RES3/RES4 ions to the temperature T in the parallel diffusion model, $C_s = \sqrt{2T/m_H}$. Two recyclings (RES3 and RES4) are estimated. RES3 recyclings (circle) are summation of all RES3 ions over the region ($PL1 \sim PL2$) and the region ($PL3 \sim PL4$). RES4 recyclings (diamond) are summation of all RES4 ions recycled at locations PL1, PL2, PL3, and PL4. RES3 recyclings (ions reaching the wall via radial diffusion) are dominant with $T \leq 0.01\,eV$. RES4 recyclings (ions reaching the limiters or walls via parallel diffusion) are dominant with $T \geq 0.05\,eV$. Current model ($T = 5\,eV$) has no RES3 recyclings in the outboard FP (except for RES3 recyclings on the antenna limiter).

following expressions

$$R_N = \left[(1+3.2116\,\epsilon^0.34334)^{3/2}+(1.388\,\epsilon^{3/2})^{3/2}\right]^{-2/3} \quad (4.1)$$

$$R_E = \left[(1+7.1172\,\epsilon^0.3520)^{3/2}+(5.2757\,\epsilon^{3/2})^{3/2}\right]^{-2/3} \ , \quad (4.2)$$

where ϵ is the reduced energy defined as

$$\epsilon = 32.55\frac{M_2}{M_1+M_2}\frac{1}{Z_1Z_2(Z_1^{2/3}+Z_2^{2/3})}E_o \ , \quad (4.3)$$

a function of the nuclear charge (Z) and mass (M) of the incident (subscript 1) and target (subscript 2) atoms and the incident particle energy E_o. In this model, E_o, the energy of incident impurity ion is expressed as

$$E_o = \frac{1}{2}m_z v_z^2 + 3kZT_e \ , \quad (4.4)$$

where Z is the charge state of impurity ion, the subscript z represents the impurity ion. The maxium value of the kinetic energy that an incident impurity ion may gain is when v_z becomes the deuterium ion sound speed (background plasma flow), $v_z = \sqrt{2T_e/m_D}$. Thus the maximum gain of kinetic energy is $\frac{m_z}{m_D}kT_e$, which is $\sim 20kT_e$ for Ar impurity ion. The result of calculations are plotted in Fig. 4-6.

When an impurity ion hits the target, a random number ξ is drawn which is uniform in the range [0,1]. If ξ is greater than the particle reflection coefficient, R_N, then this ion is recycled as thermalized neutral ($0.03\,eV$). If ξ is less than R_N, then the neutral is emitted with a energy estimated as $E_{emit} = E_{impct}\frac{R_E}{R_N}$ into a cosine angular distribution. For example, if the 10,000 test ions are reflected from the target, it is expected that $10,000R_N$ reflected particles have the energy above ($0.03\,eV$).

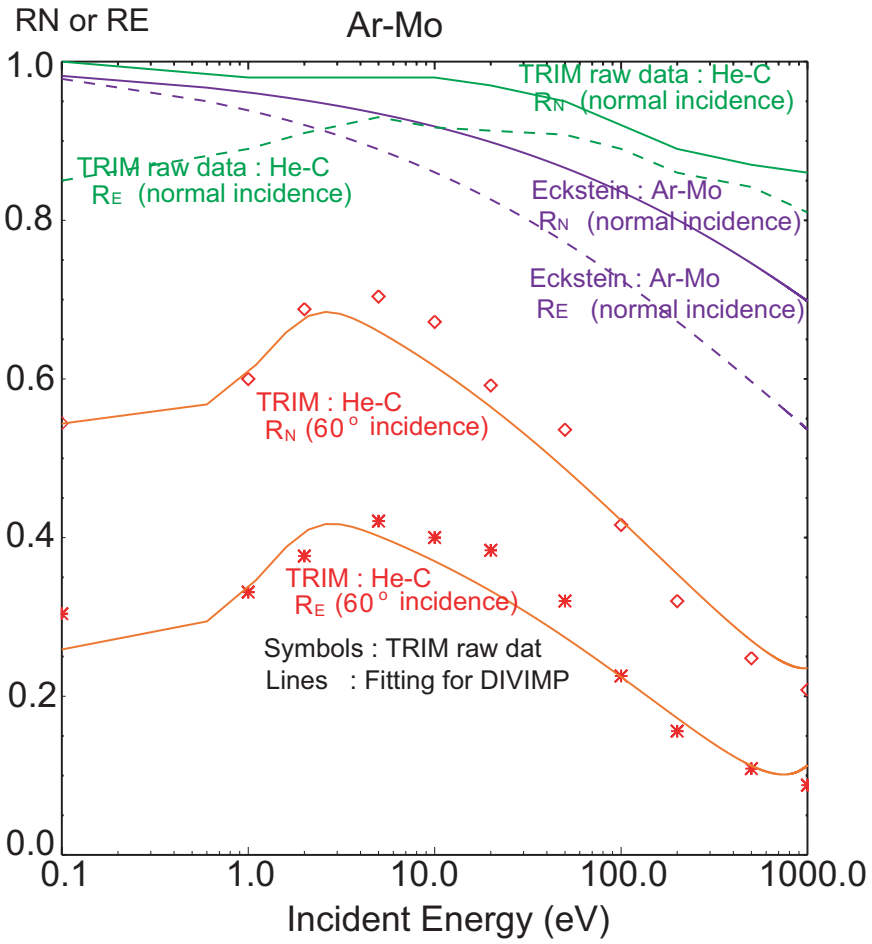

Figure 4-6: The calculations of particle and energy recycling coefficients for Ar-Mo. The reference data is obtained both from Eckstein model (for normal incidence of Ar on Mo) and TRIM model (for He-C with oblique incident angle). Calculations of TRIM and Eckstein models for the normal incidence case is given for the estimation of how precisely the current TRIM model approximates Ar-Mo intereaction.

4.3 Identification of Connection Between the Recycling and the Core Penetration

It is important to know which recycling sources contribute to the core impurity levels and where they cross the separatrix. To identify such a connection between the recycling sources and the core penetration diagnostic *counters* are placed both on the recycling locations and on the separatrix. Fig. 4-7 shows the DIVIMP grid for recycling diagnostics. The index marked on the cell around the poloidal plane (1-88) distinguishes the different cells at the edge of the grid. The counter on each cell is to count the number of particles reaching it. For RES3 recycling particles, there are as many counters as the cells around the SOL (index:18-71 in Fig. 4-7).

RES4 recycling particles are counted at one of the four locations : PL1,PL2,PL3 and PL4. In the same way, each divertor target element has an individual counter to count the target recycling particles. The neutrals launched from recycling spots are tagged with that information (i.e. the target element index). Another type of counter is placed on the separatix to check the origination of ions crossing the separatrix. With combined data obtained from both the separatrix and source location it can be recognized which recycling source has contributed to core penetration at which separatrix location. Thus this diagnostic gives information of how many recyclings have occurred on various recycling locations (*recycling source strength*) and how many of those recycling neutrals reach the core plasma (*source contribution to the core impurity levels*). The ratio of the *source contribution to the core impurity levels* to the *recycling source strength* is used for an estimation of penetration factor. The number of ions crossing the separatrix is counted by facecrossing arrays. There are two kinds of radial facecrossings: one is perpfxing and another is sepxing. The difference (explained in 4.1) can be understood easily with an example case of single particle launch with a single recycling shown in Fig. 4-8.

first particle a A single particle is launched from PL3 spot and becomes ionized at poloidal cell 55 in the SOL. The ion makes its initial entrance to the core on the separatrix cell 55 and makes the final exit to the SOL cell 60 before recycling on the

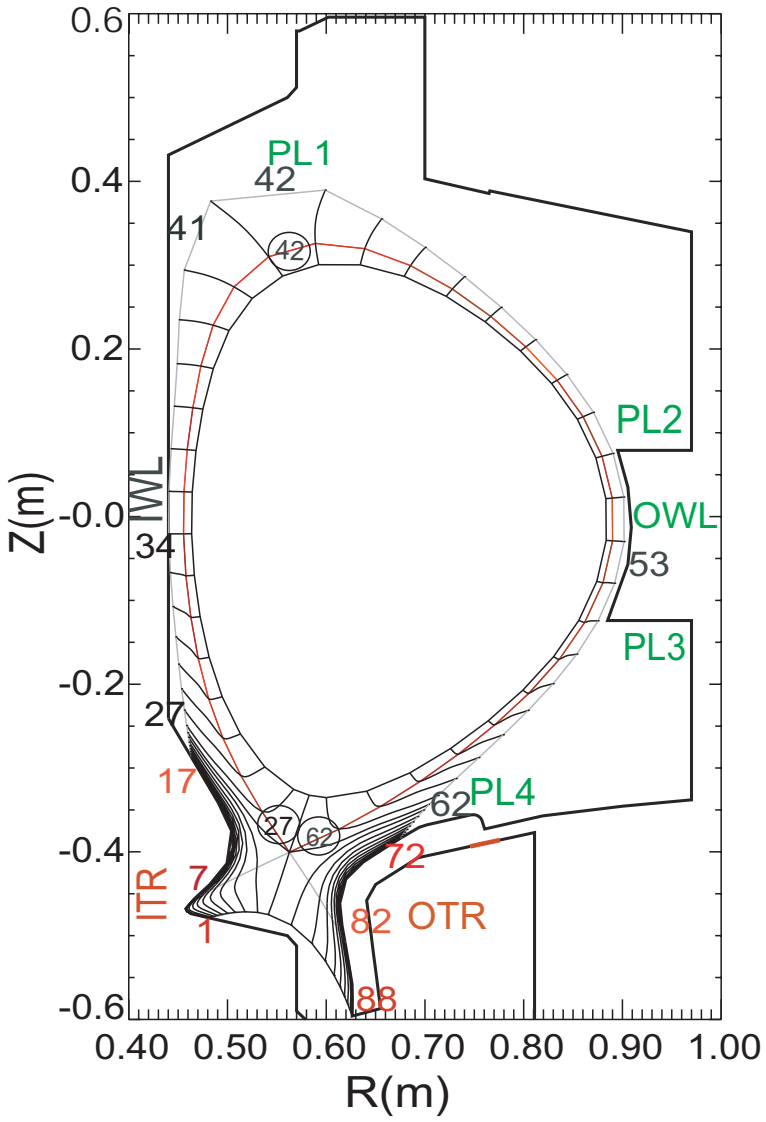

Figure 4-7: The DIVIMP computational grid with the recycling locations indicated. The circled number indicates the grid index on the separatrix.

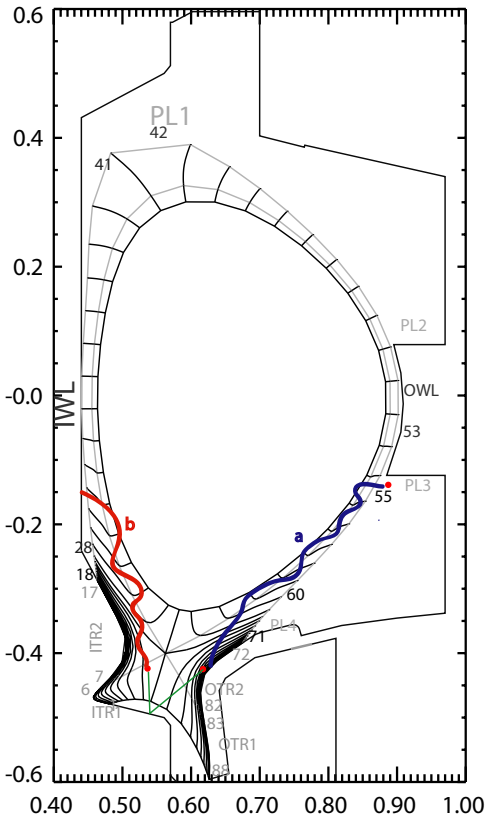

Figure 4-8: Cartoon of particle tracking. Single particle is launched with single recycling allowed. The sepxing array counts only the first entrance and the last exit cell. The parafxing array counts every cross in/outs on the separatrix.

target. The ion has experienced many crossings across the separatix in between cells $55 \sim 60$. The recycling neutral is launched from the target as a second particle.

second particle b The neutral emitted from the target has sufficient energy to pass through the PFZ and reach the wall. The neutral is reflected off the wall into the PFZ again and ionized there. The ion created in PFZ may cross the inner separatrix leg into the inner SOL and then enter the core. This run ends when the second particle strikes the inner wall.

The outer target and PL3 are the recycling sources which contribute to the impurity core penetration in this example. The differences in influxes on the separatrix made both by the sepxing and perpfxing are plotted for the particle a in Fig. 4-9. The sepxing has counted steps made only on cells 55 and 60 while the perpfxing has followed every step made across the separatrix.

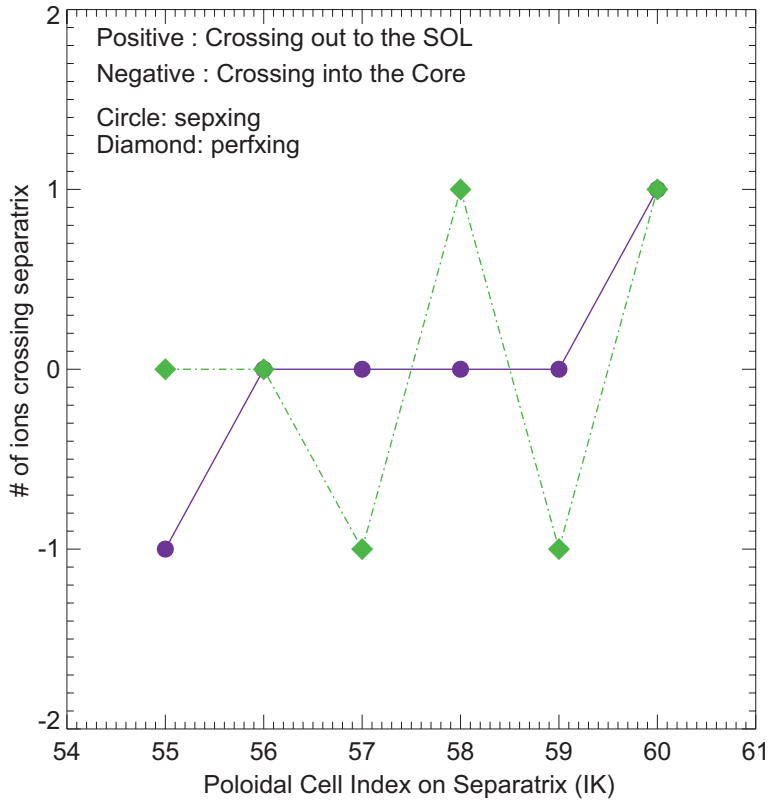

Figure 4-9: The difference between the sepxing and the perpfxing. The sepxing counts only the first entrance and the last exit steps made on the separatrix while the perpfxing counts every crossing steps.

4.4 Summary

The modifications of recycling descriptions and the implementations of diagnostics were reviewed. The purpose of this section is to help a reader get familiar with the utilizations of diagnostics presented in previous sections. A case used here as an example is modeling for the low density case: 40 neutrals are launched from the outside midplane with a total of 2,000 recyclings allowed. The total of 80,000 particles are followed in this run. Figure 4-10 shows impurity ion flow patterns generated by the parafxing and perpfxing vectors: the parallel and perpendicular ion flows are plotted separately. The length and thickness of the facecrossing arrows are proportional to the number of facecrossings. The perpfxing on the separatrix is expressed by solid-head arrows and it magnitude is multiplied by 4 and indicates that ions cross the separatrix into the core plasma from the outer midplane and move out of the core

plasma in the inboard side. The parallel ion flows show that the impurity ions flow from the outboard region to the inboard region in the SOL.

It is difficult, however, to obtain detailed information of the impurity ion flow pattern on the separatrix from this picture. For detailed information of impurity ion radial flow through the separatrix, the perpfxing or the sepxing data are plotted in an alternative way as in Fig. 4-11. The figure shows the perpfxing on the separatrix. The positive symbols are used for the radial facecrossings from the core plasma to the SOL and the negative symbols for facecrossing from the SOL to the core. The net radial facecrossings on the separatrix (estimated by the summation of the positive values and the negative values) are plotted by solid line which corresponds to the solid-head arrow vectors in Fig. 4-10. The average ionization states of ions crossing the separatrix are also indicated here by a gray scale. It shows that impurity ions move into the core mostly from the outer midplane in lower-Z states and move out to the SOL from the inboard region in higher-Z states.

Instead of the perpfxing, the sepxing array will be used through this thesis as the sepxing is used for the calculation of total number of ions entering core, i.e. the core impurity level. Fig. 4-12 shows the impurity ion radial flow on the separatrix with the sepxing. The hollow symbols represent for the radial facecrossings into the core and the filled symbols for the radial facecrossings out of the core into the SOL. This plot is useful to recognize which side/region of separatrix is favorable to the core influx and which one is favorable to the core outflux. It is indicated here that the impurity core influx is dominant over the outflux in the outer midplane while the outflux to the SOL is dominant in the inboard region.

It turned out that 2,570 ions of total 80,000 ions have entered the core plasma. These ions are counted by the sepxing arrays (the integration of hollow symbols). By adding these two sepxings (the hollow and filled symbols) one can obtain the net radial facecrossing pattern on the separatrix. Of course, the number of net facecrossings obtained by adding these two sepxings are zero, which implies that all the impurities are ionized in the SOL and the PFZ. The result is plotted in Fig. 4-13 which indicates the relative strength of crossing-in's or crossing-out's on each cell on the separatrix.

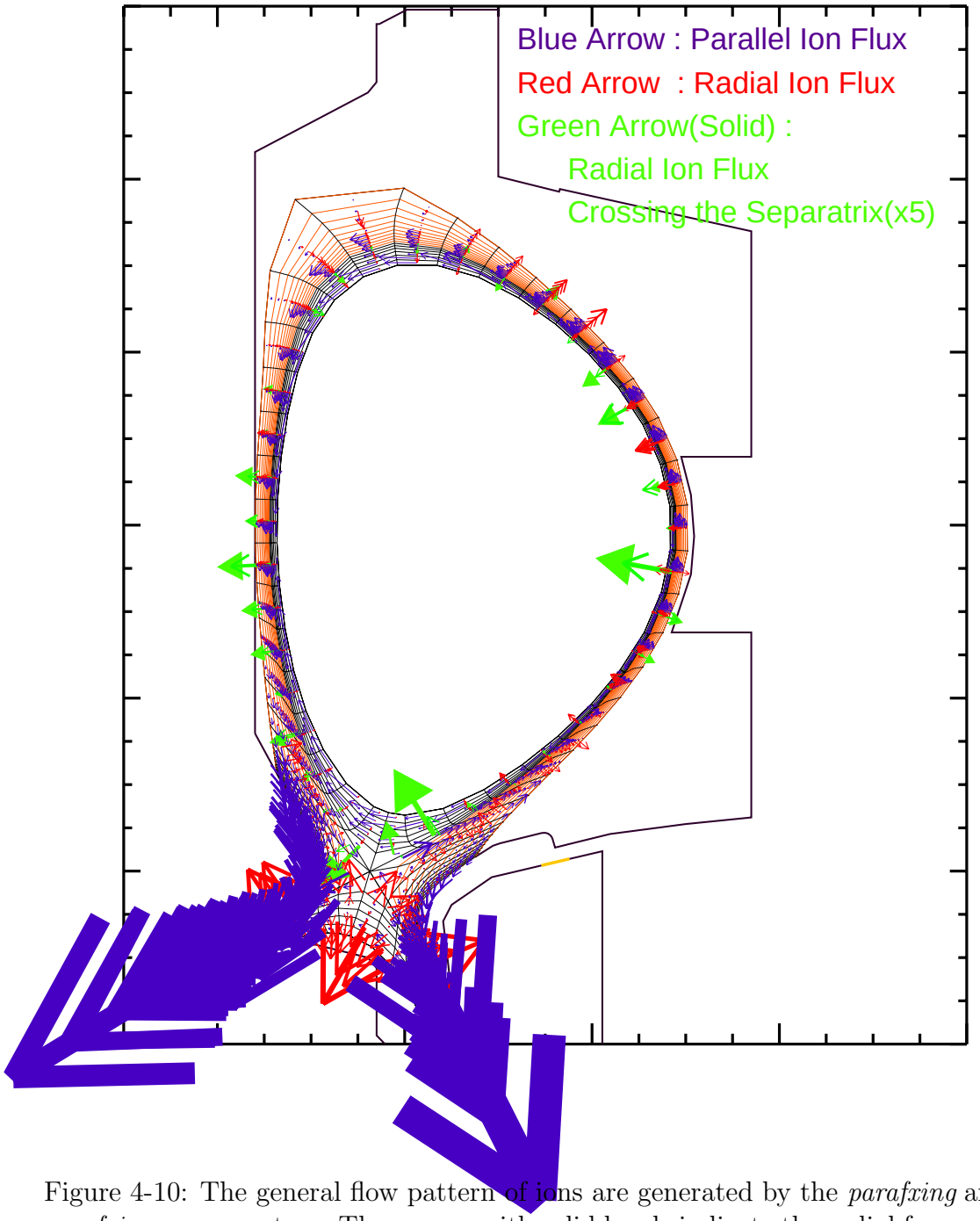

Figure 4-10: The general flow pattern of ions are generated by the *parafxing* and the *perpfxing* arrow vectors. The arrows with solid heads indicate the radial facecrossings on the separatrix and shows that ions cross the separatrix into the core from the outboard side. It is observed that there are impurity ion parallel flows directed from the outboard to the inboard region in the SOL.

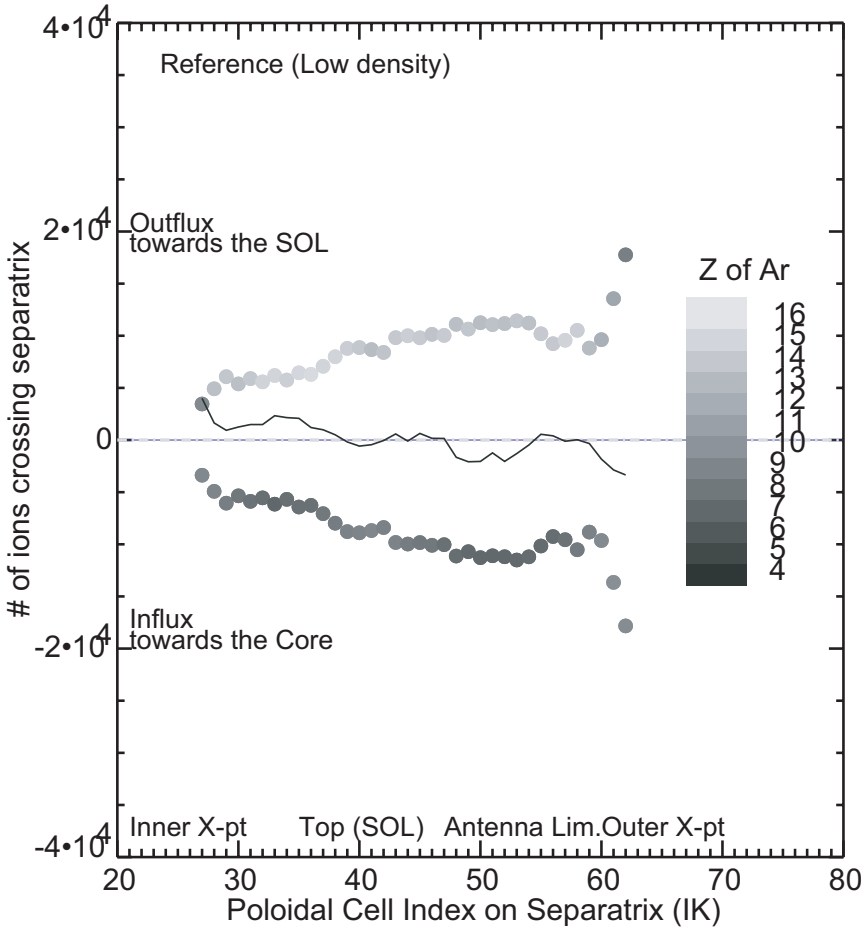

Figure 4-11: The perpfxing on the separatrix. The symbols above zero indicate radial facecrossings from the core to the SOL. The symbols below zero indicate radial facecrossings from the SOL into the core. The net radial facecrossings are represented by solid line (with the magnitude multiplied by four). The plot also shows that impurity ions cross into the core in low-Z state and cross out of the core into the SOL in high-Z state.

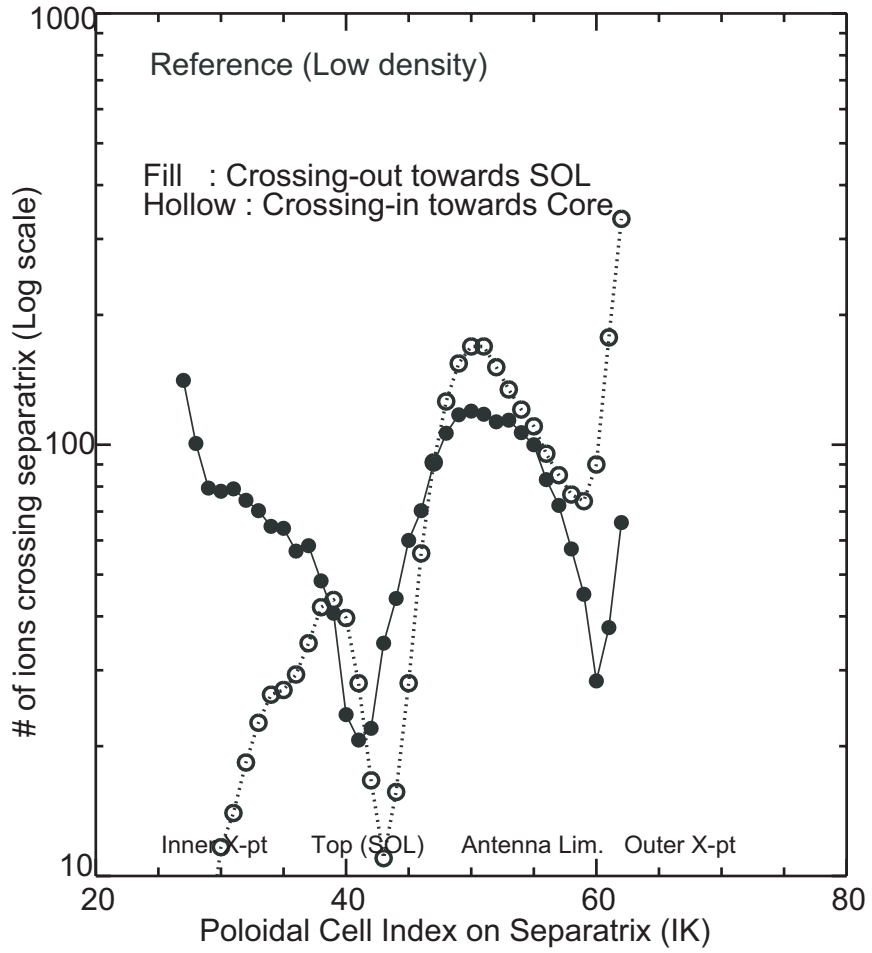

Figure 4-12: The sepxing on the separatrix. Each of crossing-in (hollow) and crossing-out (filled) components are plotted separately. The plot shows that impurity penetration into the core is dominant in the outboard region and ions flow out of the core from the inboard side.

Information of recycling neutrals is needed for the impurity retention study as the recycling neutrals are the sources of core penetrating ions. First one needs to know the distribution of recycling neutrals in the main chamber and targets. One then needs to estimate how many neutrals from each recycling source penetrate into the core (as ions). Fig. 4-14 shows the poloidal distribution of recycling neutrals and Fig. 4-15 shows what fraction of recycling neutrals reach the core plasma as ions.

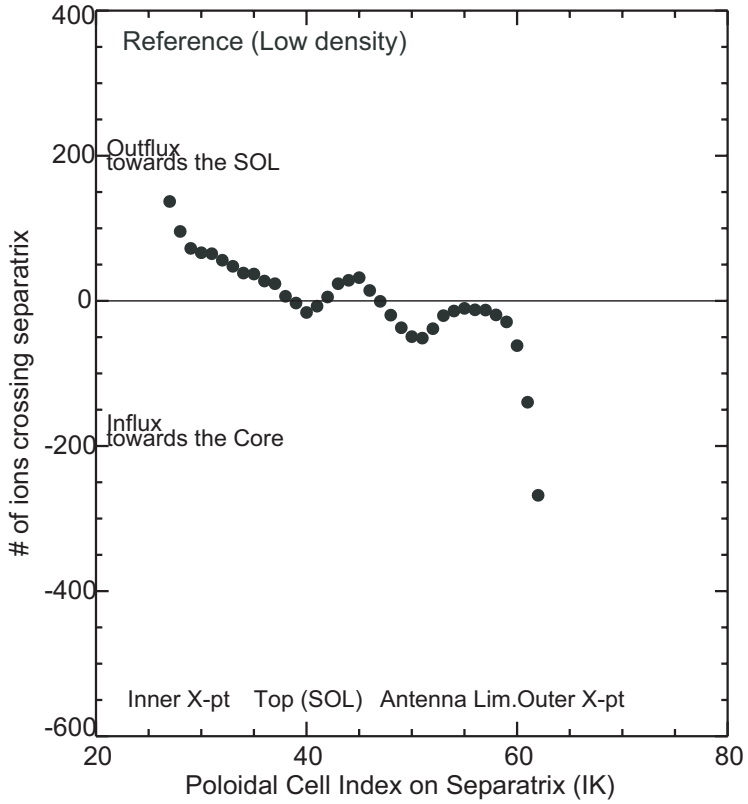

Figure 4-13: The net of sepxing is calculated by the summation of the positive sepxings and the negative sepxings. The plot indicates that the relative strength of influx is dominant over outflux in the outboard side.

Impurity ions recycle as neutrals at various locations: the inner target, inner wall surfaces, antenna limiter, outer target, and PL1,PL2, PL3, and PL4 locations. Of total of 80,000 recycling ions, $\sim 28\%$ ions are recycled on the inner target, $\sim 26\%$ on the outer target, $\sim 11\%$ on the inner wall surfaces, and $\sim 29\%$ on the outboard region. In the outboard region, $\sim 22\%$ of total ions are recycled at PL1,PL2,PL3 and PL4 and $\sim 7\%$ are recycled at the antenna limiter. All the recycling ions are launched as

neutrals at those locations into a cosine angular distribution with an energy of $0.03\,eV$.

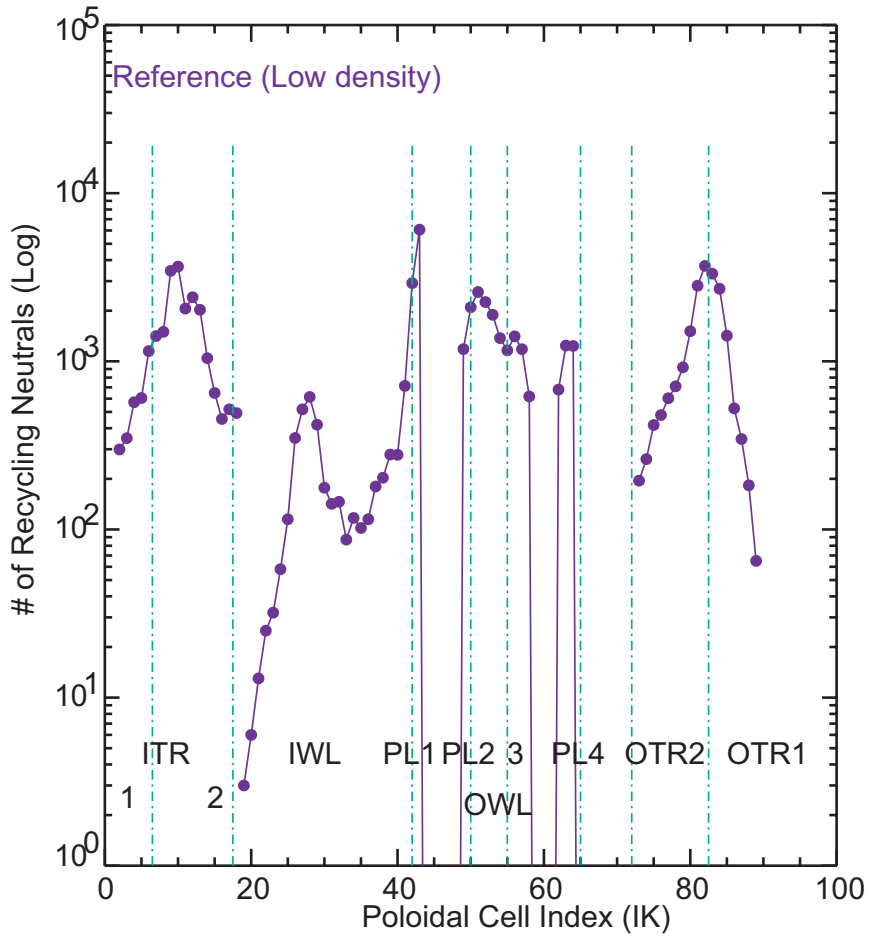

Figure 4-14: The poloidal distribution of recycling neutrals at the inner target, the inner wall surfaces, the antenna limiter, the outer target, and PL1,PL2, PL3, and PL4 locations. Among the total of 80,000 recycling neutrals, $\sim 28\%$ neutrals recycle on the inner target, $\sim 26\%$ on the outer target, $\sim 11\%$ on the inner wall surfaces, and $\sim 29\%$ on the outboard region.

Combined with the data stored in the diagnostic counters on the separatrix (Ch.4.3), it can be calculated that how many neutrals of recycling sources get into core plasma, i.e. screening of impurities (or the penetration factor). Fig. 4-15 shows the poloidal variation of the impurity screenings estimated with the penetration factor defined by

$$PF_k = \frac{\#\text{ of core entering ions originated from the k-source neutral}}{\#\text{ of neutrals recycled from k source}} \times 100(\%) \quad (4.5)$$

.

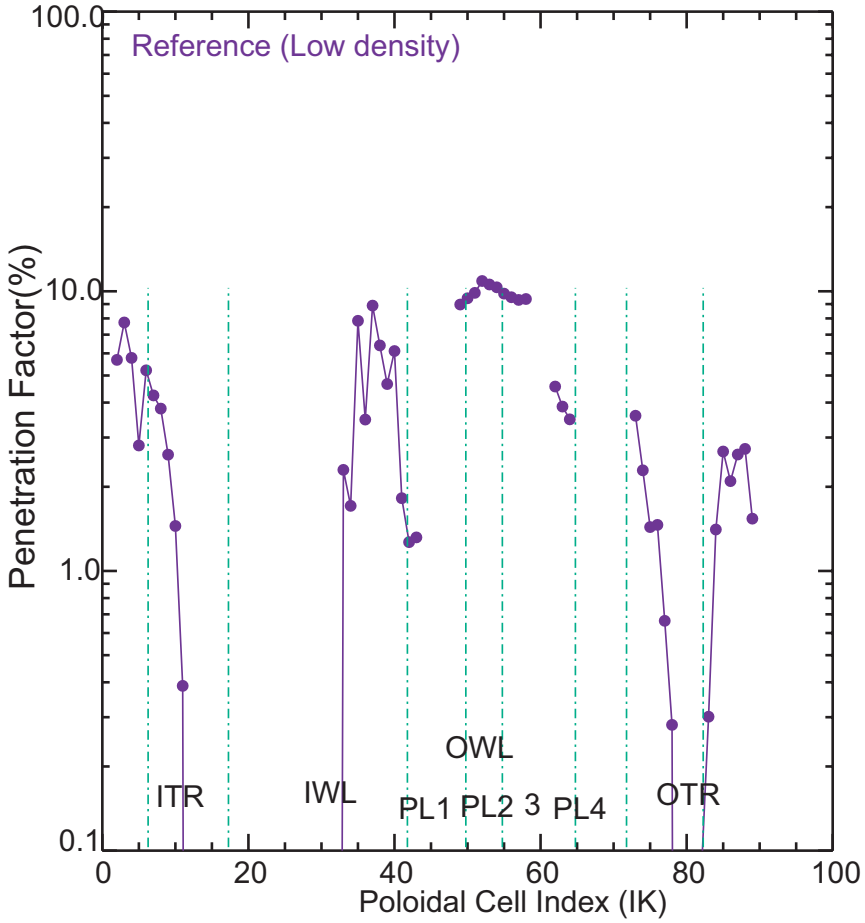

Figure 4-15: The screening of recycling impurities is measured by penetration factor (PF %). The PF is the ratio of the number of ions entering the core to the number of recycling neutrals. For example, out of 22,183 neutrals (or ions) recycling on the inner target 312 neutrals (after ionized) have entered the core plasma. Thus the inner target has a penetration factor of 1.4%.

For example, out of 22,183 recycling neutrals (or ions) on the inner target 312 neutrals (after ionized) have entered the core plasma. Thus the inner target has a penetration factor of 1.4%. In similar way penetration factors for other recycling sources are calculated: 0.6% for the outer target, 2.7% for the inner wall, 9.1% of the antenna limiter, 2% for the PL1, 9.8% for the PL2 (upper antenna limiter), 10% for the PL3 (lower antenna limiter), and 5% for the PL4. One can also estimate each recycling source's contribution to the core impurity level based on the total number of ions entering the core (in this case total of 2,570 ions out of 80,000 ions have entered the

core plasma). The inner target has 12%(= 312/2570 × 100) of contribution to the core impurity level, the outer target has 4.8%, the inner wall has 9.5%, and the antenna limiter (including PL2 and PL3) has 55.8% of contribution to the core impurity level.

Chapter 5

Background Plasma Description

The background plasma parameters such as density, temperature and parallel flow are prescribed on the DIVIMP computational grid (Fig. 3-1). The density and temperature profiles in the core are given by measurements from Thomson Scattering and GPC [41]. In each flux ring of the core region, a constant plasma profile along the field line is assumed. For the SOL plasma description, a simple 1-D solver based on onion-skin method (OSM [35]) was developed. The plasma description of the private flux zone (PFZ) is limited due to the lack of an analytic model. The current description of the PFZ plasma is made in an *ad hoc* manner, which tries to match known plasma parameters in that region.

In this chapter the details of the SOL plasma description by the 1-D OSM solver will be presented including an estimation of the solver validity. Ohmic L-mode discharges are modeled for low density ($\bar{n}_e = 1.14 \times 10^{20}\, m^{-3}$), medium density ($\bar{n}_e = 1.46 \times 10^{20}\, m^{-3}$), and high density, with an assumption of detachment, ($\bar{n}_e = 2.1 \times 10^{20}\, m^{-3}$).

5.1 Plasma Descriptions in the SOL

The basic principle of the onion-skin method is to treat the SOL flux surfaces as a set of individual flux tubes. The OSM solver solves the continuity, momentum and energy conservations equations along each single flux tube independently, i.e. the OSM treats

a flux tube as independent to adjacent flux tubes. This method assumes that the cross-field transport information is given implicitly within the boundary conditions. The boundary conditions in an OSM solver are typically specified across the targets and midplane with the density and temperature given by experimental measurement. The density and temperature are measured by Langmuir probes mounted on the targets, a vertical scanning probe (FSP) above the outer x-point region,a horizontal scanning probe (ASP) at the outer midplane, and a scanning probe at the inner midplane (ISP). The location of each probe in C-Mod is shown in Fig. 5-1.

The OSM solver in the current version of DIVIMP has one caveat. The OSM solver solves for a plasma parameter separately in the inboard region and in the outboard region and tries to match the two solutions at the mid-point. When the inboard and outboard targets have different boundary conditions, there can be a discontinuity in the solution at the mid-point[1]. To alleviate this problem an alternative solver has been developed in this study. The alternative solver is still based on the onion-skin method, but uses the electron heat conduction equation and the plasma pressure balance condition for the calculations of plasma temperature and density along the field line in the SOL. The solver first solves for the temperature using the electron heat conduction equation by starting from the inner target passing through the mid-point (the location of ASP) all the way to the outer target. The electron heat conduction is given as

$$q = -\kappa_e T_e^{5/2} \frac{dT_e}{ds} \ (W/m^2) \tag{5.1}$$

where the electron thermal conductivity, $\kappa_e (WeV^{-3.5}/m)$, is ~ 2000 (much larger than the ion thermal conductivity $\kappa_i \sim 60$), the electron temperature T_e is in eV and q is the parallel heat flux density (W/m^2). This model simplifies the physics in the SOL by assuming that: the electrons and ions are thermally well coupled such that the electron heat conduction equation approximates the transport of the total

[1]The latest updated solver now has fixed this discontinuity problem

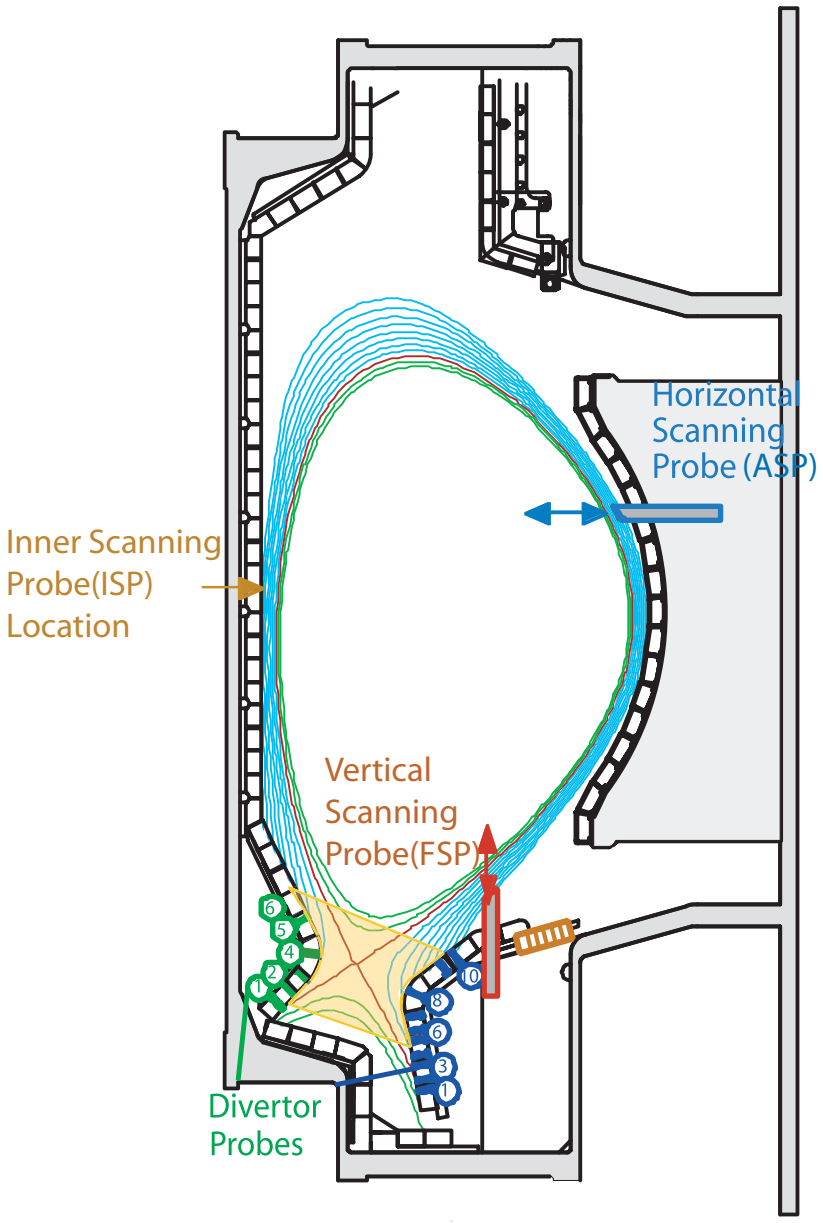

Figure 5-1: Poloidal location of diagnostic probes: divertor probes, FSP (vertical probes), and ASP (horizontal scanning probe) are used for the measurements of plasma density, temperature and flows. Recent installation of inner scanning probe (ISP) in the inner midplane wall allows measurements of the plasma parallel flow in the inner wall.

conducted power. Subsequently the assumption of $T_e \simeq T_i$ can be used. This is a reasonable approximation in the SOL of C-Mod given the high collisionality. It is also assumed that the SOL region between the inner x-point and outer x-point has a power source coming from the core while the regions below the x-points (in front of the divertors) have a power sink due to radiation losses. This can be expressed as

$$\begin{aligned} \frac{dq}{ds} &= Q \\ Q(W/m^3) &= \begin{cases} Q_{SOL}(>0) & : \text{ above the x-point} \\ Q_{rad}(<0) & : \text{ below the x-point} \end{cases} \end{aligned} \tag{5.2}$$

Q_{SOL} can be either a point source or uniformly distributed source along the SOL. The point source case assumes that all the power coming from the core enters the SOL at a single location (i.e. at the midplane). The uniformly distributed source case assumes that the power enters the entire SOL uniformly along a flux tube. These two very different conditions result in only a small difference (within $\sim 18\%$) in the temperature solution at the mid-point. However, the temperature profile obtained with the point source condition has a discontinuity in $\frac{dT}{ds}$ at the midplane. This gives a cusp-like shape to the thermal gradient and overestimates the thermal forces. Thus the uniformly distributed power source is assumed in this work.
The above two equations, Eqs. 5.1 and 5.2, are coupled as

$$\frac{5}{2T_e}\left(\frac{dT_e}{ds}\right)^2 + \frac{d^2T_e}{ds^2} = -\frac{Q}{\kappa_e T_e^{5/2}} \ . \tag{5.3}$$

To apply Runge-Kutta numerical method, the above second-order ordinary differential equation is rewritten as two first-order equations

$$f = \frac{dT_e}{ds} \quad \text{and} \quad -\kappa_e T_e^{3/2} f^2 - \kappa_e T_e^{5/2}\frac{df}{ds} = Q \tag{5.4}$$

The solver finds the solution at each grid point advancing from the inner target to

the outer target along the field line. In the course of procedure the solver checks the matching condition of the temperature at the midplane and at the target. By adjusting the input parameters of Q_{SOL} the solver tries to match the solution at the midplane with the measured temperature by the ASP within $\sim 3\%$. Similarly, the parameter Q_{rad} is adjusted in the outer divertor region to match the solution at the outer target with the temperature measured by the target mounted probe within $\sim 1\,\%$ error. After the temperature is found, then the plasma density and the parallel flow are calculated by the continuity and momentum equations as

$$\frac{d}{ds}(n_e v_p) = n n_o < \sigma v >_{iz} - n^2 < \sigma v >_{rec} \tag{5.5}$$

$$\frac{d}{ds}(n_e m v_p^2 + 2 n_e T_e) = -m n_o n_e v_p (< \sigma v >_{rec} + < \sigma v >_{cx}), \tag{5.6}$$

where T_e are given from the previous calculations, v_p is the parallel plasma flow (m/sec), and $\Gamma = n_e v_p$. The subscript 'iz' represents ionization, 'cx' for charge-exchange, and 'rec' for recombination. Information about the plasma neutral density, n_o in Eq. 5.13 is obtained from the neutral code EIRENE [47, 48] coupled with DIVIMP. The EIRENE has plasma density and temperature given as the input and calculates the plasma neutral density on the computational grid.

Input plasma parameters given as boundary conditions (filled symbol) and the probe measured values (hollow symbol) at the targets are shown in Figs. 5-2 and 5-3. Fig. 5-4 shows the plasma parameters measured by ASP probe (filled) and the plasma parameters calculated by OSM method (hollow).

The above 1D solver is applied only to the attached region. When the recycling of plasma becomes significant in front of the targets, collisions between plasma neutrals and ions become significant enough to cause plasma pressure to drop in that region. In this detached region the temperature drops to $1 \sim 2\,eV$ and the subsequent temperature gradient is negligible [43, 44, 45]. To prescribe the temperature and density profile in the detached region (outer targets for high density case and inner targets for all plasma cases), an approximation is applied in front of the target. This approximation is illustrated in Fig. 5-5. In this figure, the region between

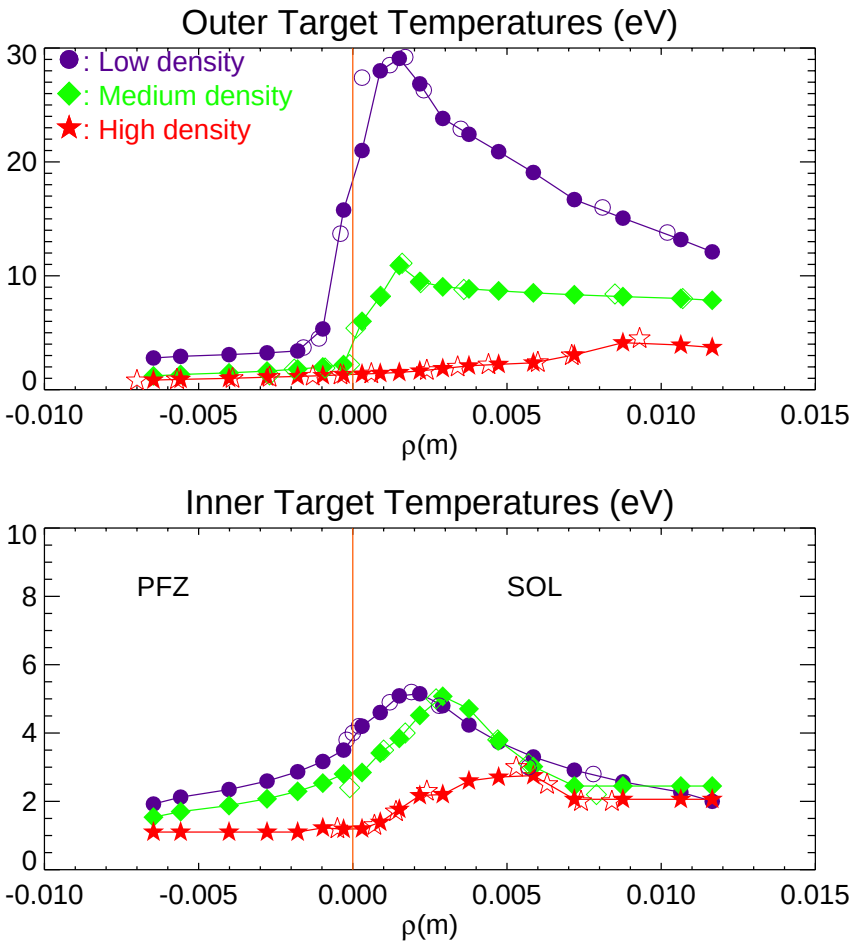

Figure 5-2: The target temperature is given as input (filled). The measured data is indicated with hollow symbol. The coordinate ρ is the distance outward from the separatrix at the midplane of the flux surface on which the measurement is made.

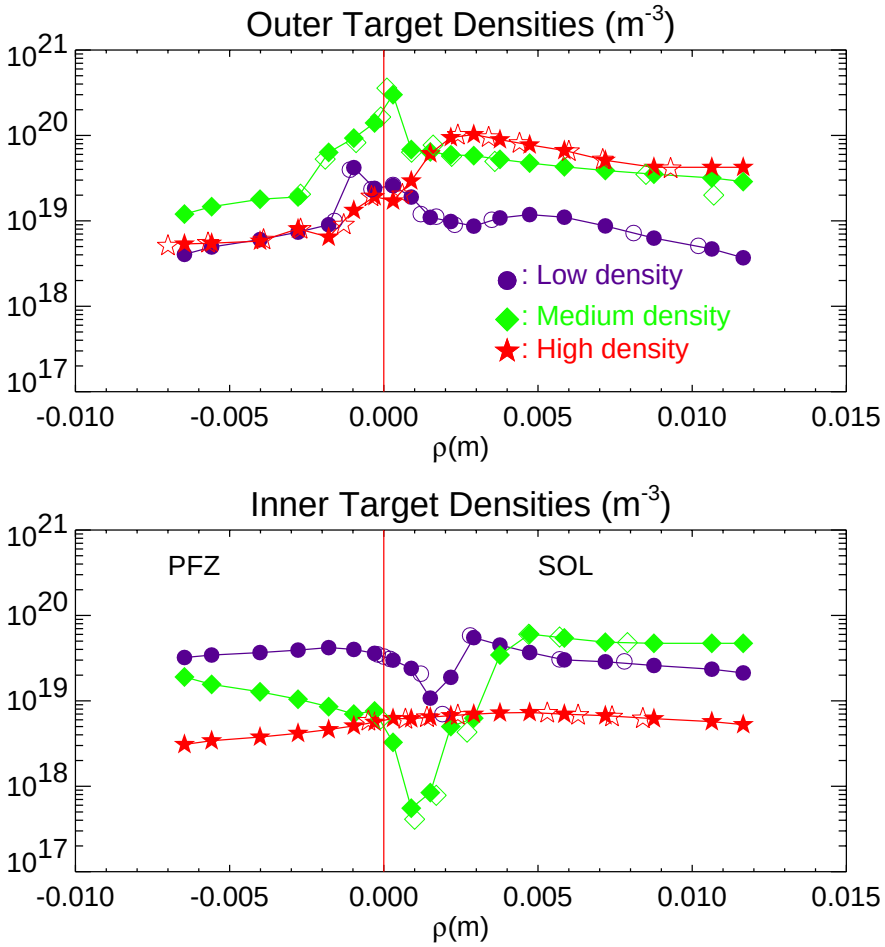

Figure 5-3: The target density is given as input (filled). The measured data is indicated with hollow symbol. The coordinate ρ is the distance outward from the separatrix at the midplane of the flux surface on which the measurement is made.

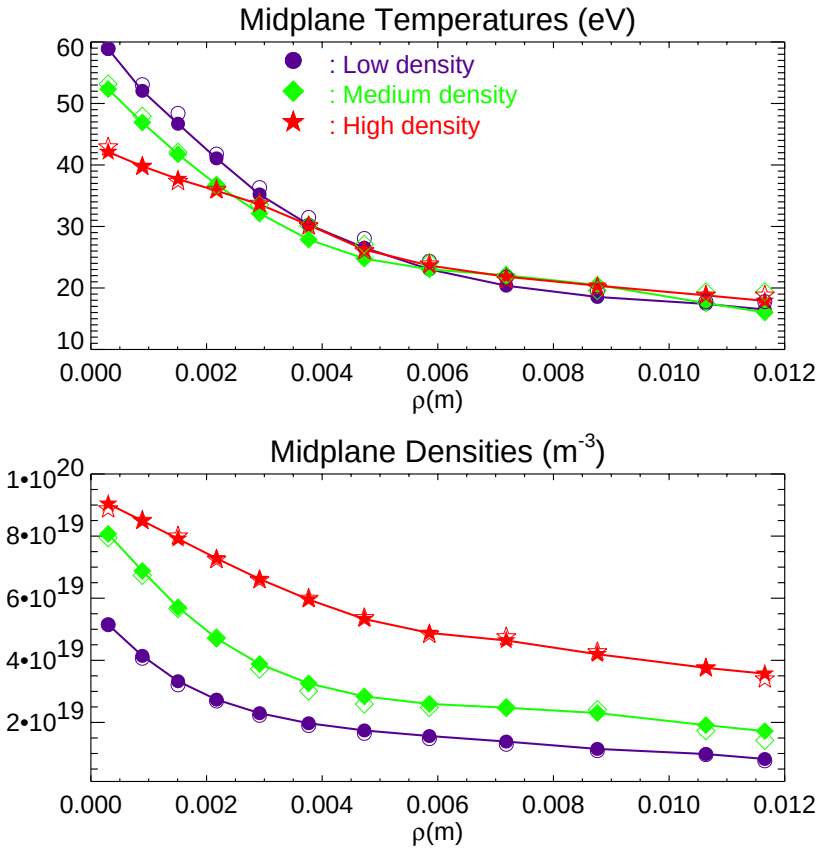

Figure 5-4: The density and temperature at the midplane are measured by ASP probe (solid). The values obtained from the 1D OSM solver is shown as hollow symbols.

$L_u \sim L_r$ is the constant pressure region. The pressure loss occurs in a narrow region, typically near the divertor plates and its size (along the field line) is defined by L_r, the distance away from the target (Fig. 5-5). The size of L_r is roughly estimated. First, the (R,Z) coordinate of the peak location of D_γ emission (the peak point is assumed to be the front line of the detachment) in the contour plot is provided as a function of radial location, $\rho(m)$, then find L_r-value (m), the distance along the field line, by converting that (R,Z) value into the parallel distance (m) from the DIVIMP grid. This approximation method is benchmarked by comparing the L_r values to the ones measured precisely by the utilization of D_γ inversion technique based on 'reconstructive OEDGE modeling' [50]. Fig. 5-6 shows the comparison of the L_r(m) values of the current model and the benchmarked model. In this case the detached inner target for the medium density case is used. The result shows that the current approximation gives a reasonably good estimation of the detachment front location. For the high density case which has detachment at the outer divertor, the sensitivity of this method has been investigated. The estimated value of L_r in the outer divertor corresponds to $\sim 70\,\%$ of L_x, the parallel distance from the target to the x-point. As this fraction is varied between $60 \sim 80\,\%$ of L_x, the compression ratio is found to be varying as $c_z \sim 23 - 27$, which is comparable to c_z estimated in the experiment, ~ 30. When the size of L_r is reduced to a size less than $50\,\%$ of L_x, the compression ratio increases by a factor of ~ 2 higher than the experimental value, $45 \sim 60$.

For the size in radial direction, the pressure loss region is defined to be within the first three rings of the grid (IR=8-10 in Fig. 3-1), which corresponds to $\sim 3\,cm$ along the target from the strike point to the upper nose. Calculated density, temperature, and parallel flow profiles in the SOL are plotted in Figs. 5-7, 5-8, and 5-9.
In Fig. 5-9, the parallel plasma flow values measured at three locations (inner wall by ISP, outer midplane by ASP, and near outer divertor by FSP in Fig. 5-1) [46] are marked for comparison. Measured plasma flows are larger than the calculated ones by a factor of ~ 3 in the inboard region. A combination of Pfirsch-Schluter ion currents plus pure toroidal rotation could explain why the measured flows are larger than the modeling (the current 1D model doesn't include such aspects of transport) [49]. In

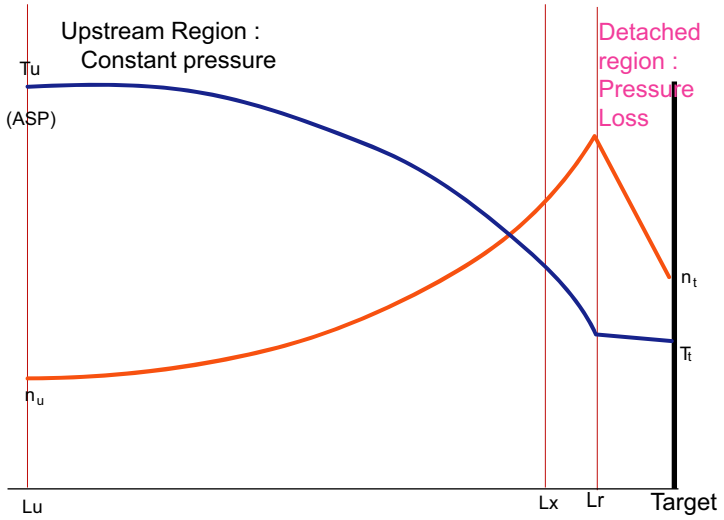

Figure 5-5: Approximate description of divertor region where pressure loss exists. This picture shows a flux tube on which the electron heat conduction equation is solved. The constant pressure condition is applied the region above L_r. In the region below L_r, in front of the target, recycling or detached model is assumed where the pressure drops rapidly and temperature gradient is negligible.

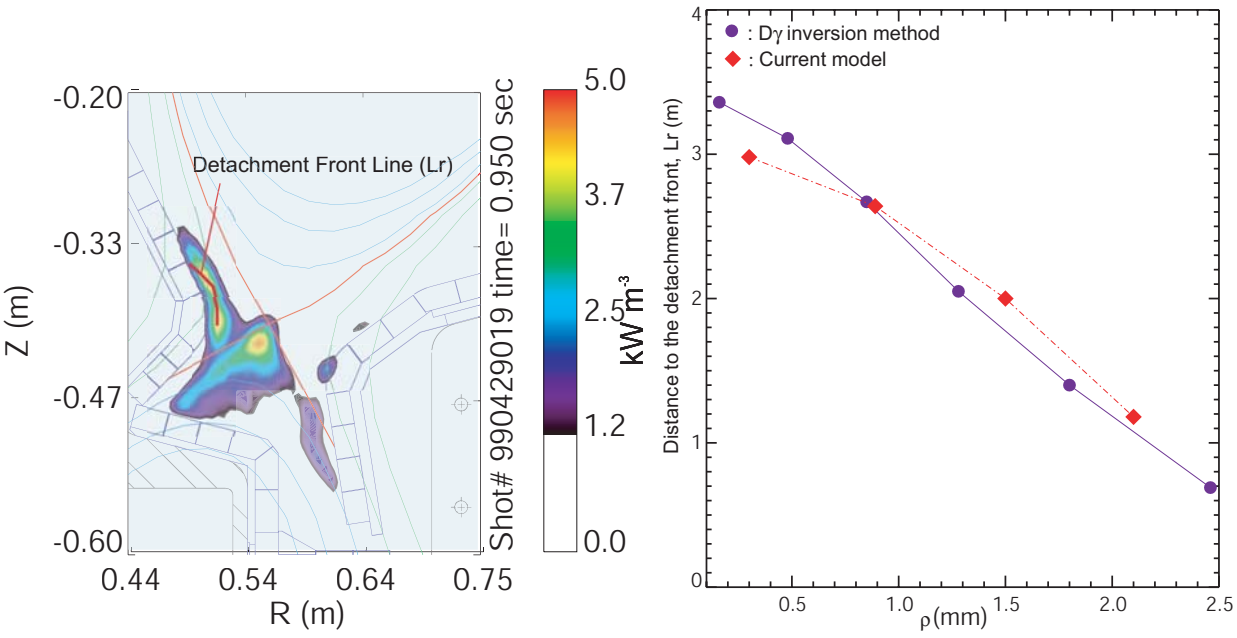

Figure 5-6: Approximate estimation of the distance to the detachment front line (L_r). (R,Z) value of the peak location of D_γ emission signal (left panel) is assumed to be the detachment front line and converted into L_r (m). The current method of approximating the distance to the detachment front line (square) is benchmarked (right panel) to the estimation based on 'reconstructive OEDGE modeling' (circle) [50].

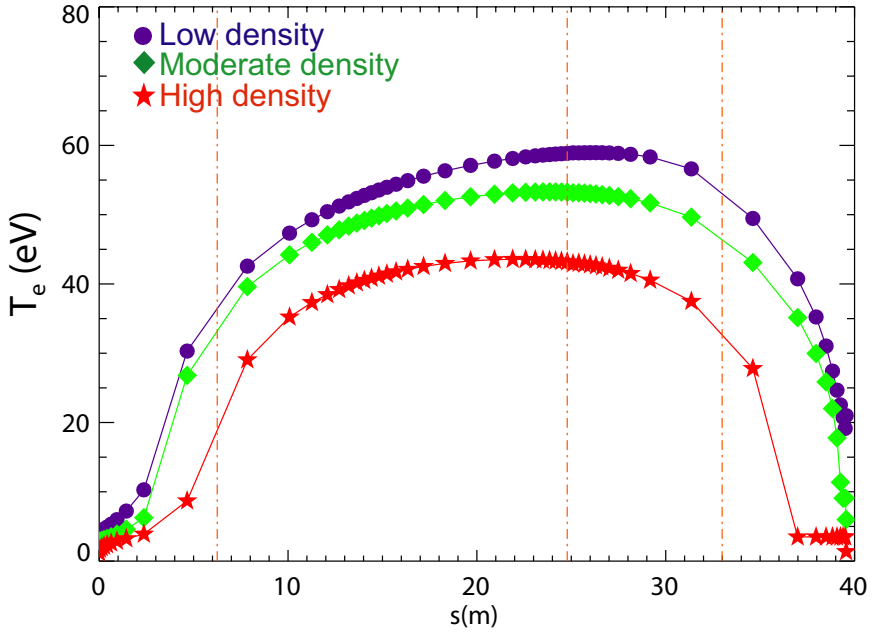

Figure 5-7: Temperature profiles obtained from the current 1-D OSM method. The radial location is the first flux tube outside the separatrix.

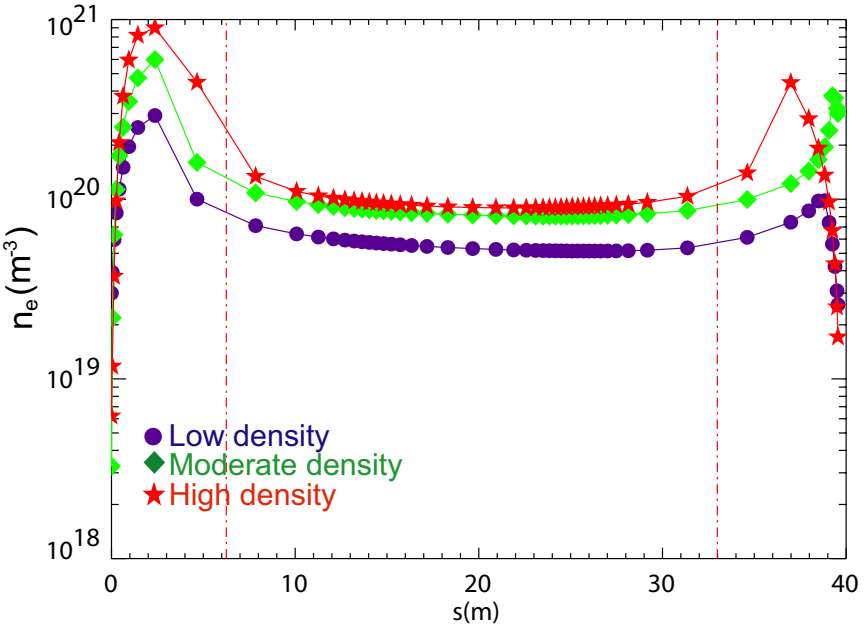

Figure 5-8: Density profiles obtained from the current 1-D OSM method. The radial location is the first flux tube outside the separatrix.

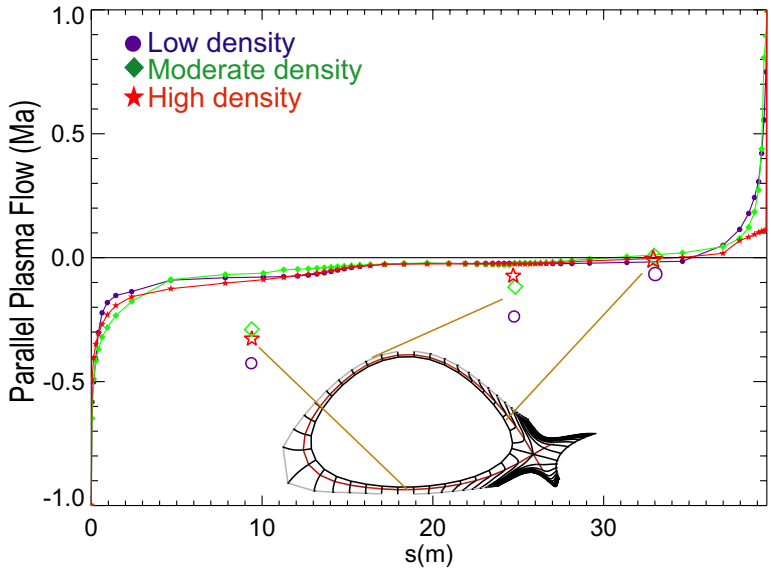

Figure 5-9: Parallel plasma flows (Ma) along the SOL for different discharges. Experimental measurements [46] by FSP, ASP and ISP (Fig. 5-1) for similar density plasmas are indicated by hollow symbols.

addition, the current flow model for detached case (near the outer target in star symbols) results in relatively weak flow due to the momentum loss of ion from collisions with neutrals.

Notice that the above 1D plasma solver uses Q_{SOL} as input parameters. For a validation check, the power deposited into the entire SOL volume is estimated and compared with the experimental estimations in C-Mod [46]. In the modeling the entire SOL power deposition is calculated by integrating the Q_{SOL} on each flux tube across the SOL, $\int Q_{SOL} dv$ (dv is the volume of each flux tube). And the comparison is plotted in Fig. 5-10.

Unlike in the SOL, the plasma descriptions are limited in the private flux region due to the lack of an analytic model. The experimental measurements for the density and temperature profiles have yet to be developed. Only the moderate density case has an estimation of the profiles for n_e and T_e made by 'empirical reconstructive' OEDGE modeling [50] where the plasma parameters are inferred by matching D_α, D_γ signals in C-Mod divertor [51], and Stark broadening measurements. For the low density and the high density (detached) plasmas, a parabolic density pro-

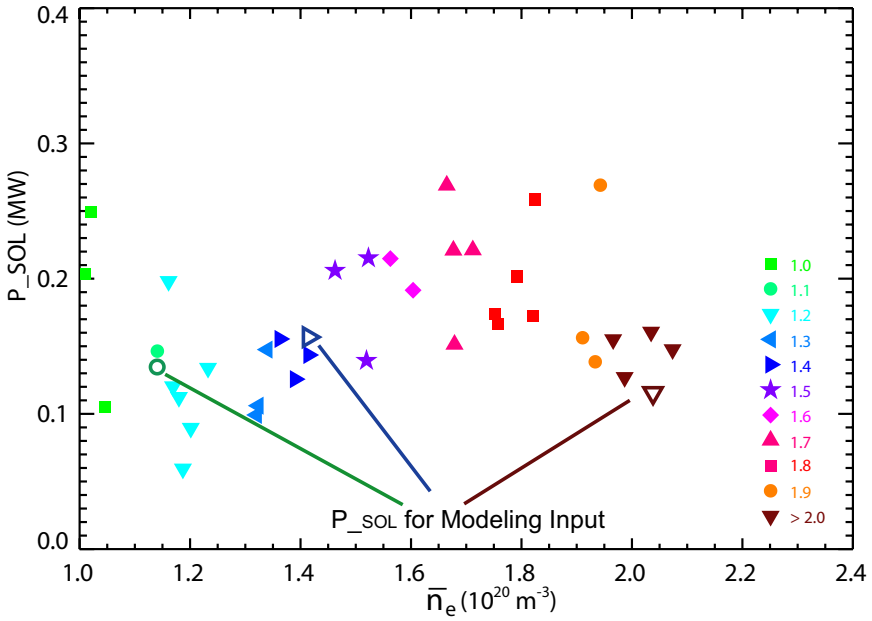

Figure 5-10: $\int Q_{SOL}$ of the modeling input parameter is compared with experimental estimation of the power conducted into the entire SOL region.

file is assumed. The target densities are given by the probe measurements and the peak density estimated by D_γ measurement [51] are specified at the mid-point along the field line in the private flux region. The temperature profiles are approximated by interpolating between the inner and outer target. Note that nearly flat profiles for density and temperature are assumed for the detached model since a negligible plasma influx from the common flux region (the SOL) is expected. Fig. 5-11 shows the corresponding PFZ plasma density and temperature profiles. Compared to other two cases, the low density model has the higher uncertainty in the description of the private flux plasma. The investigation of modeling sensitivity to the private flux condition for the low density is discussed in the next section.

5.2 Sensitivity of the Modeling to the Private Flux Plasma

This section will investigate the sensitivity study of modeling by monitoring variations in the impurity ion influx patterns on the separatrix (i.e. sepxing). The uncertainty of

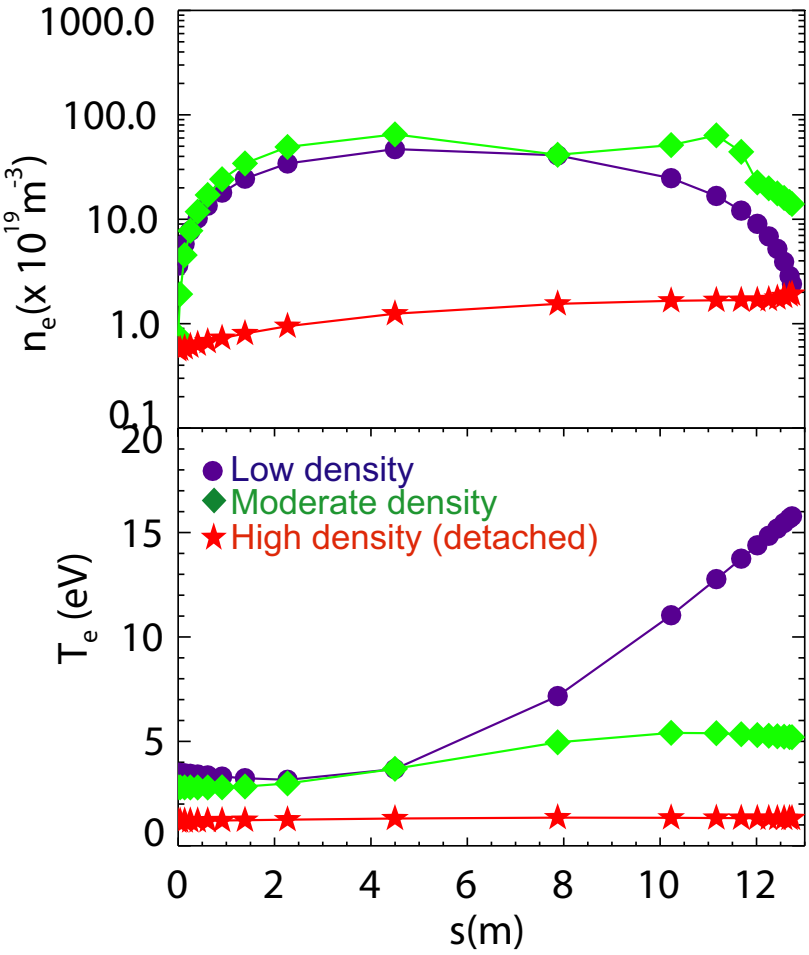

Figure 5-11: Plasma density and temperature profile specified in the private flux zone in the current model. Profiles of n_e and T_e estimated by data analysis of as D_γ emission profile (S. Lisgo) are available for the moderate density case.

the private flux plasma description for the low density is discussed here. The reference private flux plasma has a parabolic density profile with the peak value of $5 \times 10^{20}\, m^{-3}$ at the mid-point. The reference plasma flow has the flow stagnation region in most of the private flux region except for a finite flow in front of the targets. For the study of sensitivity to the density, the peak of the reference density has been increased by a factor of 2 and for the flow sensitivity a finite amount of flow is imposed in the stagnation region. Fig 5-12 shows the flow imposed in the private flux region for the flow sensitivity study.

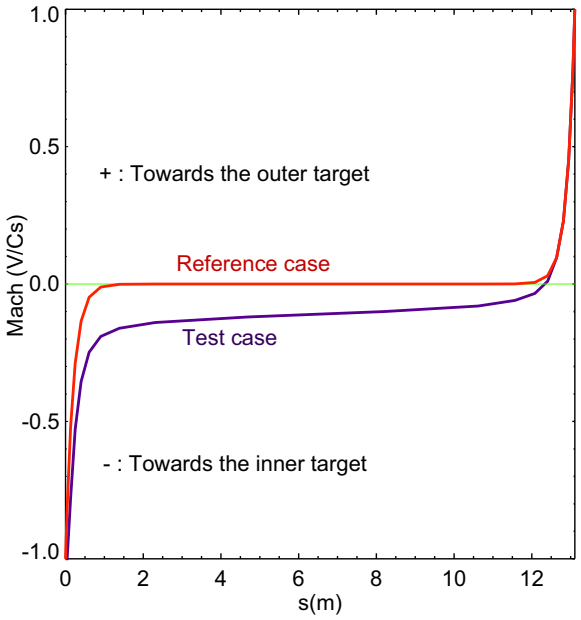

Figure 5-12: The plasma flow used for the sensitivity study. The reference case has the flow stagnation region in most of the private flux region except there is a finite flow in front of the target. For the sensitivity study, a finite plasma flow directed toward the inner target (negative Ma flow) is imposed.

The result of the sensitivity study is shown in Fig. 5-13 which shows the change in the sepxing as the PFZ condition changes. The sepxing profile is not altered much by the variation of the PFZ plasma: the influx from the antenna limiter region and from the x-point region are comparable for all cases. Only a small change in the magnitude of the sepxing near the x-point (cells 61-63) has occurred.

Fig. 5-14 gives a quantitative estimation of the sensitivity. The summation of the negative values of the sepxing in Fig. 5-13 for a net influx is used in this figure. The

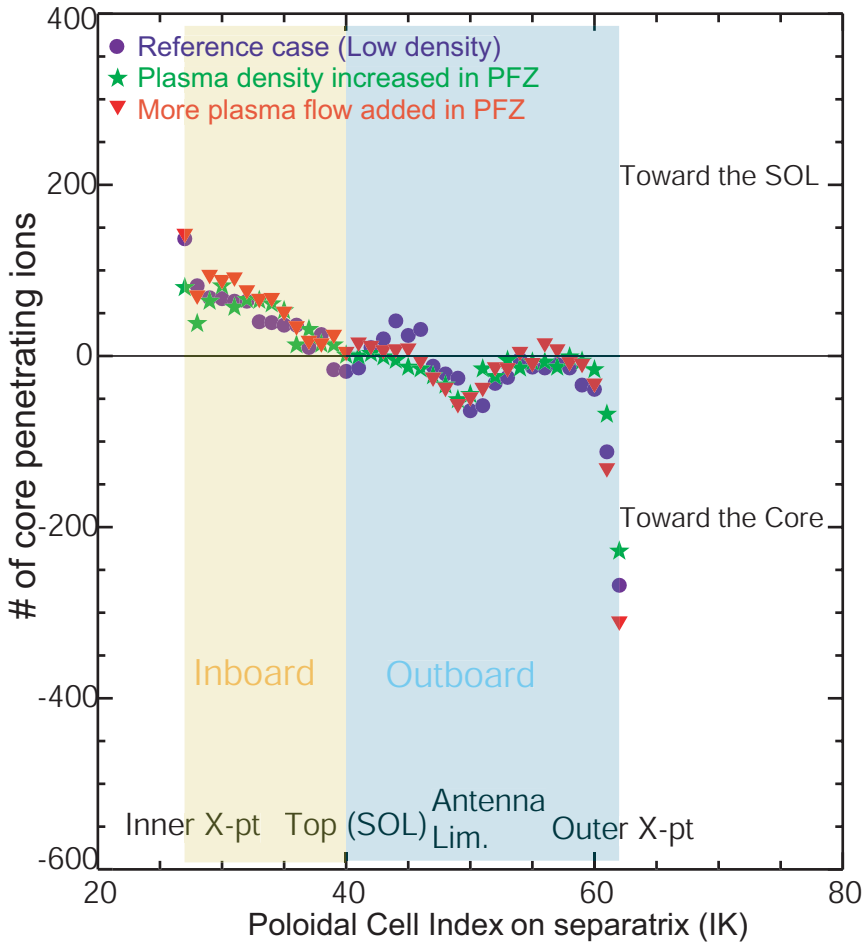

Figure 5-13: The change in the sepxing profile for the different PFZ condition. For the sensitivity study, the PFZ plasma density is increased (Star) by a factor of 2 and the negative parallel flow (toward the inner target) is imposed (Triangle) in the flow stagnation region. Only a small change ($\leq 25\,\%$) in the magnitude of the sepxing near the x-point (cells 61-63) occurs as the PFZ condition varies.

reference case has a net flux of 794. The net influxes for other cases are normalized to the reference value (794).

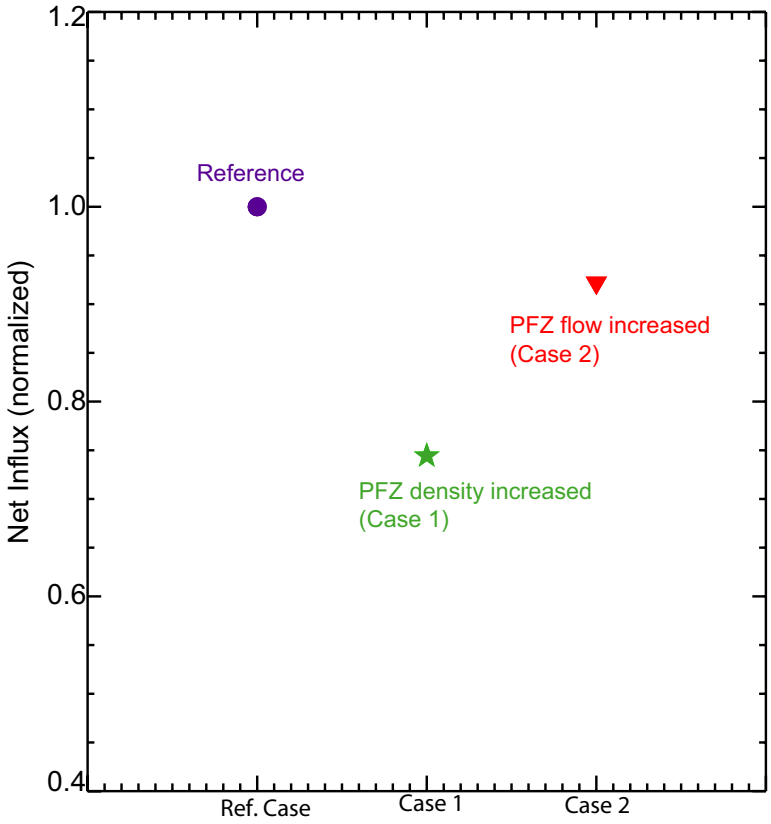

Figure 5-14: The changes in the net influx (defined here as the integration of the negative sepxings in Fig. 5-13). The increased PFZ density give rise to the reduction of the net influx by $\sim 25\,\%$ while the increase in the PFZ flow reduces the net influx by $\leq 10\%$.

The increase of the private flux density (by a factor of 2) results in the reduction of net influx by $\sim 25\,\%$ while the increase of the private flux flow reduces the net influx by $\leq 10\,\%$.

Chapter 6

Modeling Results

This chapter presents the DIVIMP modeling for impurity screening behavior observed in the experiment (introduced in Ch.2). Modeling has been performed for both the non-recycling and recycling cases. The non-recycling case is presented in section 6.1 and the recycling case in section 6.2. Underlying physics related to impurity retention will be explored in chapter 7.

6.1 Non-recycling Modeling

Experimental observations of non-recycling impurity screening [19] were made by using a nitrogen gas puff at different poloidal locations. As the gas puff location was varied from the inner midplane to the outer midplane and to the divertor region the core impurity level was found to change. Outboard gas injection had a much greater influence on core impurity levels than inboard injection. Core impurity densities were at least a factor of 20 greater for the outboard injection case than the case where the impurities were injected at the inner wall. In DIVIMP modeling, C impurities were used for both N_2 and CH_4 due to the lack of atomic data availability. To simulate non-recycling behavior, the following boundary condition is applied in the modeling: when the ions reach the wall surfaces and the targets they are discarded. In this study 4,000 C neutrals are injected with 0.03 eV energy into individual cells around the SOL (poloidal cell index IK is indicated in the left panel of Fig. 6-1) and the number of

impurities penetrating into the core plasma is counted to yield the penetration factor (PF) of each cell. The penetration factor of cell IK is defined as

$$PF_{IK}(\%) = \frac{\#\text{ of ions entering core from a cell IK}}{\#\text{ of neutrals injected into a cell IK}} \times 100\,. \tag{6.1}$$

We note that a different definition of PF was employed in Ref. [19], however, the focus here is on the patterns and trends which are expected to be fairly similar, based on either definition. The right panel of the figure shows the poloidal variation of the penetration factor.

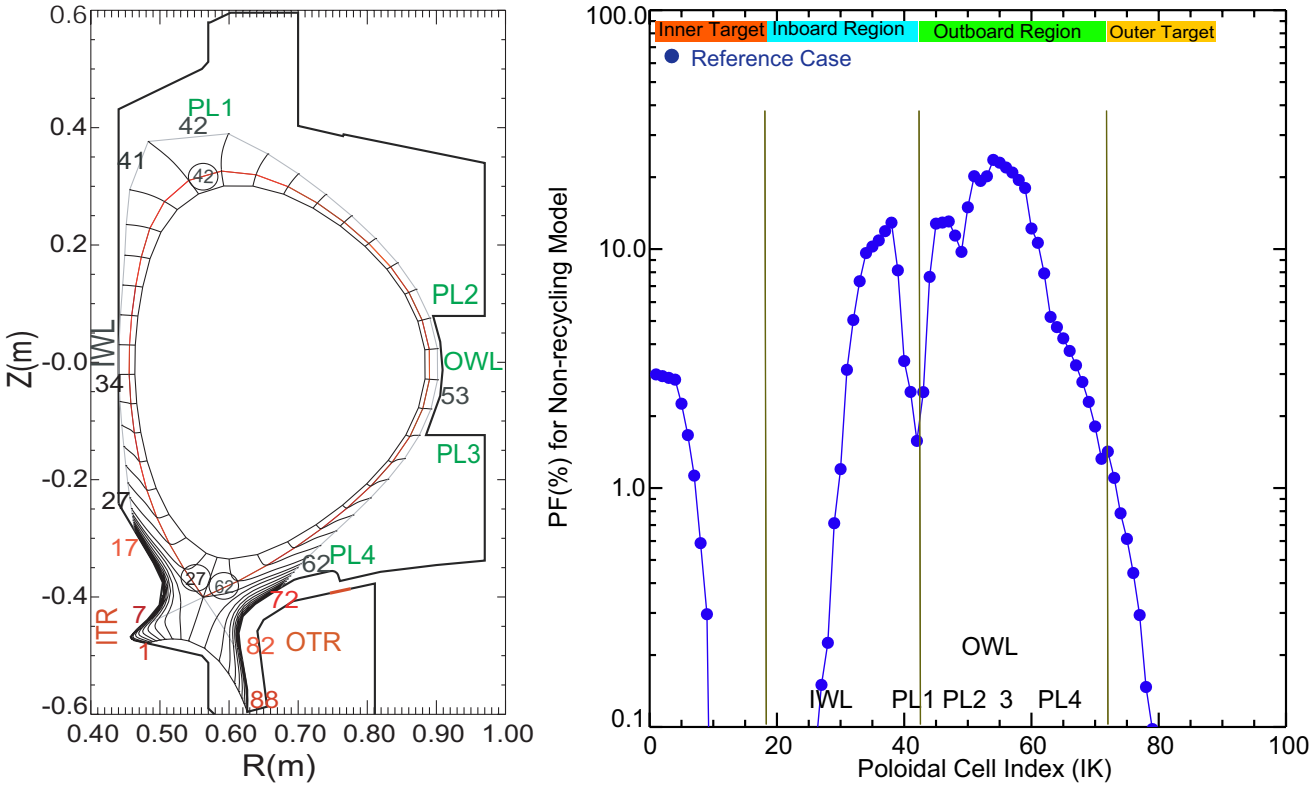

Figure 6-1: Calculation of poloidal variation of impurity penetration factor (PF). 4,000 test impurity neutrals are injected into each cell of the edge along the SOL (Left Panel). The cell index starts from the inner target (1) and goes all the way to the bottom leg of the outer target (88). The resultant poloidal variation of the PF for non-recycling model is shown in the right panel.

It is shown in Fig. 6-1 that the impurities injected from the inboard region are screened better than those injected from the outboard region, i.e. PF of an inboard

region cell is lower than PF of an outboard region cell. PF of the divertor plate is lower than the inboard PF in this model. For the quantitative comparison of screening between the inboard and outboard regions the regional PF is calculated by averaging over a range in source locations indicated in Fig. 6-1 (left panel). For example the averaged PF of the inboard region is calculated as

$$PF_{inboard}(\%) = \frac{\text{\# of ions entering core from cells 18-40}}{\text{\# of neutrals injected into cells 18-40}} \times 100 \tag{6.2}$$

and similarly for the outboard PF and target PF over the corresponding regions. The resultant averaged PF (%) is 3.6 for inboard, 11 for outboard, and 0.7 for divertor sources, which is consistent with the experimental trends seen in Fig.5 of [19]. The ratio of the outboard PF to the inboard PF is, however, lower ($\sim$ 3) compared to the ratio measured in the experiment, $\sim$ 20. It is suggested that the increase of the current modeled flow to the level of measure flow and the increase of injection energy of the impurity neutral may alter this ratio. The effects of such parameters will be investigated in Ch. 7.

6.2 Recycling Modeling

Contrary to non-recycling model, recycling model allows impurity ions to be recycled on the walls and targets. In the recycling case, all the ions reaching the wall and target surfaces are injected back into the plasma as neutrals. This section compares the recycling model to experiments through density dependence of impurity compression, c_z, and characteristics of recycling impurity screening.

6.2.1 Compression Ratios of Different Plasmas

The compression ratio for Ar is defined in section 2.3 and calculated for the three different background plasma cases. For the modeling of recycling impurities, 40 neutrals are injected initially from the outside midplane (near the cell 53 in Fig. 6-1)

with energy of 0.03 eV. When the ions reach the walls they are injected back into the plasma grid as recycling neutrals with room-temperature energy of 0.03 eV. For the impurities recycling on the target, the injection energy of recycling neutral is determined based on the calculation of particle and energy reflection coefficients (refer Sec.4.2.2). A total of 2,000 recyclings (for each of the forty initial injection neutral) are allowed from the various locations such as the targets and wall surfaces (thus a total of 80,000 particle-histories are followed). The code calculates the compression ratio as the ratio of impurity neutral density estimated in the plenum grid (Fig. 3-1) to the impurity ion density estimated as the total number of impurities in the entire core cells divided by the total volume of those cells. Fig. 6-2 shows the values of c_z observed in experiments and modeling.

It is observed in the experiment that c_z increases as the line-averaged plasma density increases (up to $c_z \sim 100$) and drops as plasma detaches. It is also found that the open-bypass reduces the compression ratio by a factor of two. The general trend of c_z is reproduced in the modeling within a factor of two: the modeling values are lower than the measured c_z's and the effect of open-bypass is less than the experiments. A couple of explanations of quantitative disagreements are given [52, 53]: first, a local experimental c_z is measured at a *closed port* in the divertor which is believed to result in a higher neutral pressure than a toroidally averaged c_z, and secondly the leakage gap estimated in the model may be overestimated as it is based on free-molecular gas conductance.

6.2.2 Characteristics of Recycling Impurity Screening

Recycling impurities are believed to travel around the machine without being lost to the walls or targets and to be recycled at various locations. If a small amount of gas is puffed (typically $\sim 10^{17}$ Ar atoms were injected in the experiment [19]) and many recyclings are allowed, then the impurity core level may not see the effect of change in injection location. This was observed in the experiments with Ar impurities [19]; The Ar impurity ion density in the core was independent of the initial argon gas puff location. To simulate this, 40 Ar neutrals are injected at three different locations and

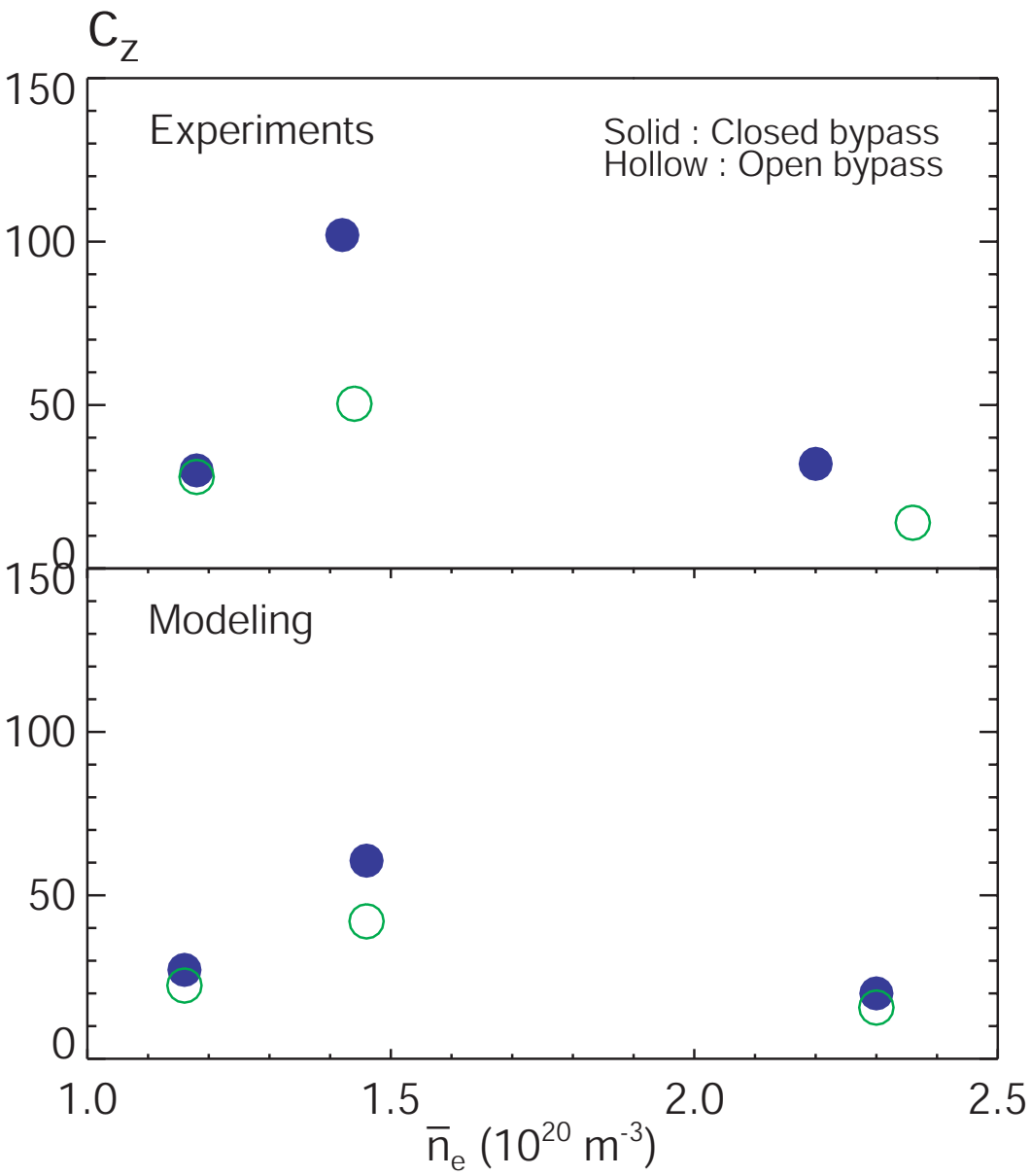

Figure 6-2: Density scanning of compression ratio of Ar impurity. The modeling has reproduced c_z's dependency on plasma densities within factor of two.

2,000 recyclings are allowed in the modeling. The injection locations are inner midplane, outer midplane (outside the cell 53 in the grid figure of 6-1), edge of the outer divertor (near PL4 in the grid figure of 6-1), and the private flux region. Modeling results are summarized in Table 6.1 showing that the compression ratio is insensitive to the injection location.

Injection Location	Inner midplane	Outer midplane	Divertor
c_z	63.2	60	61

Table 6.1: Recycling impurity core level is independent of the injection location.

In addition to the compression ratio, we have also investigated the time dependence of the Ar ion core density on the injection location and its subsequent evolution to steady state. Fig. 6-3 shows the time evolution of the core Ar level for different injection location. In the model and experiment impurities launched from the outboard (inboard and divertor) initially lead to a core Ar level higher (lower) than the steady state value. As the number of recyclings increases in the model the core Ar dependence on initial launch location disappears as seen in the experiment (Fig.3 of [19]). The result indicates that impurities are initially localized near the puff location. Because of the poloidal variation in PF value the localized puffs lead to different core levels. Over a number of recyclings the Ar redistributes poloidally such that less Ar is in the outboard SOL and more is in reigions of lower PF. If we calibrate the equilibrium time in the model (which is '400' recyclings) to the one in the experiment (that is $\sim 20ms$), we obtain a recycling time scale of $\sim 50\,(\mu sec/\text{recycl.})$. Thus, each Ar travels a small distance between recyclings, of order 0.1 m.

The above experiment, however, did not measure the distribution of recycling neutral sources and their relative importance in determining the core impurity levels. On the other hand, the modeling estimates the recycling source distribution in poloidal plane and calculates each source's contribution to the core penetration (the penetration factor). The location of each recycling source is indicated in the left panel of Fig. 6-1: recyclings on the inner wall (IWL), on the outer wall vessel (PL1,PL2,PL3,

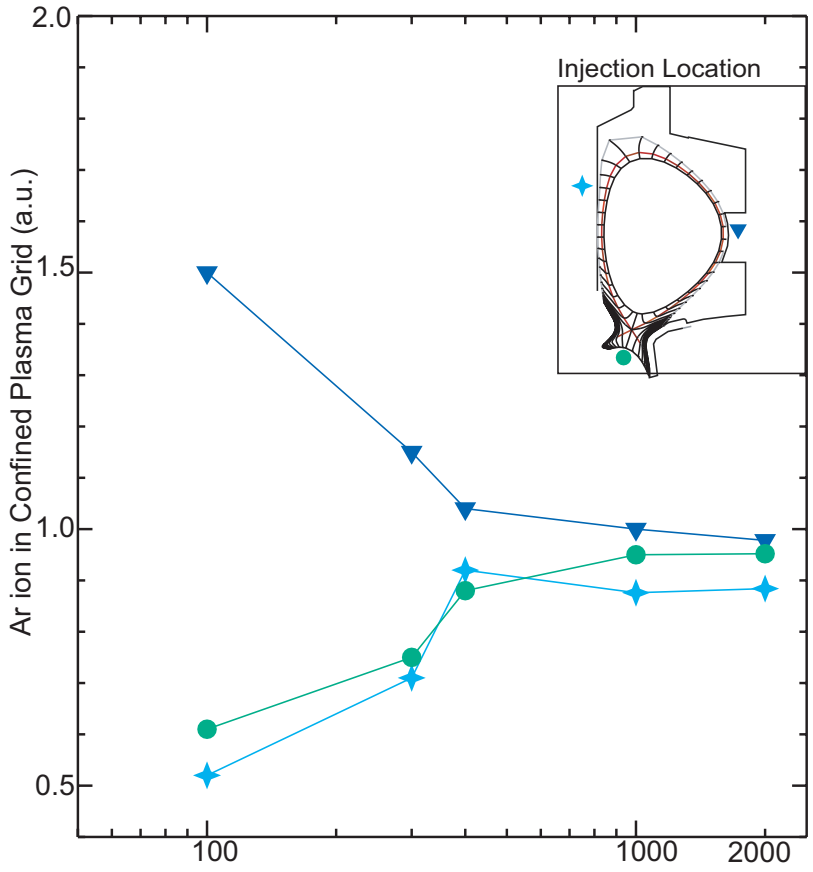

Figure 6-3: Ar core density is dependent on the injection location in earlier stage of the run where the recycling sources are comparable to the number of initial puffing neutrals. As the recycling sources become dominant over the initial neutral source, it becomes independent of the injection location.

PL4, and OWL), and targets (details of the impurity ion recyclings are described in Ch.4). Fig. 6-4 shows the poloidal variations of recycling sources for different plasmas. A quantitative comparison of source distribution is estimated in Table 6.2 with the absolute number of impurities recycled in each region and its fraction (inside parenthesis in %) to the total recycling neutrals (80,000).

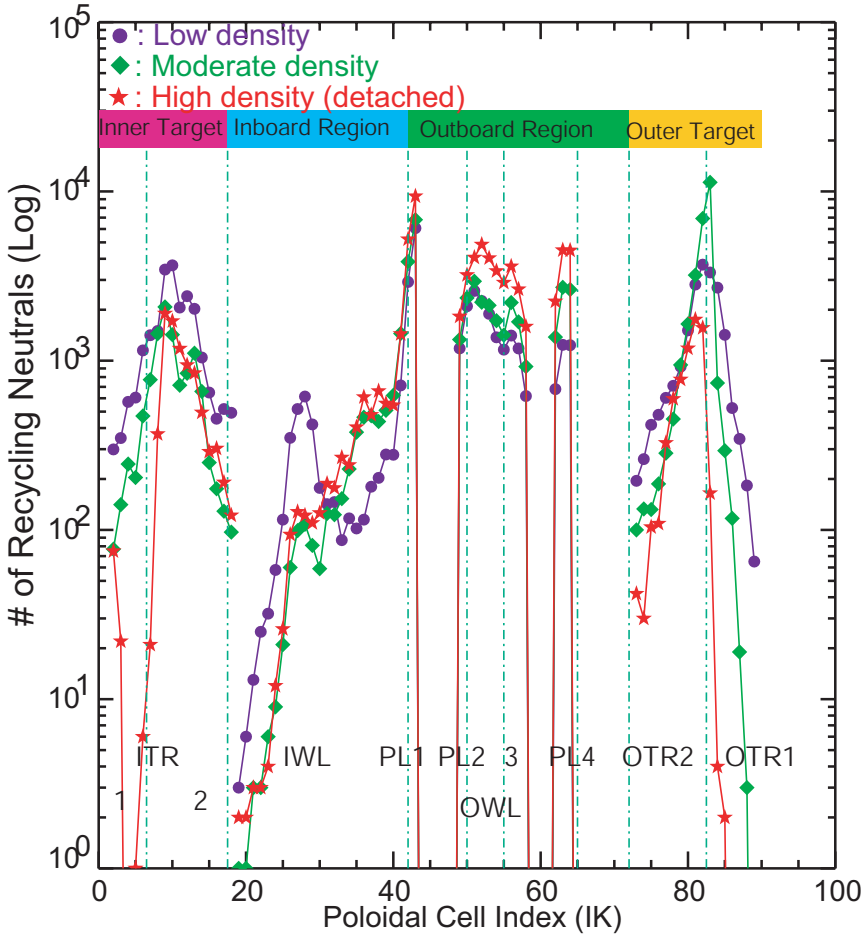

Figure 6-4: Calculation of poloidal variation of recycling source distributions around the poloidal plane. In this case, 40 impurity neutrals are injected from the outer midplane (cell 53) and 2,000 recyclings allowed. A total of 80,000 recycling impurities are distributed in various locations.

For example, the sum of all neutrals recycling at the inboard (cells 18-40) is 9,014 (low density plasma) which corresponds to 11.26 % of the total recycling neutrals (80,000). Table 6.3 implies that the inboard source fraction remains the similar level (11 $\sim$ 15 %) for different plasma cases. For the low and medium density cases,

Plasma density	Inboard	Inner+Outer Targets	Outboard
Low	9014 (11.26%)	22193+20840=42960 (53.7%)	23153 (28.9%)
Moderate	11288 (14.1%)	11343+29838=41200 (51.5%)	25958 (32.3%)
High (detached)	12005 (15%)	8587+6973=15520 (19.4%)	51466 (64.4%)

Table 6.2: The absolute number of recycling impurities at each source location and its fraction (%, in parenthesis) to the total number of recyclings (80,000).

most of the recyclings ($\geq 50\,\%$) occur on the divertor targets while the recyclings are dominant on the outboard region ($\sim 64\,\%$) for the high density case. With this source information and by utilizing the sepxing counter which keeps track of each particle, the penetration factor of each source is calculated, i.e. how many neutrals injected from each source penetrate into the core before returning to the wall and recycling again. Poloidal variation of PF of recycling model is shown in Fig. 6-5 and the regional penetration factor of each source region estimated in same way to the non-recycling case is summarized in Table 6.3. The result shows that the penetration factor (PF) of the outboard region is higher than the inboard PF, which implies that the neutrals injected from the outboard region are less screened than the inboard neutrals. This is, of course, similar to the results observed in the non-recycling impurity screening experiments.

Plasma density	Inboard	Inner/Outer Targets	Outboard
Low	1.6	1.4/0.6	7
Moderate	2.7	0.5/0.1	5.3
High (detached)	2.47	6/2.7	4.8

Table 6.3: Penetration factor (%) of each recycling source.

In addition, screening of target recycled impurities is degraded for the high density plasma case which assumes the detached condition. As another application of the sepxing counter, one can estimate the relative importance of each recycling source in determining the core impurity level which is measured by the total number of impurity ions entering the core region. For example, the low density case has a total of 2,570 impurity core penetrations. Among these core penetrating ions, 308 ions

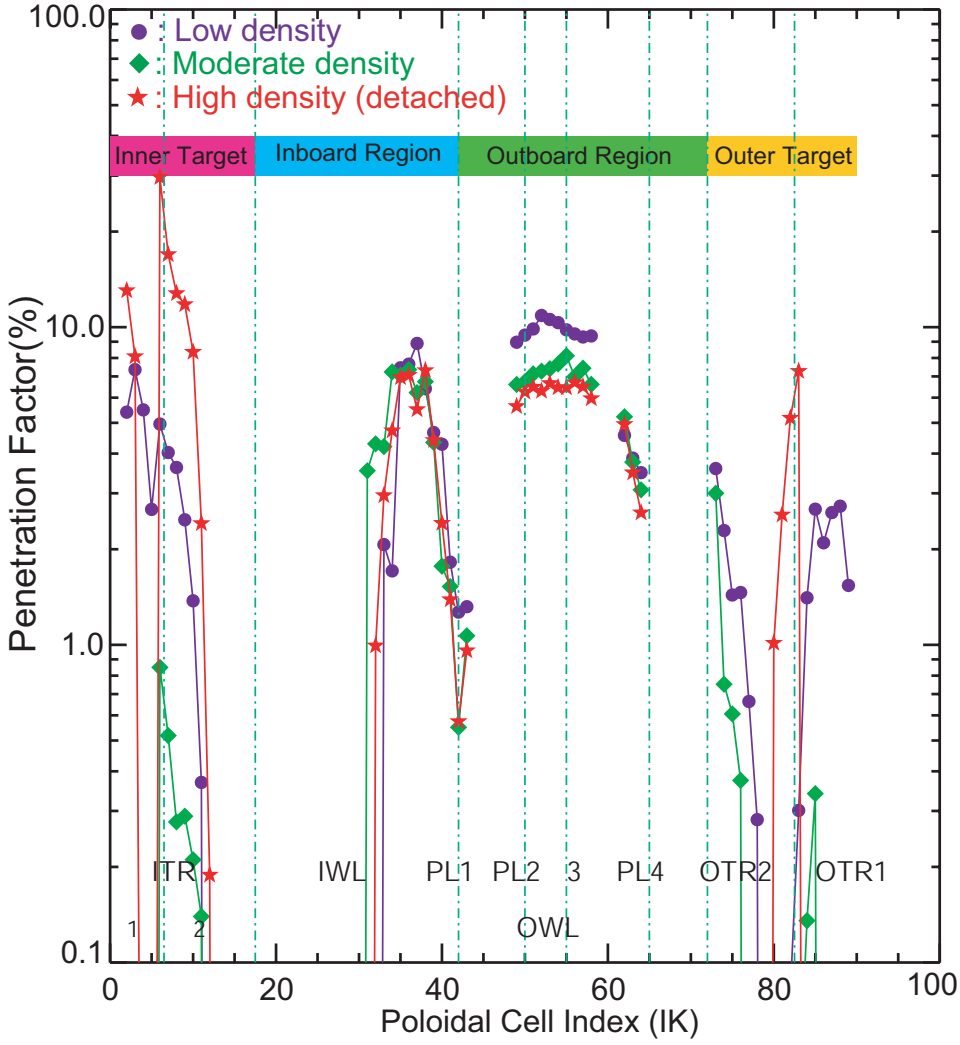

Figure 6-5: Poloidal variation of PF (%) of recycling model.

(12 % of the core penetrating ions) originated from the inboard. The number of core penetrating ions (core impurity level) and the relative importance of each source (%) is summarized in Table 6.4.

Plasma	Total # of core penetration	Inboard	Outboard	Targets
Low density	2570	12	68	20
Moderate density	1848	18	76	6
High density	3413	7	71	22

Table 6.4: The core impurity level and the relative importance in percent of each recycling source in determining the core impurity level are estimated. The core impurity level is measured by the total number of ions entering the core before they strike the walls or target surfaces.

The result shows that the outboard source dominates the core influx (more than 68%) compared for other source locations for all density cases. The inboard source contribution is consistently less than the outboard source contribution. It also indicates that for the low and high density plasmas the relative importance of target recycling sources become larger than the inboard recycling source.

6.2.3 Summary of Recycling Modeling

To summarize this section, the DIVIMP modeling has reproduced the characteristics of Ar recycling impurity compression observed in the experiment. c_z increases from low density to moderate density and then drops as the plasma detaches at high density. As in the non-recycling case, screening of recycling impurity (PF) from the inboard region is greater than those recycling at the outboard. In determining the impurity core level (estimated by the total number of ions penetrating into the core) in each plasma model, the outboard source contributes more than 68 % of the core impurities. However, the relative contribution of inboard vs. target recycling is different for different plasma densities. In the low and high density cases the core contribution ratio of the target recycling to the inboard contribution are 1.67 (= 20 %/12 %) and 3.14, respectively. For medium density the ratio drops to 0.33. Thus it can be argued that low c_z's for the low density plasmas are due to the relatively high contribution

from target recycling. For the high density case, low c_Z is due to the high PF at the target.

Chapter 7

Exploration of Underlying Physics of Impurity Retention

In the previous chapter, the results of DIVIMP modeling for impurity screening and compression measurements are presented. This chapter explores the underlying physics of impurity retention. First we will try to understand the asymmetry of screening between inboard and outboard. Second, a detailed investigation for impurity influx across the separatrix is made. Third, the sensitivity of modeling results to the plasma conditions is studied.

7.1 Asymmetry of Screening of Inboard vs. Outboard

7.1.1 Non-recycling Model

The background plasma used for the modeling of non-recycling impurity screening has comparable density and temperature values between the inboard and outboard regions, which causes the ionization depth of the recycling impurity to be similar in the inboard and outboard region. The parallel plasma flow, however, has different values between the inboard and outboard region. The background plasma typically flows from the outboard region toward the inboard region and as it approaches the

inner target the flow velocity increases up to the sound speed. The asymmetry in the plasma flow causes the frictional force on the impurity ion to be different between the inboard and outboard regions, which leads to the observed asymmetry of impurity screening of inboard vs. outboard observed both in the experiment and modeling. To quantitatively measure the sensitivity of plasma flow on the screening asymmetry, the reference plasma flows have been increased to the flow levels measured in experiment as shown in Fig. 7-1.

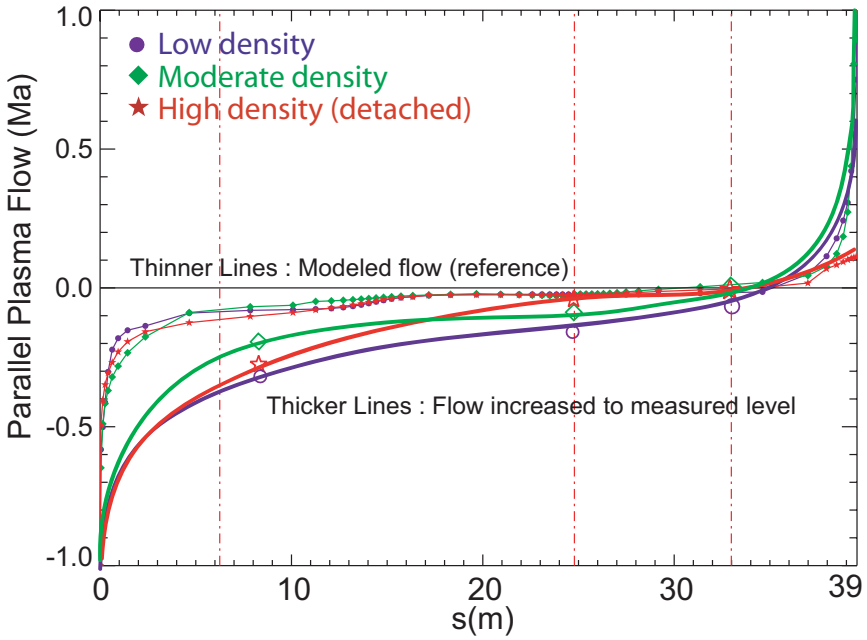

Figure 7-1: The reference flow (thinner lines) is increased to the level of measured flow (thicker lines). The experimental values of flow are shown as large hollow symbols. The effect of flow increase is expected to be more significant in the inboard region than in the outboard region.

The effect of increased flow on the PF is shown in Fig. 7-2. In general, the increase of the flow enhances the impurity screening with PF reduced. The averaged regional PF of the inboard is reduced from 3.6 % (with the reference flow) to 1.5 % (with the flow increased) and the outboard PF is reduced from 11 % to 9 %.

This result is for the non-recycling case with impurities injected at constant energy ($0.03\,eV$) around the main chamber and on the targets. In reality, however, a certain

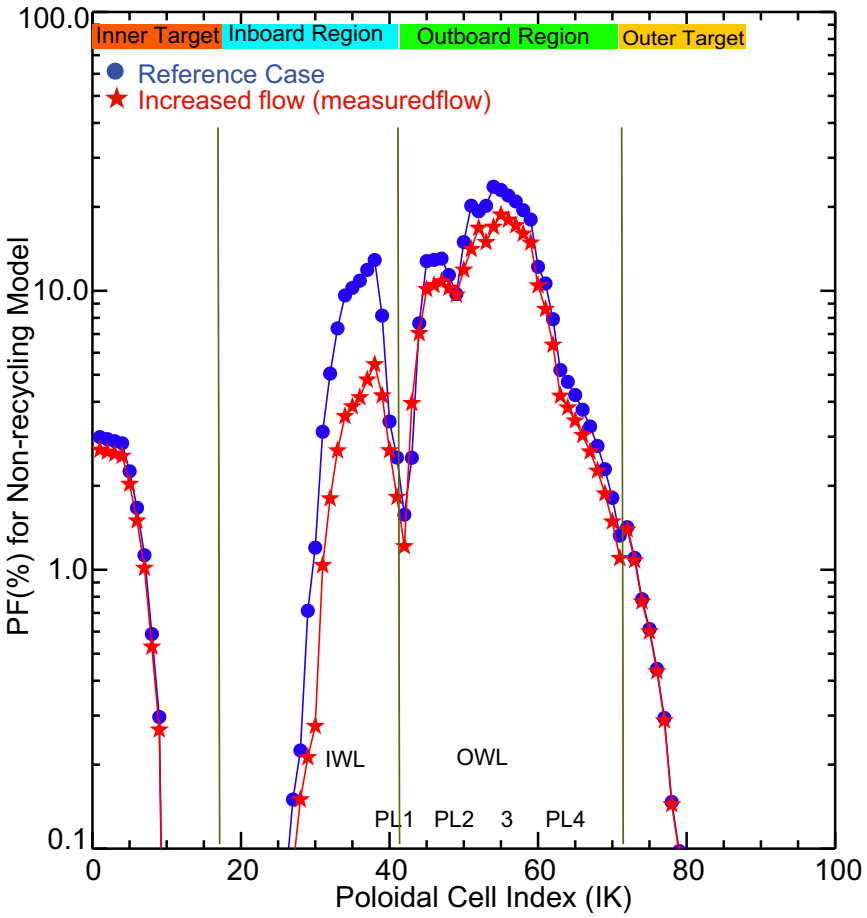

Figure 7-2: Estimation of the increased flow effect on the penetration factor. As the flow increases in the inboard region, the inboard PF is reduced by a factor of ~ 2.

portion of non-recycling impurities might be reflected off from the inner wall surfaces or the outer limiter and the emission energy might be different in the inboard and outboard regions. For example, there could be some variation in injection energy of recycled impurity caused by sheath rectification near an ICRF antenna [54]. Thus the injection energy is possibly another parameter that gives rise to the asymmetry of the screening. This is modeled by setting the inboard neutral energy to $0.03\,eV$ and the outboard to $0.5\,eV$ (this value is based as an *ad hoc* proposal, not by physical basis). The resultant averaged PF of the outboard is increased from 11 % (reference case) to 23.7 % (with the injection energy increased). With the increase of the flow and injection energy (at the outboard), the ratio of the regional PF of the inboard to the outboard becomes ~ 15 which is closer to the experimental value, ~ 20.

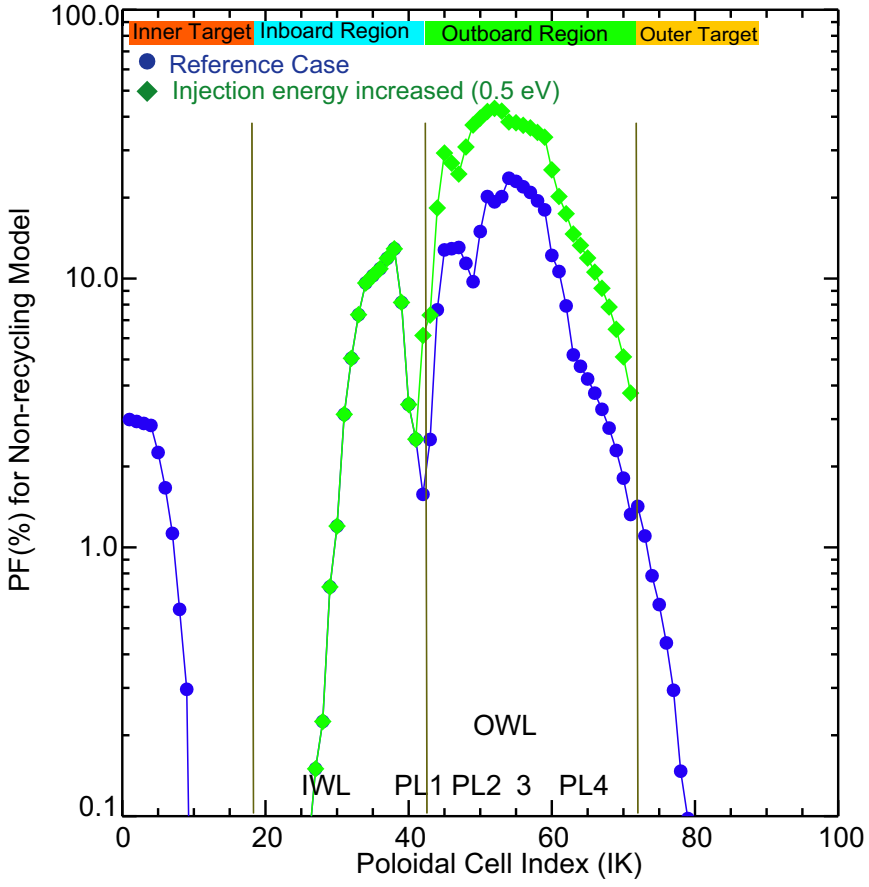

Figure 7-3: Estimation of the effect of injection energy on the screening asymmetry. Injection energy of impurity neutral in the outboard region is increased by a factor of ~ 3 ($0.03\,eV$ to $0.5\,eV$) resulting in an increase of the outboard PF by a factor of ~ 3.

7.1.2 Recycling Model

In the recycling case the asymmetry of impurity screening has been also observed in the modeling as shown in Table 6.4. It is prescribed for all plasmas used in this model that the plasmas have parallel flows directed from the outboard SOL to the inboard SOL with stronger flows in the inboard region. The asymmetry of plasma flow (thus the frictional force) causes the bulk impurity ion flows to be stronger in the inboard than in the outboard. Fig. 7-4 shows the resultant velocity profiles of bulk impurity ions in different plasmas (plotted in arbitrary units). In this figure, the parallel impurity ion flow velocities averaged over all charge states are plotted along the field line. The radial location is the first ring just outside the separatrix.

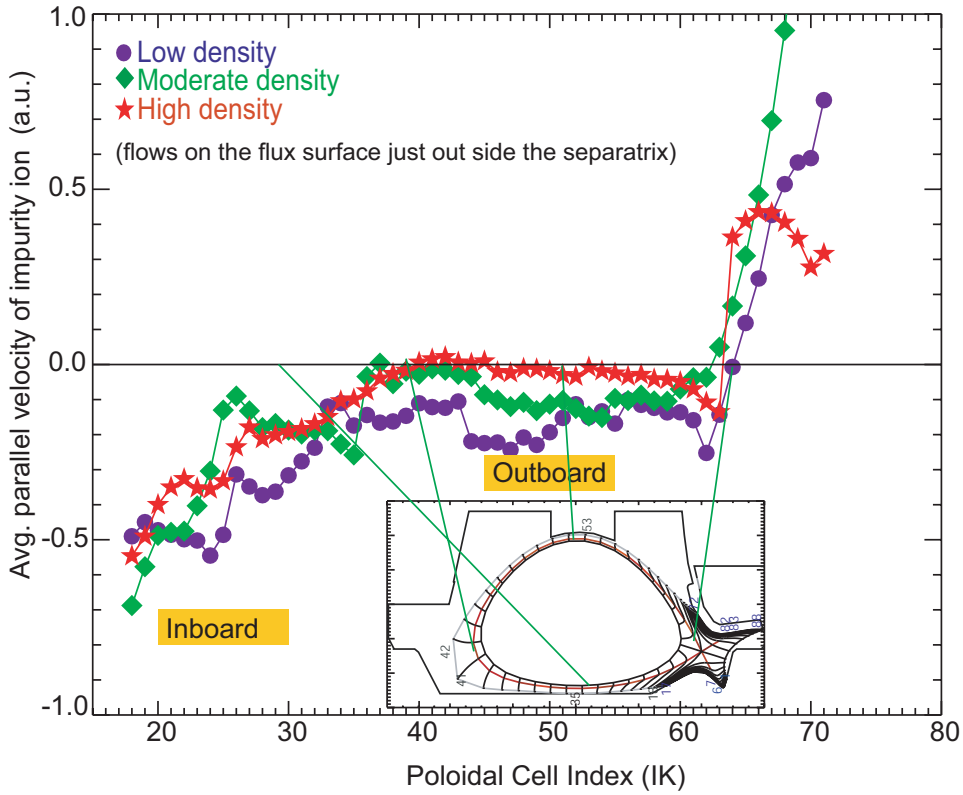

Figure 7-4: The profile of average parallel flow velocity of impurity ion just outside the separatrix. It indicates that the impurity ion flows are stronger in the inboard than in the outboard region.

The figure indicates that the impurity ion flows are weaker at the outboard region and stronger at the inboard region. Thus impurity ions in the outboard region have

sufficient time to diffuse radially inward to the core plasma or out toward the wall while those in the inboard region are expected to be swept quickly down toward the inner target before radial diffusion can take place. A factor of $\sim 2-3$ in the inboard vs.outboard flows is consistent with the difference found in the screening asymmetry. A simple test is conducted to give a quantitative estimation of the effect of SOL flow increase by imposing the experimentally measured flow [46]. The measured flow is plotted with thicker solid lines in Fig. 7-1. Quantitative effects of the increased plasma SOL flow on the screening are estimated. In the same way as in Table 6.4, the core impurity level and the relative importance of each source are calculated in Table 7.1. In addition, the recycling penetration factor, PF_R (%) defined as the ratio of the core impurity level to the total number of recycling sources (80,000) is estimated in this table. For a comparison, the values for the reference (modeled flow) case is indicated inside the parenthesis.

Case	PF_R (%)	Core impurity level	Inboard	Outboard	Targets
Low density	1.8 (3.2)	1438 (2570)	3 (12)	58 (68)	39 (20)
Medium density	1.3 (2.3)	1069 (1848)	6 (18)	70 (76)	24 (6)
High density	4.5 (4.3)	3615 (3413)	0.8 (7)	39 (71)	60 (22)

Table 7.1: Increased flow effect on the impurity screening. First column is the recycling penetration factor estimated by the ratio of the core impurity level to the total number of recycling impurities (80,0000). The core impurity level, the total number of impurity ions crossing the separatrix before striking the wall or targets, is in the second column. The relative importance of recycling source in determining the core impurity level is in the rest columns. In parenthesis are the values for the reference case.

Table 7.1 shows that increasing the flow reduces the core impurity level for the low and medium density cases and increases it for the high density case. Increasing the flows to the levels of measured values reduces the recycling PF for all but the detached case and gives values similar to experiment ($0.7 \sim 3\,\%$). For all cases the target contribution to the core impurity level increases. The smaller flow effect on the outboard screening than on the inboard screening can be explained by a couple of factors. First, as seen in Fig. 7-1, the flow increase is smaller in the outboard region than in the inboard region. Secondly, the impurity ion velocities are increased due

to the increased frictional force. The ions recycled from the outboard side have to travel a longer path until they reach the inboard region meaning that the outboard recycling ions have a good chance to diffuse into the core plasma.

The increase of target contribution to the core impurity level with the increased flows are attributed mainly to the increase of target recycling sources. The increase of recycling sources can be explained by the higher plasma flow carrying more ions to the divertor plates. For the low and medium density cases, the target sources are increased by a factor of $\sim$ 1.5. For the high density case, the target sources are increased by a factor of ~ 3.

One may argue that the increase of the plasma flow accelerates the impurity ions. Thus the energy of impurity ion striking the target should be increased sufficient to be dominant over the sheath potential energy term (in Eq. (4.4)). As a result one may anticipate that the energy of impurity neutral recycled at the target should be increased substantially due to the increased flow effect. It turned out, however, that the resultant energy of impurity neutral re-injected at the target has not changed much by the increased flow. For example, for all the cases, the energy of re-injected impurity neutral is increased from $4.6 \sim 5.4\,eV$ to $4.87 \sim 6.2\,eV$. The reduction of the core penetration from the main chamber recycling dominates over the increase of the core penetration from the target recycling for the low and medium density case while the case is reversed for the high density (detached) plasma.

7.2 Study of Impurity Influx Pattern

The screening study estimates each recycling source's contribution to the impurity core level (Table 6.5). This provides a rough estimation where the impurity ions cross the separatrix. For example, from Table 6.5 it can be inferred that more impurity ions should cross the separatix into the core from the outboard region than from the inboard region. To obtain detailed flux patterns of impurities on the separatrix the sepxing counter is used. The left panel of Fig. 7-5 shows the poloidal variation of number of ions entering the separatrix counted by the sepxing. This is the total

inward flux of impurity ions on the separatrix. The sepxing also counts the number of ions flowing out of the core through the separatrix as shown in the right panel of Fig. 7-5

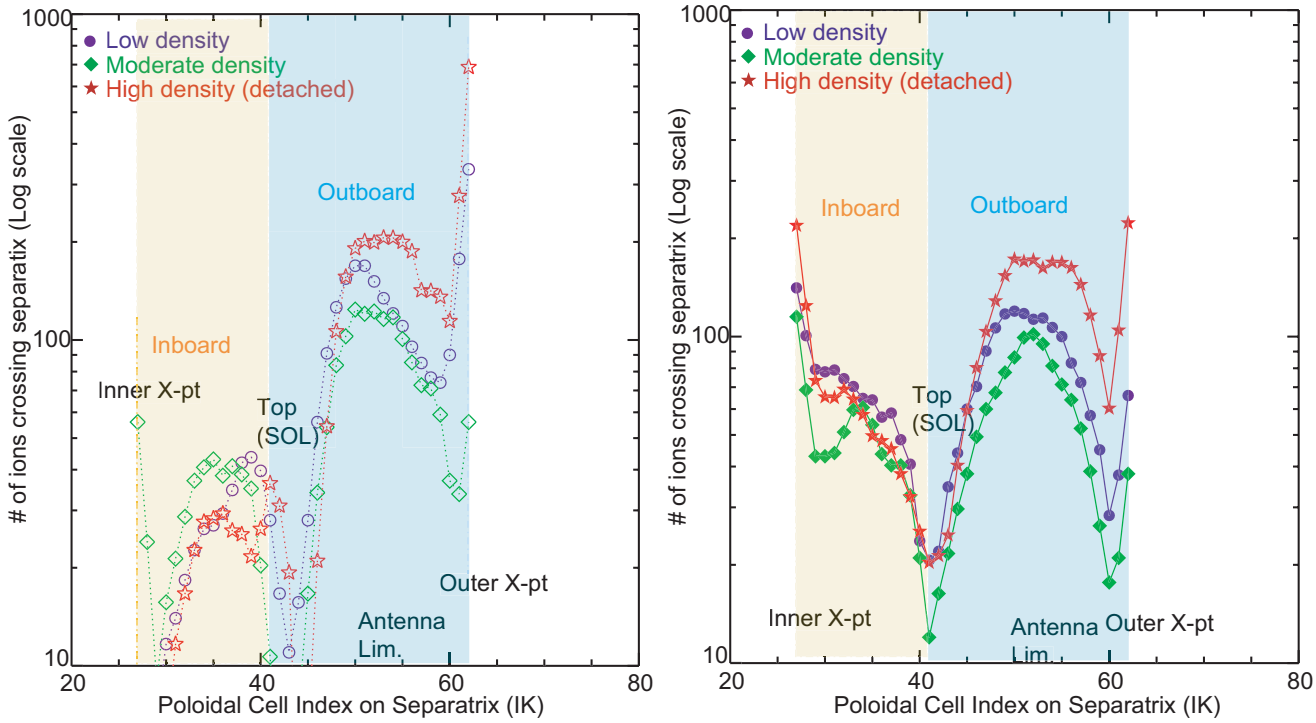

Figure 7-5: Poloidal variation of the number of impurity ions crossing the separatrix. X-axis is the poloidal cell location on the separatrix (marked with the circled number in Fig. 6-1. The left panel shows the number of impurity ions crossing the separatrix into the core and the right panel shows the number of impurity ions crossing the separatrix into the SOL.

The quantitative estimation of the pattern of the impurity ions inward fluxes across the separatrix and its dependence on density is estimated in Table 7.2. In this table, I_{INB}, I_{OBD}, and I_{XP} are the ratio of the number of ions entering the core integrated across the separatrix locations (27-41), (42-59), and (60-62) respectively, to the core impurity level (in %).

By comparison of Tables 7.1 (the relative source importance) and 7.2 it appears that impurities, for each try to cross the separatrix, generally do not travel far poloidally before entering the core. Of course, over many recyclings, they can migrate much farther poloidally. There are other implications of Table 7.2. First, the inward impurtity flux across the separatrix from the inboard side is in excess of the inboard

Case	Core impurity level	I_{INB}/C_{imp}	I_{OBD}/C_{imp}	I_{XP}/C_{imp}
Low density	2570	14	65	21
Medium density	1848	25	68.5	6.5
High density	3413	8.8	66	25.2

Table 7.2: The fraction of the impurity ions inward fluxes through the different poloidal regions along the separatrix. Inward flux through the outboard side separatrix dominates the inward flux through the inboard side. The influx near the x-point region becomes significant for the low and medium density cases.

recycling source (Table 7.1). This implies that a small fraction of the ions recycled from the outboard SOL travel to the inboard region (dragged by the background plasma flow) and then penetrate into the core from that region. Second, the influx through the x-point region is significant for the low and high density plasma cases. Details of the second observation will be discussed in the next section.

Generally, by combining the inward and outward fluxes (Fig. 7-5), it is found that the influx (hollow symbols) exceeds the outflux (solid symbols) in the outboard region while the outflux exceeds the influx in the inboard region. The summation of total influx and outflux gives the net flux of impurity ion across the separatrix and its result is shown in Fig. 7-6. The net flux pattern indicates that the impurity ions flow into the core from the outboard side (antenna limiter and the x-point regions) and flow out to the SOL at the inboard side. Note that there are substantial influxes of impurity ions to the core observed at a couple of cells near the outer x-point region (cells 60-62) for low (circle) and high (star) density plasmas. Once the ions flow into the core region (e.g. the cell COREXO in Fig.7-10) where no plasma force exists, the ions diffuse in parallel direction. Since the outboard side is the influx dominant region, the inboard side is favored for the impurity ions to flow out to the SOL. The peak of outward flux near the other x-point region (inboard side) implies that the ions penetrating into the core near the cell COREXO promptly flow out to the SOL through the cell COREXI.

From this data, the 'net influx' is calculated by summing all the negative components of the net flux. The low density case has the net influx of 794, the moderate density case of 380, and the high density case of 991.

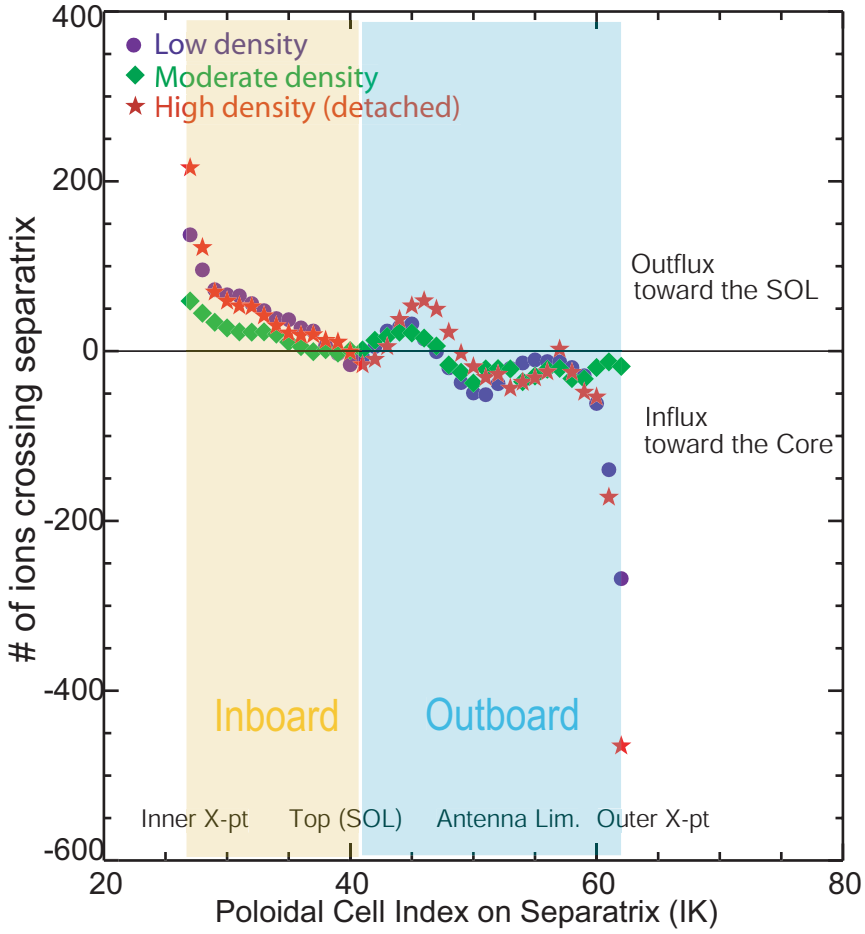

Figure 7-6: Net flux pattern of impurity ion across the separatrix for different plasmas. The result indicates that impurity ions flow into the core from the outboard side and return to the SOL at the inboard side. The low (circle) and the high (star) density plasmas have substantial core influxes from the x-point region (cells just outside the separtrix).

The above result of the significant influx near the x-point (what we call *the x-point fueling*) leads to the following questions. What causes the x-point fueling? Is it due to the target recycling ions? How is it possible for the ions recycled from the inner target to penetrate into the core from the outboard x-point? The following subsection will try to answer these questions and investigate the mechanism of x-point fueling observed in the modeling.

7.2.1 Observation of X-point Fueling

It turns out that the direction of impurity ion flow near the x-point is a critical factor for generation of x-point fueling. To demonstrate this, impurity ion flow patterns generated by facecrossing vectors are investigated near the divertor region. Figs. 7-7 and 7-8 show the ion flow patterns of the medium density case and the low density case, respectively.

For easier interpretation of these results the parallel and perpendicular components of the facecrossings are separated and the magnitude of the perpfxing on the separatrix are multiplied by a factor of 4 (represented by solid-head arrow vectors). Starting with the medium density case shown in Fig. 7-7 and looking at the cells PFXI and PFXO in the private flux zone (PFZ) the ions are observed to cross the separatrix from the PFZ to the SOL. The ions crossing the separatrix toward the inner divertor region arrive the cell XI and flow down toward the inner target implying that the plasma forces are directed to the inner target. Such a direction is attributed to the fact that the friction force (directed toward the target) dominates over the temperature gradient force (directed away from the target) in that region. The outer divertor region has a similar mechanism for impurity ion transport. The ions crossing the separatrix from the cell PFXO to the outer SOL enter the cell XO and flow down toward the outer target indicating that the friction force is dominant over the temperature gradient force in this region as well.

Now we turn our attention to the ion flow patterns for the low density plasma which is shown in Fig. 7-8. As in the moderate density case, the friction force dominates in the inner divertor region. This is shown by the parallel flow vectors heading toward

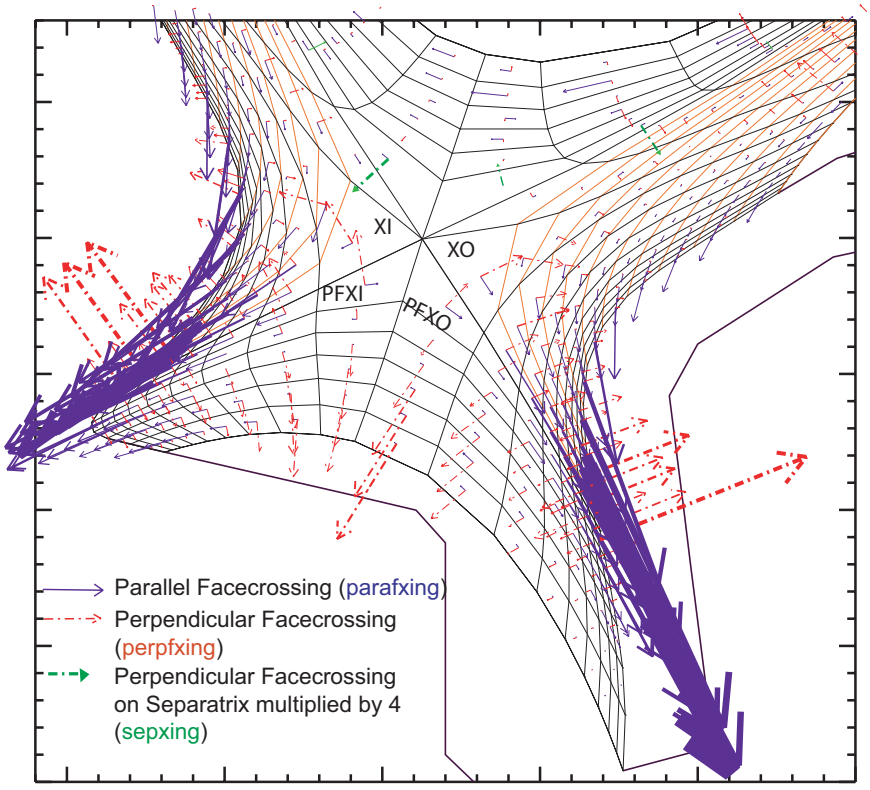

Figure 7-7: The impurity ion flow patterns near x-point indicated by the facecrossing vectors for the medium density case. Both the inner and the outer divertor region have the friction force dominant over the temperature gradient force. The resultant impurity ion flows are directed toward the targets. On the separatrix near the x-point more outflux exists than influx.

the inner target. Thus the ions crossing the separatrix from PFZ into this region will be directed to the divertor plate. The outer divertor region, however, has the opposite mechanism for impurity ion transport. Impurity ions crossing the separatrix from the cell PFXO to the cell XO are found to flow away from the outer target. This is attributed to the fact that the plasma force is directed away from the target. This direction of the plasma force results from the combination of the temperature gradient and the reverse plasma flow (away from the outer target).

One question remains to be answered regarding how inner target recycled impurities make it into the private flux and then into the core. Fig.7-10 indicates that there is a large source of impurity ions near the cells PFXI and PFXO in the private flux region (non-zero divergence). Due to the fact that the plasma density and temperature are low near the inner divertor in the private flux region, the impurities recycled at the inner divertor get ionized deeper inside the private flux region and generate the ion sources near the cells PFXI and PFXO. Of course, some of the target recycled impurities reach the bottom of the PFZ and recycle that region to be reflected into the private flux region. This amount, however, is relatively small: the contribution of the PFZ recycled impurities to the ionizations inside the private flux is less than 20 %.

For further study of this phenomenon quantitative comparisons are made in Fig. 7-9. In this figure the average parallel velocities of the impurity ions in separatrix cells near the x-point are plotted. Cell 63 corresponds to the x-point in the outboard region (cell XO) and cell 64 corresponds to the cell below XO (closer to the plate). Cell 62 corresponds to the cell above the cell XO (away from the target).

This indicates that the low density (circle) and the detached plasma (star) have parallel forces which drag the impurity ions toward the inner target. The impurity ions, therefore, have strong negative flow (directed away from the inner target) near the x-point in these plasmas. In the medium density case the plasma force causes the impurity ions to flow toward the outer target. This figure also shows that the low (circle) and high (diamond) density plasmas have the stagnation point of the impurity ion flow located below the x-point (cell 63).

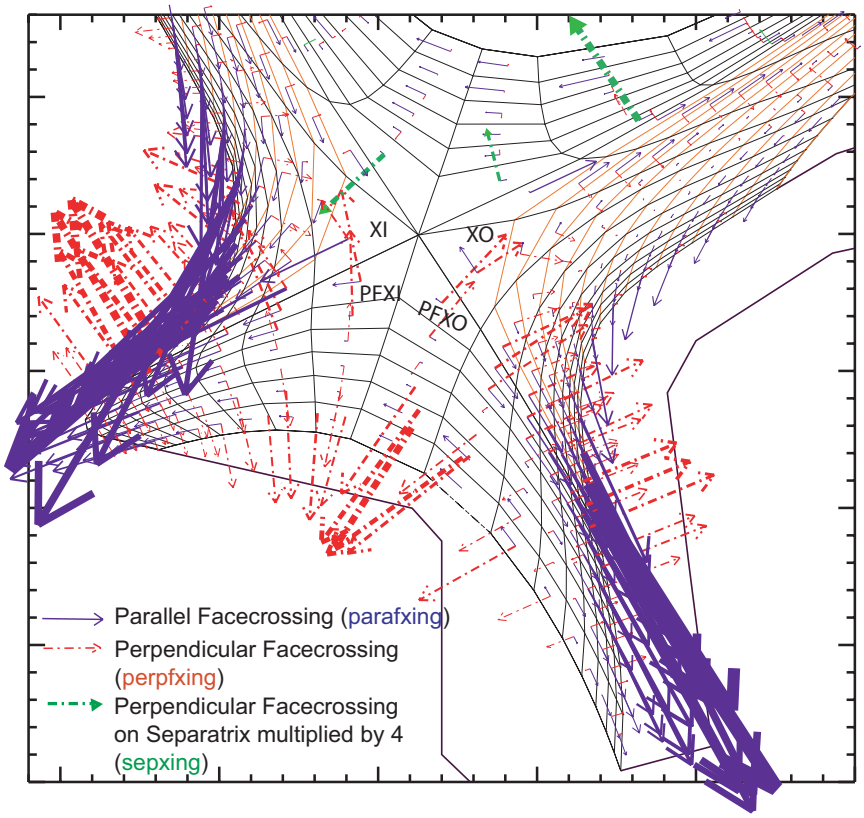

Figure 7-8: The impurity ion flow patterns near x-point for the low density case. The impurity ions flow down to the target in the inner divertor region due to the friction force. The impurity ions flow upstream in the outer divertor region. The substantial amount of influx on the separatrix near the outer x-point is attributed to the negative (toward the inner target in poloidal plane) flow effect.

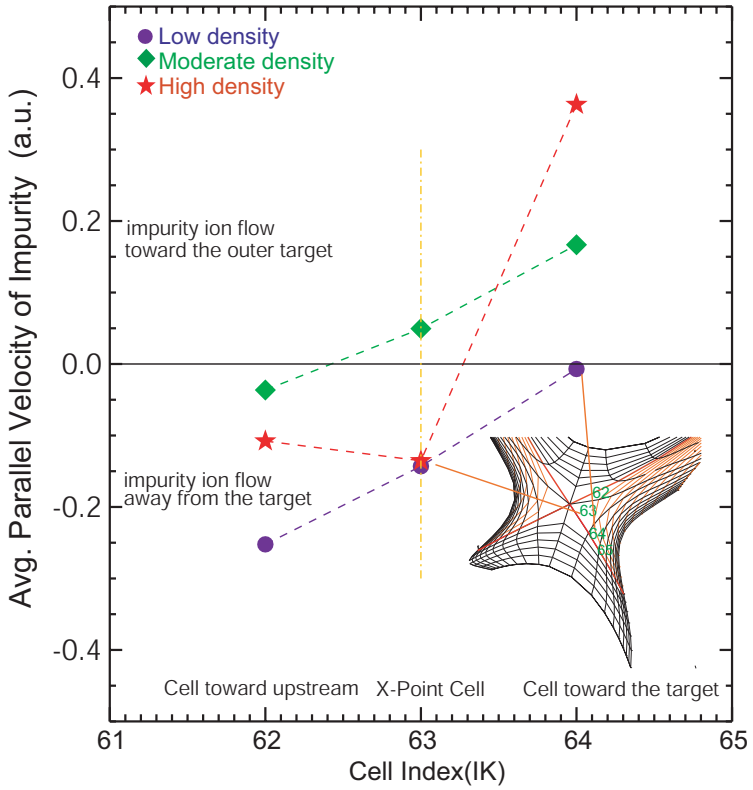

Figure 7-9: Averaged velocity of impurity ion in the first ring outside the separatrix. The low density and high density cases have impurity ions flow toward the upstream around the X-point, while the medium density case has impurity ions flow down toward the divertor target.

7.2.2 Summary of X-point Fueling Mechanism

The mechanism observed for the x-point fueling is described in a heuristic way in Fig. 7-10. The neutrals recycling on the targets and PFZ walls are ionized inside the PFZ. Among the cells in PFZ, PFXI and PFXO provide a shorter path for the impurity ions to penetrate into the core plasma. Note that the ion's direct penetration (via cross-field diffusion) from the cell PFXO to the cell COREXO is prohibited in DIVIMP, i.e. the cell XO or XI should be passed through for the ions to penetrate from the PFZ to the core. In the inboard region, for all cases, the plasma force is directed toward the inner target. Thus the impurity ions are entrained by this flow down toward the inner target and have a very small chance to reach the core.

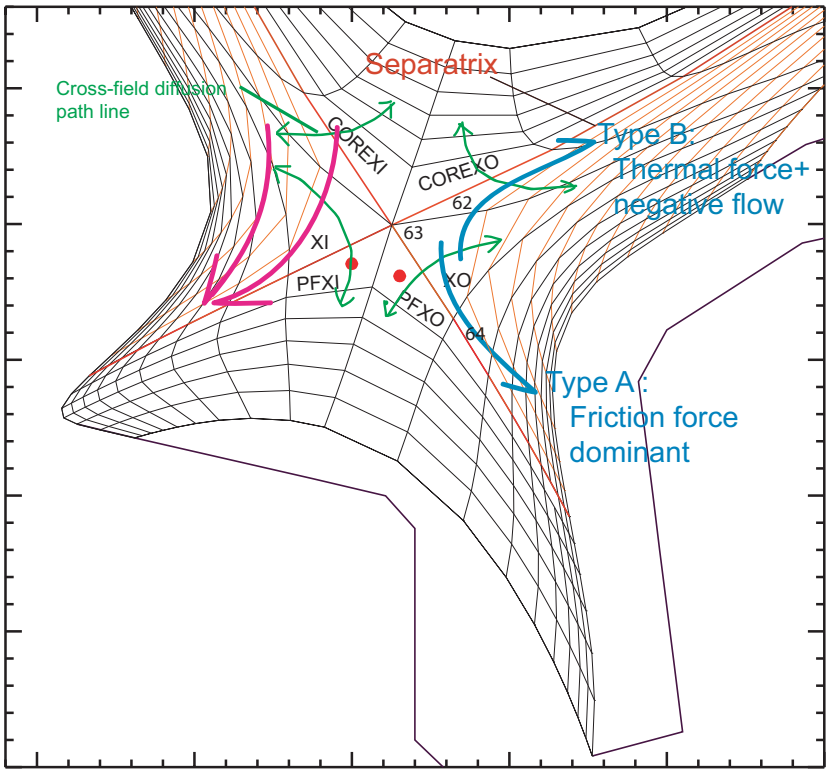

Figure 7-10: Illustration of the mechanism of the x-point fueling. The x-point fueling occurs when the impurity ion flows away from the target due to the background plasma force (Type B).

Ions diffusing out from the cell PFXO to the cell XO can diffuse into the core depending on the direction of the plasma force in that cell. Two types of total forces

exist in the cell XO, one is directed down toward the outer target (type A) and the other is directed away from the outer target (type B). The type B force observed in the low and high density plasmas favors ion core penetration in x-point region while type A (observed in the moderate density plasma) force favors ion retention in the divertor region. Also note that the low density and the high density plasmas have the impurity ion flow's stagnation point below the x-point while the moderate plasma has the stagnation point above the x-point.

This evidence suggests that the impurity influx near the x-point is sensitive to changes in the direction of the impurity ion flow and the subsequent change in the location of the stagnation point of impurity ion flow.

7.3 Effect of the SOL Flow Change on the Impurity Ion Influx on the Separatrix

In the study of recycling model sensitivity to plasma conditions the impurity ion influx was observed to be affected mainly by the parallel plasma flow in the SOL rather than by the plasma conditions in the private flux zone (Ch.5). This section will investigate the effect of the SOL flow change on the impurity ion influx across the separtrix.

First the change in the influx is investigated as the SOL plasma flow is increased. Fig. 7-11 shows the influx for the reference flow (top panel) and the influx for the case with the measured flow imposed (bottom panel).

The figure indicates that increasing the SOL flow reduces the influx from the outer midplane. The x-point fueling, however, still exists with the flow increased. Note that increasing the modeled flow to the levels of measured flow values has not changed the location of the the impurity flow stagnation point. In other words the impurity ion flow pattern near the x-point is unchanged. An increase in x-point fueling is observed in the high density plasma (star). This can be explained by the strong flow carrying a substantial amount of ions to the inner divertor plate which has a high penetration

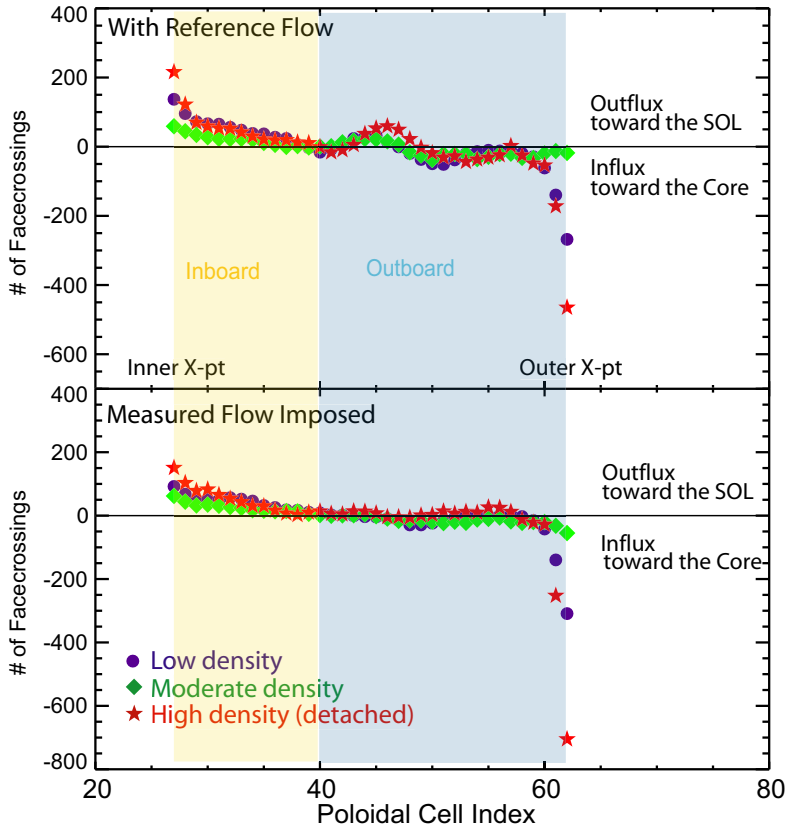

Figure 7-11: Increased plasma flow (to the levels of measured values) reduces the ion influx into the core from the outer midplane. The x-point fueling still remains with the flow increased.

factor. A quantitative estimation of the increased flow effect is estimated in Fig. 7-12

The top panel shows the changes in the 'net influx' estimated by summing the negative components of the net flux (section 7.2). The middle panel shows the change in the fraction contributed by the outer midplane influx (total of influx over cells 49-61) to the 'net influx', and the bottom panel shows the change in the fraction contributed by the influx near the x-point (total of influx over cells 62-63) to the 'net influx'. The results indicate that the reduction factors for the net influx due to the flow increase are 0.75, 0.95, and 0.85 for the low, medium, and high density cases. The reduction factors for the outer midplane influx are 0.57, 0.7, and 0.3 for the corresponding plasma cases. The fraction of the x-point fueling to the 'net influx' has increased by a factor of ~ 1.5 as the plasma flow increases.

The previous section showed that the x-point fueling is sensitive to the direction of impurity ion flow near the x-point. We present several case studies to show that the x-point fueling is strongly correlated with the location of impurity flow stagnation point (typically x-point fueling has occurred when the stagnation point was located below the cell XO). In the first test the SOL plasma flow direction is reversed so that the parallel plasma flow now travels from the inboard region toward the outer target and results in the impurity ion stagnation point located on the inboard x-point. A conceptual picture of the reversed flow model is shown in Fig. 7-13.

To check the dependency of the influx on initial injection location, the impurity neutrals are injected both at the outer midplane (case a) and at the inner midplane (case b). In case a, the impurity neutral is injected at the strong plasma flow side. In case b, the impurity neutral is injected at the weak plasma flow side. The results are shown in Fig. 7-14. To comply with the sign convention used in flow calculation (Ch.5), the plasma parallel flow directed from the outboard toward the inboard will be called *negative flow* while the flow directed toward the outer target will be called *positive flow*.

With the flow reversed (circle for case 'a' and star for case 'b') to opposite of the reference case (diamond), the impurity ion influx pattern is inverted about the top of the SOL (cell 40). The location of the x-point fueling moves from the outboard to

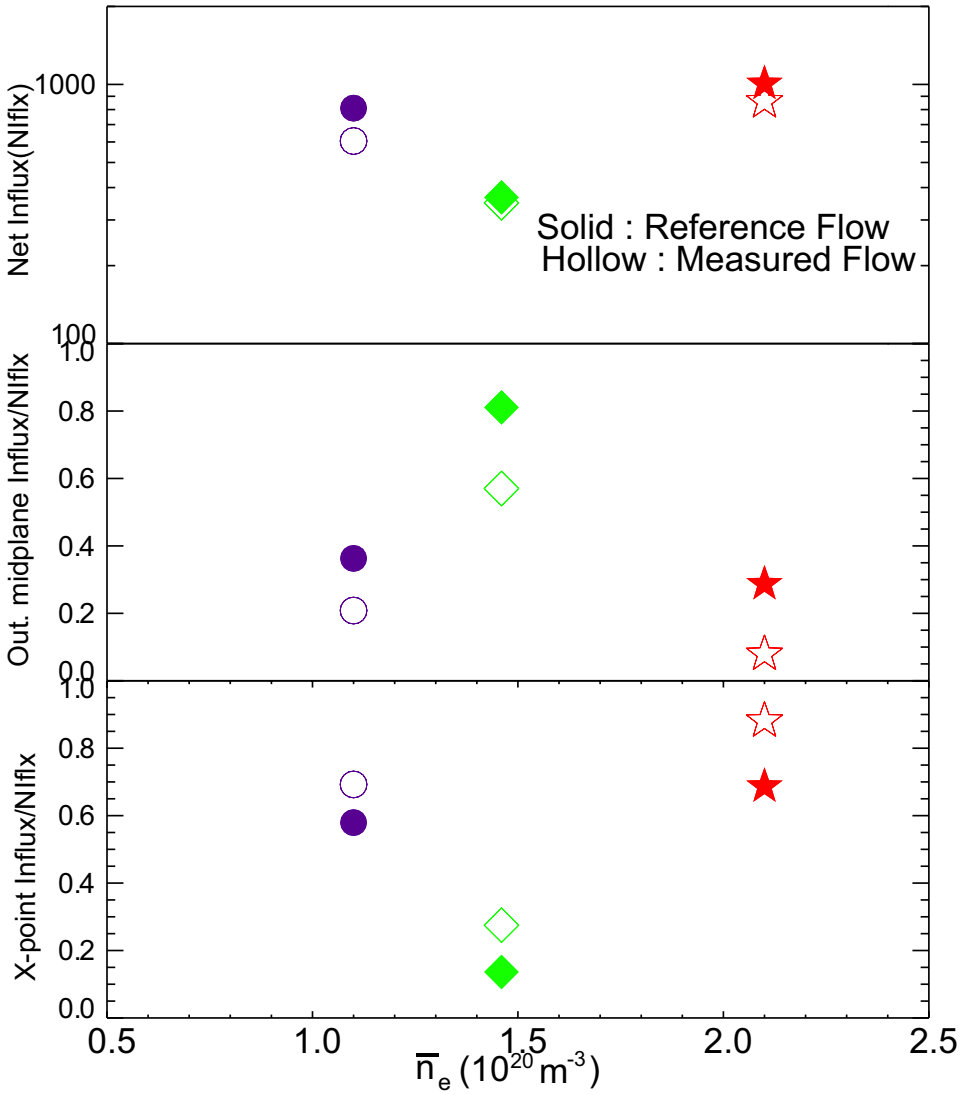

Figure 7-12: Quantitative estimation of the increased flow effect are made for different plasmas. Top panel shows the effect on the total net influx, middle panel shows the effect on the fraction of outer midplane influx, and bottom panel shows effect on the fraction of x-point influx

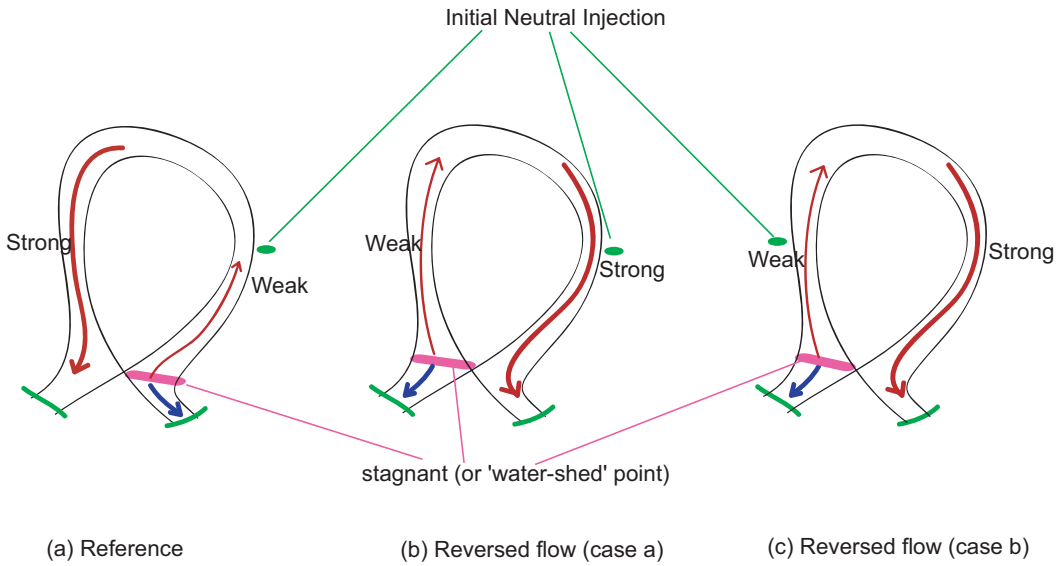

Figure 7-13: Conceptual cartoon of reversed flow model. The reference case has the impurity flow stagnation point on the outboard x-point with plasma flow directed from that point toward the inboard region. The reversed flow model has relocated the stagnation point to the inboard x-point with plasma flow directed from the inboard region toward the outer target.

the inboard side, and the ion outflux location shifts from the inboard region to the outboard region. Both cases share similar features and are summarized as follows: the x-point fueling occurs when the impurity flow stagnation point is located below the x-point (i.e. the impurity ion flow direction is away from the target on the x-point), the secondary influx is also observed typically in the region where the negative/positive plasma flow is relatively weak (i.e. the outer midplane for the reference and the inboard midplane for the test case), and the outflux to the SOL is present in the region where the plasma flow becomes stronger, and it is found that the compression ratios of three cases are comparable ($c_z = 27 \sim 29$).

The third case study is performed to show the importance of the direction of the impurity ion flow near the outer x-point in creating x-point fueling. For the study, the plasma flow condition is artifically altered so that we can have three different 'hybrid' models. The resultant changes made in impurity ion flows are plotted in Fig. 7-15. They are:

1. 'hybrid a' : Plasma flow of the low density case (which has the flow reversal

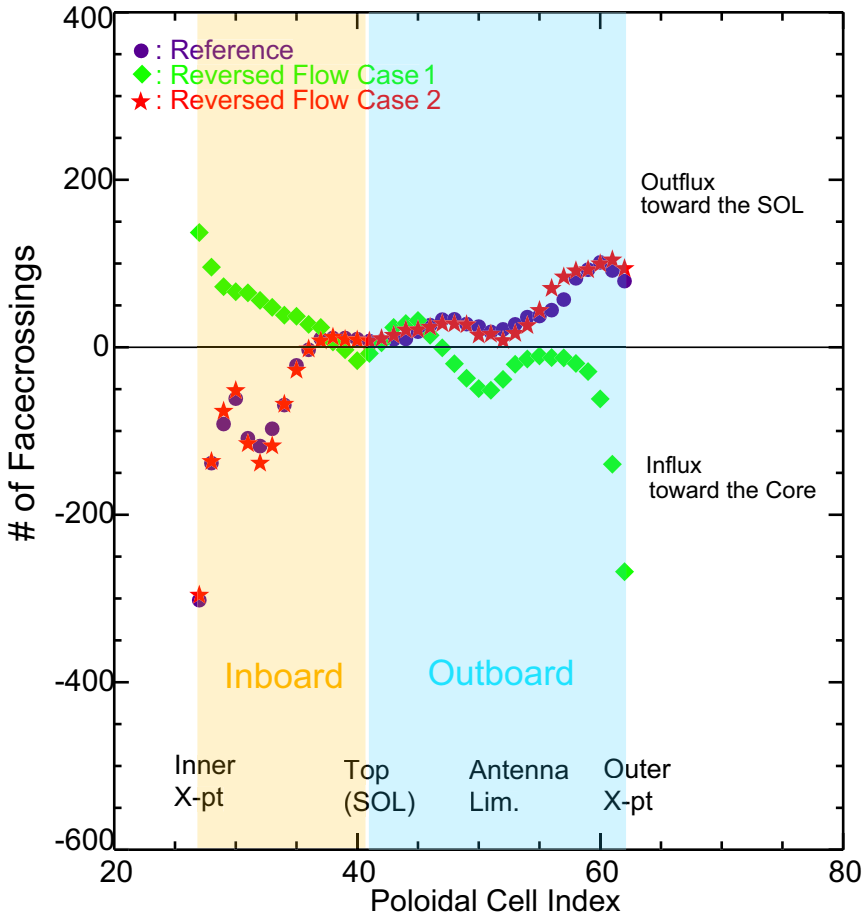

Figure 7-14: Result of the reversed flow model. With the flow reversed (circle for case a and star for case b) in the opposite to the reference case (diamond), the impurity ion influx is reversed about the top of the SOL (cell 40): the x-point fueling is shifted from the outboard to the inboard and the ion outflux is also shifted from the inboard region to the outboard region.

on the x-point) is substituted for the medium density case flow. Thus the direction of the frictional force ($\frac{v_p - v_z}{\tau_{||}}$) has changed so that the impurity ion flow direction changes at the x-point from 'toward the target' to 'away from the target'.

2. 'hybrid b' : Plasma flow of the medium density case (which has the flow directed toward the outer target on the x-point) is substituted for the low density case flow. As a result, magnitude of the negative plasma flow of the low density case is reduced at the x-point so that the impurity ion flow direction remains the same but its magnitude is reduced by about 30 % .

3. 'hybrid c' : Plasma flow of the medium density case is substituted for the high density case flow. The resultant frictional force now becomes dominant over the temperature gradient force. Thus the impurity ion flow direction changes at the x-point from 'away from the target' to 'toward the target'.

Fig. 7-16 shows how the impurity ion influx changes for the 'hybrid a' model. X-point fueling is obtained when the impurity ion flow direction changes to 'away from the target' at the x-point in the hybrid model.

The change in the impurity flux for 'hybrid b' model is shown in Fig. 7-17. This hybrid model changes only the magnitude of the impurity ion flow velocity at the x-point by about 30 %. The x-point fueling is still present for the 'hybrid b' case. Only the magnitude of the inward flux near the x-point is changed: the number of facecrossings over the cells 61-63 for the hybrid case is reduced to about of the corresponding value of the reference case. The most dramatic changes are observed for 'hybrid c' model. Fig. 7-18 shows the result of 'hybrid c' model. With the impurity ion flow directed toward the outer target, x-point fueling is reduced significantly.

The compression ratios for the hybrid models compared to the reference cases are shown in Fig. 7-19. 'Hybrid a' case reduces the compression ratio as the x-point fueling increases. c_z for 'hybrid c' case increases due to the substantial reduction of impurity influx near the x-point. The change of the magnitude of the impurity ion flow does not affect the compression ratio for 'hybrid b' case.

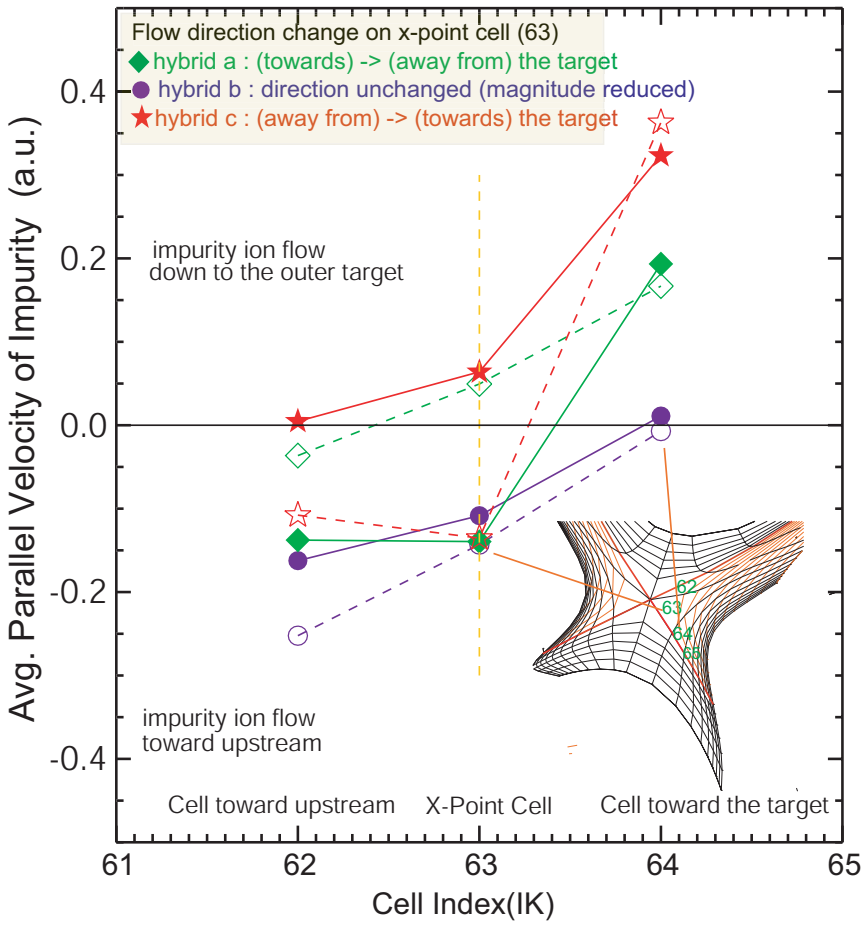

Figure 7-15: The hybrid plasma model changes the impurity ion flow in the outer x-point region. The hollow symbols are for the reference cases which are the same as in Fig. 7-9 and the filled symbols are for the hybrid cases.

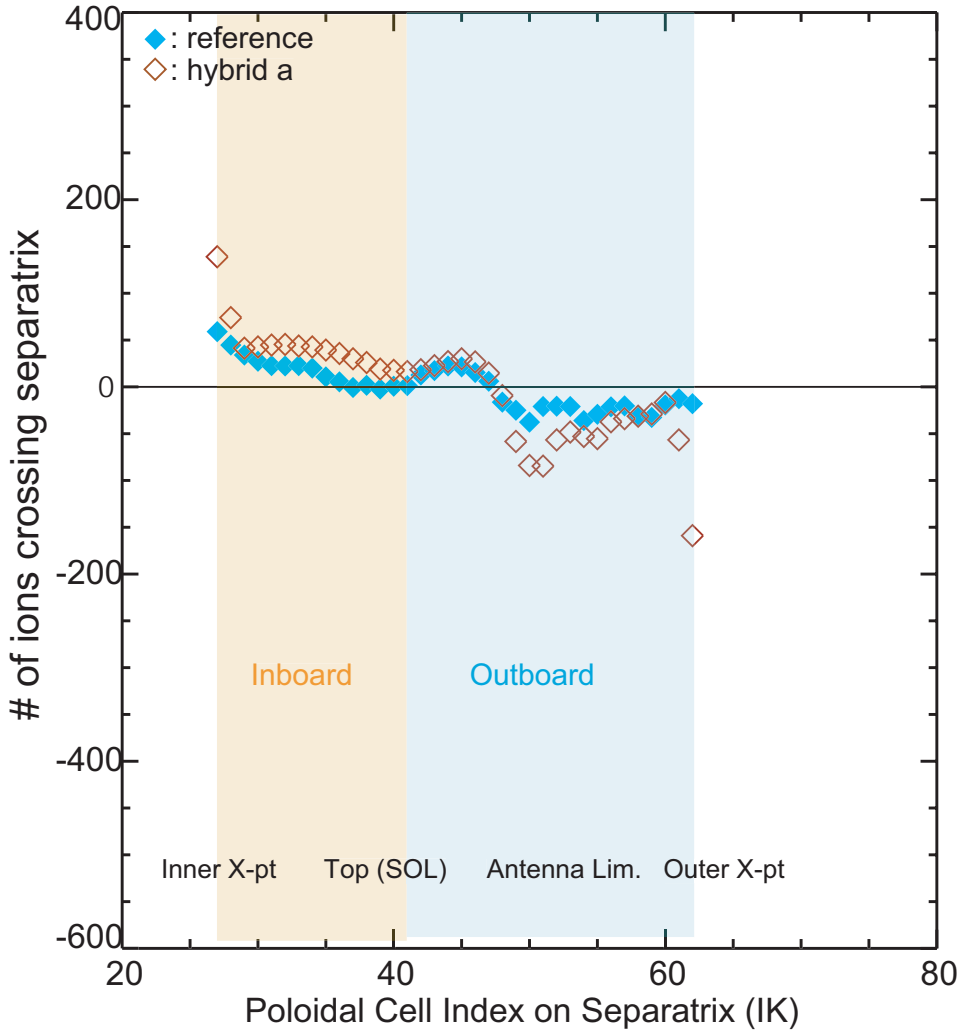

Figure 7-16: The impurity ion flux change for 'hybrid a' model. The hybrid case (the negative impurity ion flow on the x-point cell) adds a strong influx on the x-point cell and increases the influx from the outer midplane.

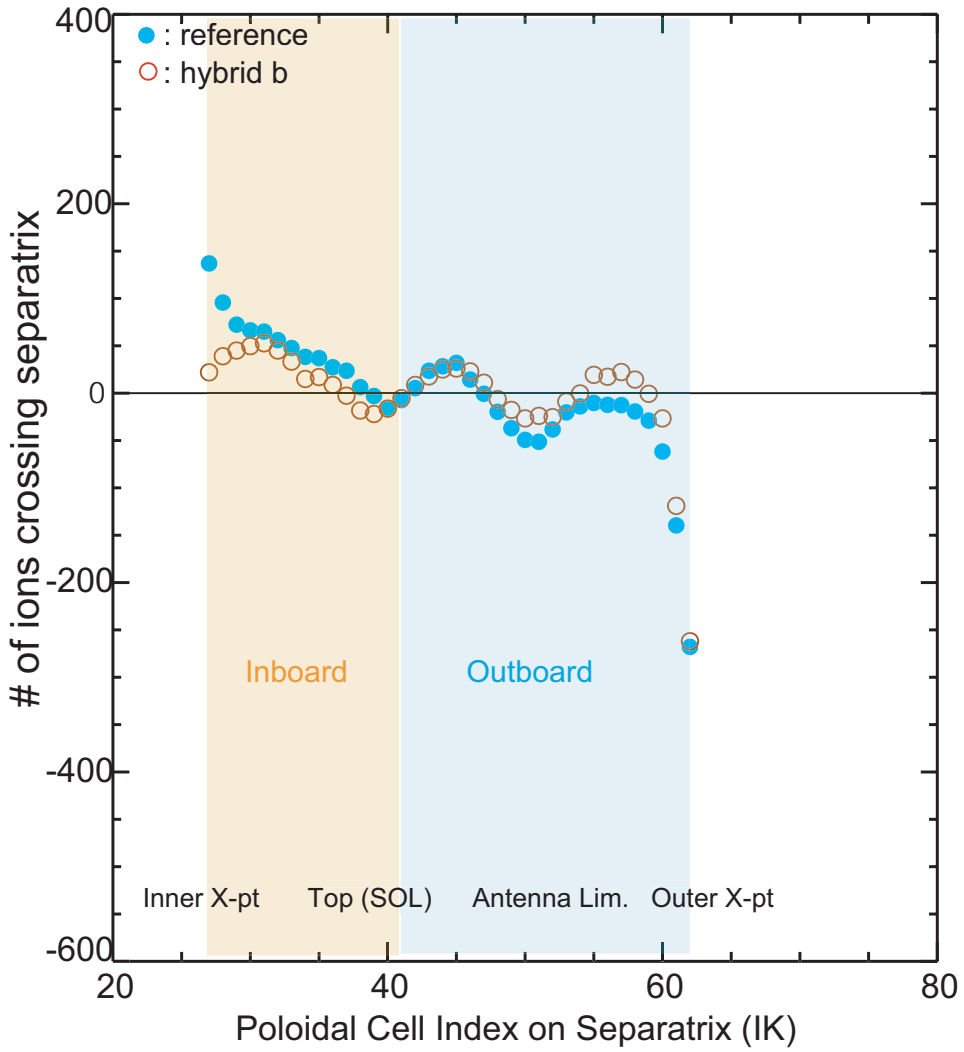

Figure 7-17: The impurity ion flux change for 'hybrid b' model. The hybrid case changes only the magnitude of the inward flux of the impurity ion. Typically, near the x-point (cells 61-63), the number of the facecrossings for the hybrid case is reduced to about 85 % of the corresponding value of the reference case.

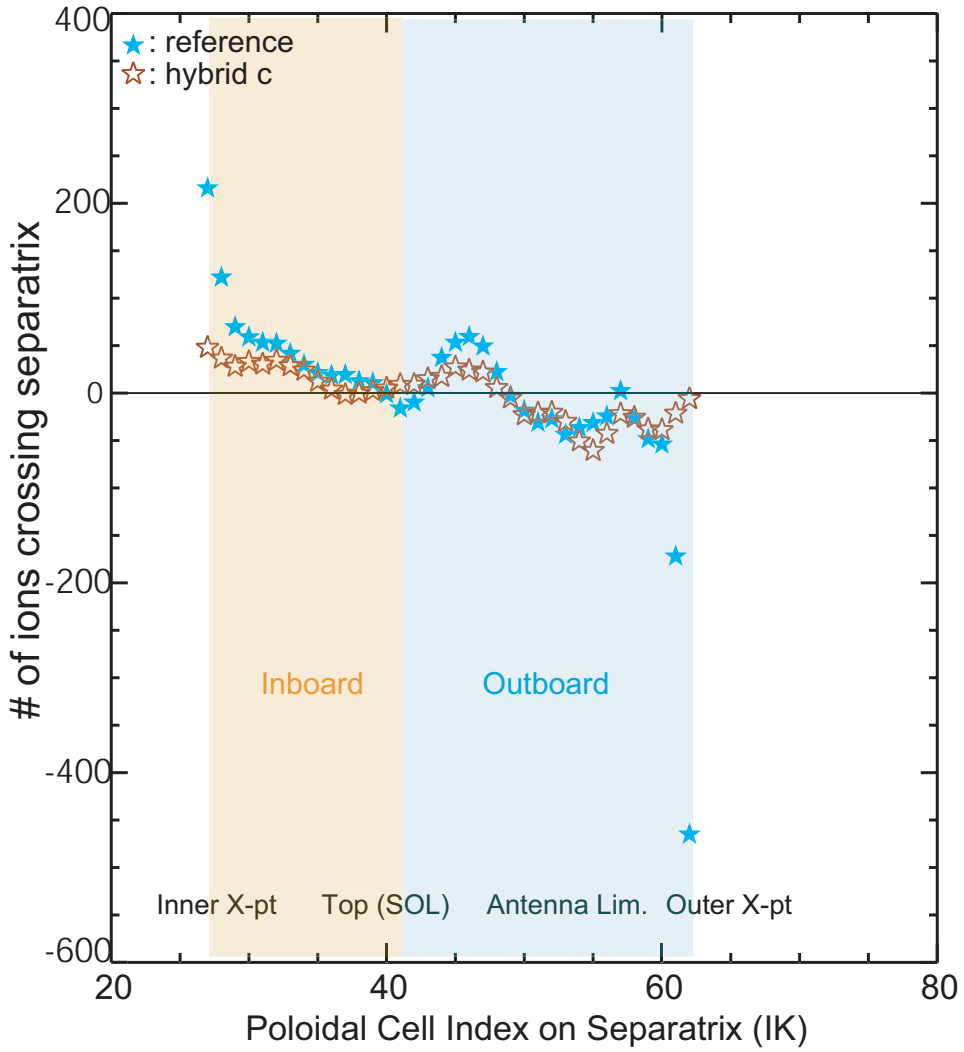

Figure 7-18: The impurity ion flux change for 'hybrid c' model. The reference plasma is the high density (detached) plasma. X-point fueling is reduced significantly with the impurity ion flow directed toward the outer target.

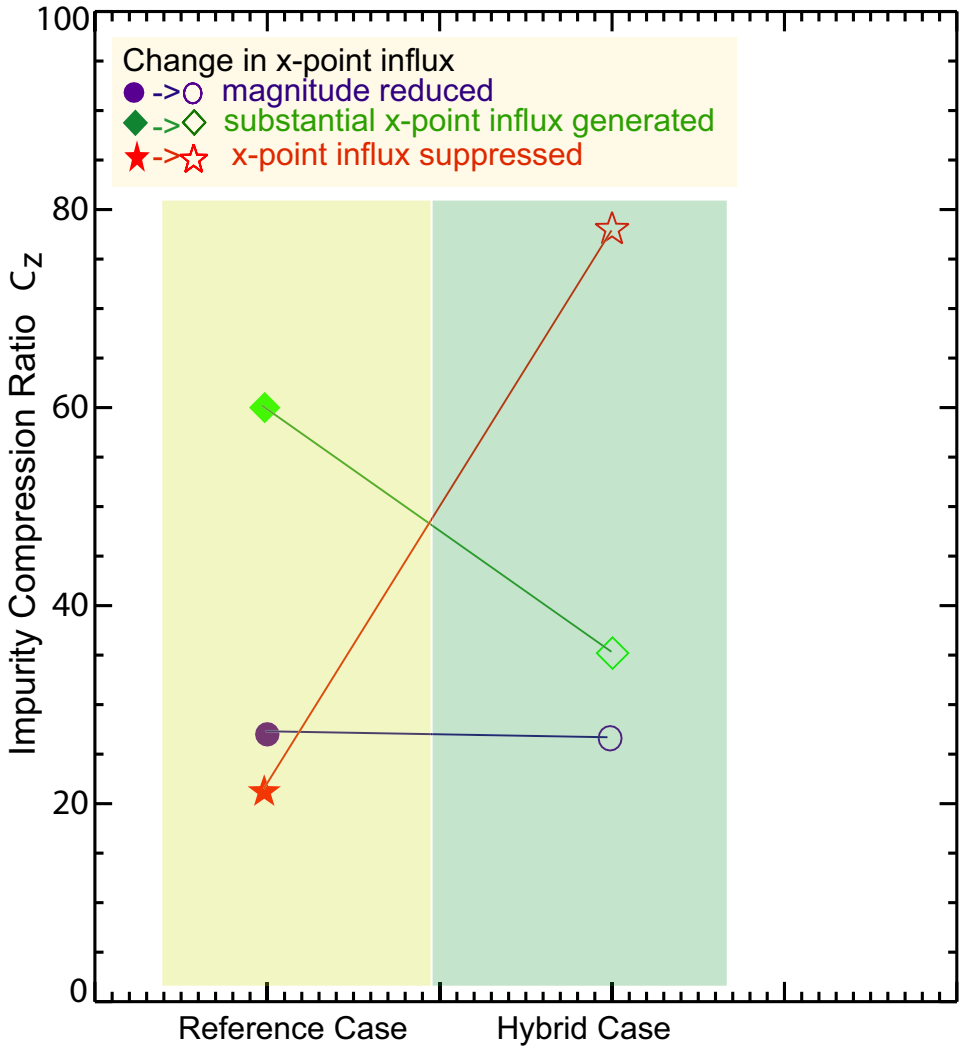

Figure 7-19: The impurity compression ratios between the reference case and the hybrid model. The increase of x-point fueling in 'hybrid a' model reduces the compression ratio and the decrease of x-point fueling in 'hybrid c' model increases the impurity compression.

7.3.1 Summary of Flow Effect on the X-point Fueling

The strong influx of impurity ions near the x-point, that is called the x-point fueling, is observed in the low and high density cases while the medium density case has no x-point fueling. It is found that the x-point fueling cases have impurity ion flows directed away from the target (*negative ion flow*) near the x-point cell while the non-fueling case has the impurity ion flows directed toward the target near the x-point.

Thus the direction of the impurity ion flow (resulting from the background plasma force) on the x-point cell is shown to be a critical factor for x-point fueling generation.

Chapter 8

Summary and Future Work

This chapter will summarize the work done in this thesis: modeling the background plasma, DIVIMP code updates, and reproduction of experimental observations of impurity screening using DIVIMP modeling. Suggestions are given for future work to improve the background plasma description and the radial transport model in DIVIMP.

8.1 Background Plasma Modeling

The background plasma is prescribed on the grid as an input to the DIVIMP code. For the description of the SOL plasma, a simple 1D solver has been developed. This solver solves the parallel heat conduction equation for the plasma temperature and the continuity and momentum equations coupled with EIRENE neutral code to calculate the plasma density and flow velocity. The boundary conditions are given on the targets by probe measurements. The calculated temperatures have good agreement with the ASP probe data at the midplane within 3 % error. The parallel plasma flow, however, has been found to be smaller than the measured flows by a factor of $2 \sim 3$. The impurity screening was found to be affected by the change in the SOL flow (by a factor of 2). Additional sensitivity modeling of the private flux region was also performed. This study indicated that the impurity penetration to the core is sensitive to the plasma density (e.g. the increase of the plasma density by a factor

of 2 in the private flux region reduced the number of facecrossings near the x-point by $\leq 25\,\%$). Changing the density by a factor of 2, however, is well within the experimental uncertainties. The change in the plasma flow in the private flux region resulted in a change in the x-point influx by only $\sim 10\,\%$ from Fig. 5-13.

It is clear that improvements in the background plasma model are needed. Nevertheless the model has been, and was used to generally match the experimental measurements for recycling and non-recycling PF, to characterize the impurity flow pattern, and to determine the important factors governing impurity penetration and flow.

8.2 DIVIMP Code Updates

The DIVIMP code was used to study impurity retention. The code has been modified with the implementation of a new physics description and new diagnostics. First, the *facecrossing* method replaced the conventional flux measurements of the code. This alternate flux measurement counts the number of ions crossing the cell boundary both in the direction of the parallel and perpendicular to the field line. The perpendicular component of the *facecrossing* on the separatrix, called the sepxing, is used to describe the pattern of the impurity ion flux across the separatrix. The *facecrossing* method always results in particle balance while the conventional method, flux measured by nv or $D\nabla n$, does not guarantee particle balance.

Second, the recycling of impurity ions in the main chamber and on the divertor plates has been updated. In the main chamber region both the parallel and perpendicular diffusion is allowed to transport impurity ions outside the plasma grid. Perpendicular diffusion is the main mechanism of impurity ion recycling in the inboard region while parallel diffusion is assumed to be the principal mechansim of outboard recycling. An approximate model combining TRIM and Eckstein models [40] is implemented for the calculation of the particle and energy reflection coefficients on targets.

Third, diagnostics for identifying the connections between the recycling sources and the impurity core level are implemented for the calculation of impurity penetration

factors.

8.3 Modeling Results

DIVIMP modeling has reproduced the characteristics of impurity screening observed in the experiments; the asymmetry of screening from inboard to outboard and density dependence of the recycling impurity compression ratio.

8.3.1 Asymmetry of Impurity Screening

In both experiment and modeling an asymmetry of impurity screening of inboard vs. outboard has been found. Typically the screening of impurities launched from the inboard is found to be better than from the outboard by a factor of 3 in the non-recycling model. This factor of 3 is lower than the factor of 20 obtained in the experiments with non-recycling gas. Such a difference can be reduced if increased plasma flow in the inboard region and increased injection energy of impurity neutral in the outboard are taken into account. Our modeling prescribes the same impurity diffusion coefficient, $D_\perp$, at the inboard and outboard. The discrepancy in screening factor inboard/outboard ratio might be further reduced by allowing higher $D_\perp$ at the outboard, as would be consistent with the experimentally indicated deuterium diffusivity.

It is commonly observed for different plasma cases of recycling models that the plasma flows from the outboard to the inboard and, as it approaches the inboard SOL, the flow becomes stronger than in the outboard by a factor of 3. As a result, the impurity penetration factor of inboard impurities is lower than the outboard penetration factor by a factor of 5 or more for the recycling case.

Increasing the modeled plasma flow in the SOL to the levels of measured values gives rise to a recycling PF similar to that seen in experiment ($0.3 - 7\,\%$).

8.3.2 Impurity Ion Influx

The impurity ion influx pattern on the separatrix has also been investigated. In general the impurity ions flow into the core from the outboard region and then flow out to the SOL through the inboard separatrix. A substantial influx of impurity ions near the outboard side x-point (x-point fueling) is observed in the low density and high density plasmas while the medium density case has no x-point fueling. The x-point fueling cases have the impurity ion flows directed away from the target (*negative ion flow*) in the near x-point cells while the non-fueling case has the impurity ion flow directed toward the target near the x-point. A sensitivity study of the x-point fueling has shown that the x-point fueling location shifts accordingly as the impurity ion flow direction is changed near the x-point.

8.4 Future Work

As the senstivity study indicates, it is important to have precise description of background plasma, primarily for the SOL flow. The description of the background plasma would be improved by using a 2D fluid code. Especially the improvements of plasma modeling for detached cases are needed to better study the impurity screening and penetration.

Modeling could be extended to study of radial transport effects on impurity retention. For example it is expected that the effect of $E \times B$ drift of plasma and the role of convective radial flux at the outer midplane could be important parameters to determine the impurity influx on the separatrix.

Appendix A

Monte-Carlo Descriptions for Atomic Processes

A.1 Ionization and Recombination of Ion

The Monte-Carlo method determines if an ion becomes ionized or recombined as follows:

1. Draw a random number, ξ, unformly ditributed in [0,1]
2. The state of impurity ion will change when $\xi <$ kpchs
3. If kprcs $\leq \xi <$ kpchs, then the ionization occurs
4. If $\xi <$ kprcs , then the recombination occurs

, where[1]

$$\begin{aligned} kpchs &\equiv 1 - e^{-\delta ttauch} \\ tauch &\equiv \frac{1}{kfizs} + \frac{1}{kfrcs} \\ &= n_e(< \sigma v >_{iz} + < \sigma v >_{rec}) \\ taurec &\equiv \frac{1}{kfrcs} \end{aligned}$$

[1]All the characteristic times for atomic processes are extracted from ADAS data and defined in subroutine iztau.d6a.

$$
\begin{aligned}
&= n_e < \sigma v >_{rec} \\
kprcs &\equiv \frac{taurec}{tauch} \\
&= \frac{< \sigma v >_{rec}}{(< \sigma v >_{iz} + < \sigma v >_{rec})}
\end{aligned}
\tag{A.1}
$$

.

A.1.1 Ionization and Momentum Transfer Collision of Neutrals

Atomic process of the impurity neutral in DIVIMP includes ionization and momentum transfer collision (MTC). The MTC event deflects the neutral trajectory by 90^o co-/counter-clock wise. kpizs is the probability of the impurity neutral ionzation and kpmtc (defined as $n_e < \sigma v >_{MTC}$) is the probability of the momentum transfer collision between the impurity neutral and the background plasma. Determination of the state change of the impurity neutral is made in similar way as in the case of the ions with the kprcs replaced by kpmtc :

1. Draw a random number, ξ, unfiormly distrubtedin [0,1]
2. When $\xi <$ kpchs, the state change occurs
3. If kpmtc $\leq \xi <$ kpizs, then the ionization occurs
4. If $\xi <$ kpmtc , then the MTC occurs

For the calculation of the MTC frequency ($< \sigma v >_{mtc}$), K. Predrag's model[55] is used instead of the default model in DIVIMP. Figure A-1 shows the relative value of the MTC rate for Ar-D^+ and Ar-D^o as the function of the deuterium energy. Predrag's data was fitted in this plot using exponential functions.

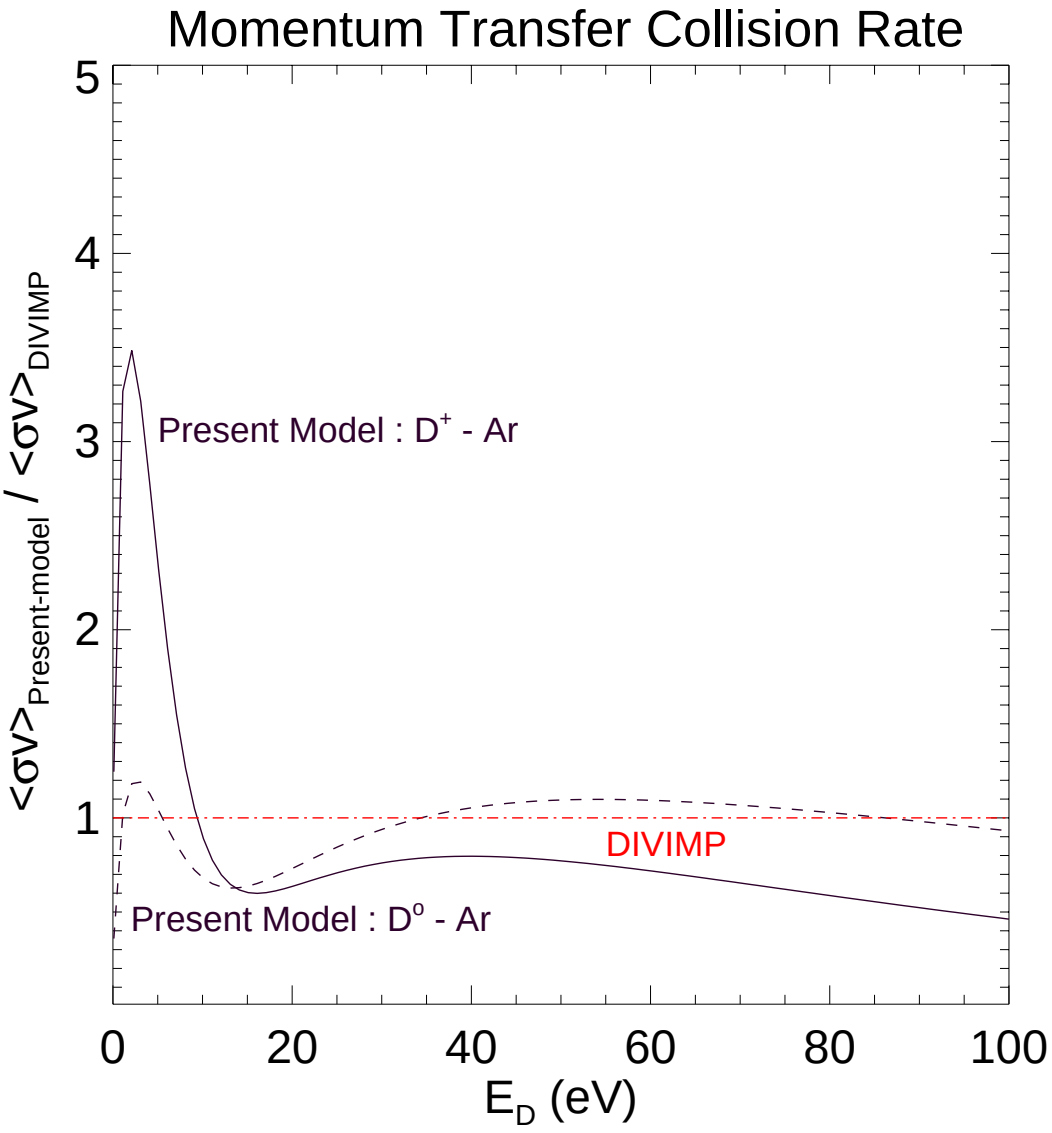

Figure A-1: Comparison of the MTC (Momentum Transfer Collision) rate between the DIVIMP calculation and Predrag's model.

Appendix B

Impurity Ion Transport

B.1 List of Parameters Used for Ion Transport Description

- (r, z) : the reference coordinate used for the grid plot, calculation of the neutral's location, and the estimation of the ion's approximate position.
- ik : the grid cell index in poloidal direction (ik increases from 1 at the inner target to the maximum at the outer target).
- ir : the grid cell index in radial direction (ir increases from 1 at the inner most core grid to the maximum at the outer most SOL or PFZ).
- $s(m)$: parallel distance along the field line (e.g., $s = 0$ at the inner target and $s = L_c$(connection length) at the outer target in the SOL region).
- $cross(m)$: the radial distance from the cell center line (so called s-line).
- $theta, \theta$: an arbitrary parameter specified in the code for an estimation of the ion's location in a cell[1].
- $kss(ik, ir)$: $s(m)$ of the center of the cell (ik,ir).

[1]The ion's transport in DIVIMP is determined with the parameters, $s, cross$ and θ. The (r, z) value is used only for a diagnostic purpose.

- $ksb(ik, ir)$: $s(m)$ of the end face of the cell (ik,ir) in parallel direction. ksb of the last cell (max(ik)) is equivalent to the connection length of the corresponding flux ring.
- $\theta_g(ik, ir)$: θ of the center of the cell (ik,ir).
- $distin(ik, ir)(m)$: the reference radial distance from the cell center to the cell face adjacent to the cell (ik,ir-1).
- $distout(ik, ir)(m)$: the reference radial distance from the cell center to the cell face adjacent to the cell (ik,ir+1)[2].
- upside(ik,ir) : the boundary between the cell (ik,ir) and the cell (ik-1,ir)
- downside(ik,ir) : the boundary between the cell (ik,ir) and the cell (ik+1,ir)
- inside(ik,ir) : the boundary between the cell (ik,ir) and the cell (ik,ir-1)
- outside(ik,ir) : the boundary between the cell (ik,ir) and the cell (ik,ir+1)

The ion's parallel shift from cell to cell is determined with the parameters s and ksb and the perpendicular shift is determined with the parameters $cross, distin, distout$ and $theta$. Fig. B-1 illustrates how the parameters listed above are defined. Although the DIVIMP code never uses the (r, z) value for ion's transport[3], the code uses it for the estimation of the approximate (r, z) position mapping to $(s, cross)$ position in the subroutine getrz. The subroutine getrz returns the value of (r, z) with $cross = 0$ assumed, i.e. the ion's position always locates on the cell center line(marked by X in Fig. B-1). The getrz with the real value of $cross$ gives the ion's approximate real position (r_r, z_r) (marked by a dot-circle in Fig. B-1).

[2]For a rectangular grid(orthogonal), $distin+distout = cellwidth$, and $ksb(ik, ir)-ksb(ik-1, ir) = cellheight$. This is not, however, true for the non-orthogonal grid case.

[3]David Elder's note

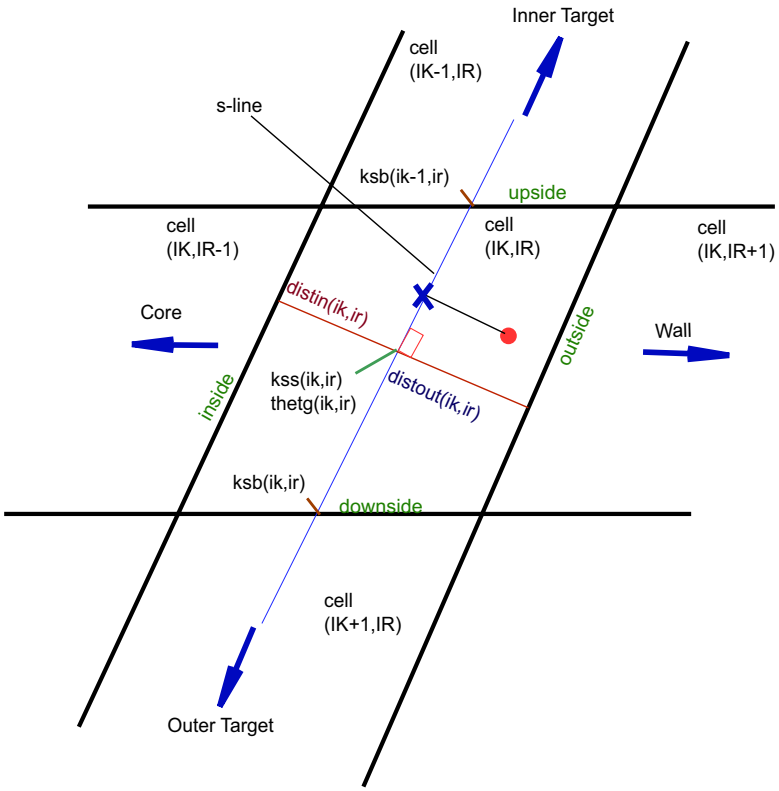

Figure B-1: The parameters used to describe the cell grid and to determine the ion transport in DIVIMP.

B.2 Algorithm of Impurity Ion Transport Calculation

Below is a brief description of the process that the div routine uses to determine the impurity ion transport.

a. An impurity neutral is ionized at (r, z)

b. The subroutine getscross_approx(r,z,s,cross,ik,ir) is called to find the approximate location in $(s, cross)$ coordinate corresponding to the given position in (r, z) coordinates in the cell (ik,ir).

c. Once s is found, then $theta(ik, ir)$ is calculated. From this stage, only the parameters, $s, cross$ and $theta$ are used to determine the transport of impurity ion.

d. The code updates $s(m)$ and $vel(m/sec)$ of the impurity ion. Then it checks if the particle strikes the divertor target. If this ion hits the target, the particle is stored as a recycling neutral to be launched later in neut (in this case code begins to follow a new ion).

e. If the ion does not hit the target, then the code stores (ik,ir) of the ion as (ikcheck, ircheck). Subroutine update_cross(ikcheck, ircheck, ...ik, ir, kflag, rflag, ..) is called to update cell index (ik and ir), and parameters such as $theta, cross$ and s.

f. The code checks if the ion crosses a cell boundary using subroutine impflux(ikcheck,ircheck,..,ik,ir,kflag,rflag,..) [4]. Here, the code checks if the current particle reaches the wall (the target recycling check is conducted in the stage d). If this ion reaches the wall, then the code stops following this particle and stores it as a recycling particle.

[4]This subroutine is added by T. Chung, 2003

g. Only the particles which do not strike the target/the wall reach this point and contribute to the increment of $ddlims(ik, ir, iz)$. This array is converted into the number density in DIVIMP at the end of the run.

h. After updating the array $ddlims$, the code checks if the ion experiences ionization or recombination. Subroutine launch_one is called to follow the recombined neutral until it is re-ionized. After finding the approximate values of s and $cross$ of re-ionized particle with getscross_approx, it continues the ion transport without being counted as a recycling event.

i. Continues the following of ions returning to step d.

Summary of the above procedures is represented in the flow chart of Fig. B-2

B.2.1 Descriptions of the Subroutines Associated with Ion Transport

In this section, a detailed review of the subroutines for impurity ion transport is made.

Subroutine getscross_approx

The main routine for the impurity neutral transport, neut, stores the ionization location of each impurity neutral in (r, z) coordinates. As the code uses $(s, cross)$ coordinates for the ion transport, a method that maps (r, z) to $(s, cross)$ is needed in the beginning of the ion transport procedure. The first thing that div, the main routine for the impurity ion transport, performs is to transform the initial position of an ion in (r, z) coordinate into $(s, cross)$ coordinate by calling the subroutine getscross_approx.

This routine estimates the approximate value of $(s, cross)$ corresponding to the position of the ion given in (r, z) in a cell (ik,ir). In a rectangular cell the mapping between the (r, z) coordinate and the $(s, cross)$ coordinate is simple. For example, the $(s, cross)$ of the ion at (r, z) can be calculated simply by $s = s_o + |z - z_o|$ and

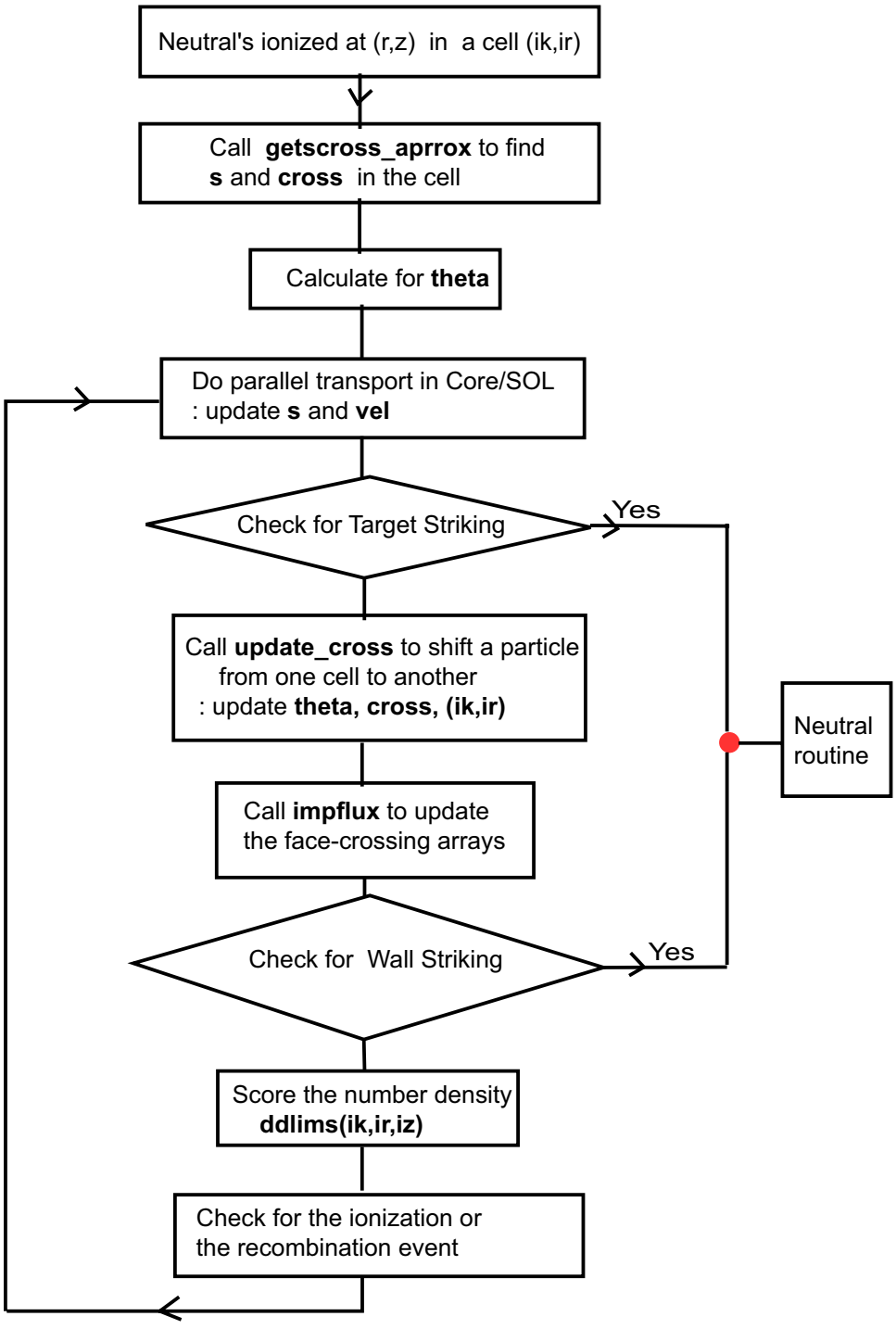

Figure B-2: The flow chart of ion transport routine, div.

$cross = |r - r_o|$ as shown in Fig. B-3 (a). This is not the case, however, for the non-orthogonal grid used in this study. The principle of calculating $(s, cross)$ in the non-orthgonal system is to recursively quarter the given cell along two major axes of the cell, one connects the center points of up/down-side of the cell, i.e. the s-line in parallel direction and another connects the center points of in/out-side of the cell in radial direction. As the cell is divided into a smaller section, the parameters $sfrac$ and $crossfrac$ is updated at the n_{th} iteration stage in the following way:

$$\begin{aligned} sfrac &= sfrac \pm 0.5^n \\ crossfrac &= crossfrac \pm 0.5^n \end{aligned} \tag{B.1}$$

Both the parameters, $sfrac$ and $crossfrac$, start with 0.0. Finally, the subroutine returns the approximate values of s and $cross$ as:

$$s = \begin{cases} kss(ik,ir) + sfrac(ksb(ik,ir) - kss(ik,ir)) & : \quad sfrac \geq 0 \\ kss(ik,ir) + sfrac(ksb(ik,ir) - ksb(ik-1,ir)) & : \quad sfrac < 0 \end{cases} \tag{B.2}$$

$$cross = \begin{cases} crossfrac \cdot distin(ik,ir) & : \quad crossfrac \geq 0 \\ crossfrac \cdot distout(ik,ir) & : \quad crossfrac < 0 \end{cases} \tag{B.3}$$

Note that a positive $cross$ represents an inward shift of the ion in the radial direction and a negative an outward shift. Fig. B-3 (b) shows an example of finding $(s, cross)$ of a particle located at (r, z). A total of 3 iterations are taken to find the final value of $(s, cross)$. In this case, $sfrac = -0.5 - 0.5^2 + 0.5^3 = -0.625$. Therefore, $s = kss - 0.625(kss - ksb)$. And $crossfrac = -0.5 - 0.5^2 - 0.5^3 = -0.875$. The cross value is $-0.875(distout)$.

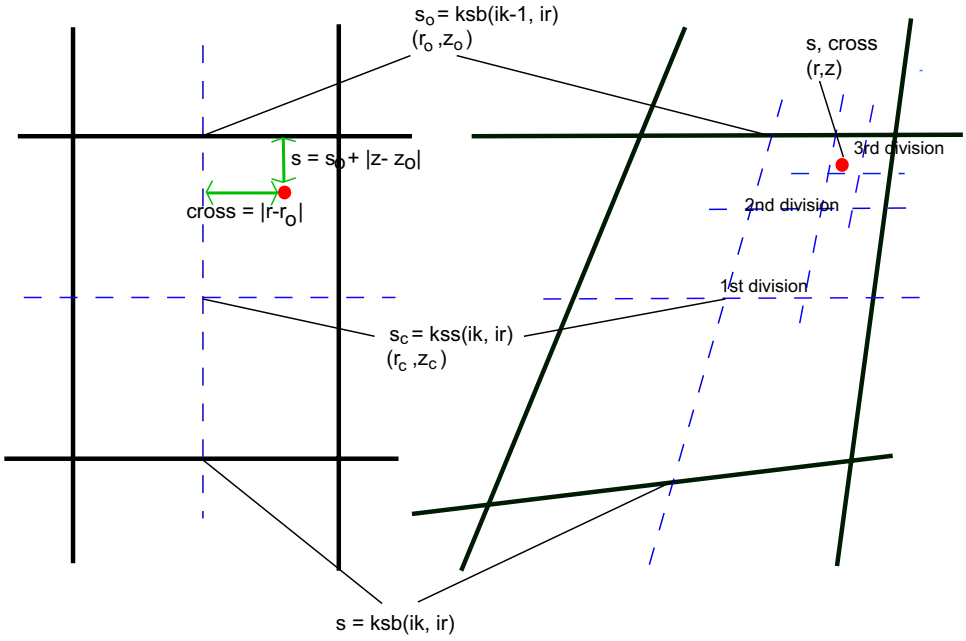

Figure B-3: Calculation of $(s, cross)$ of an ion located at (r, z). The calculations in an orthogonal system and a non-orthogonal system are compared.

Finding the parameter θ

Once the s parameter is found, the θ parameter is obtained by Eq. B-4.

$$\frac{\theta_g(ik,ir)-\theta}{kss(ik,ir)-s}=\frac{\Delta kss}{\Delta theta} \quad , \tag{B.4}$$

where $\Delta kss = kss(ik,ir)-kss(ik-1,ir)$ and $\Delta\theta = \theta_g(ik,ir)-\theta_g(ik-1,ir)$. Fig. B-4 shows the calculation of the parameter θ in case where the parameter s is greater than $kss(ik,ir)$.

The ion shift in the radial direction is made along the constant theta line (dashed line in Fig. B-4), i.e. the parameter θ of the ion remains constant during the radial transport.

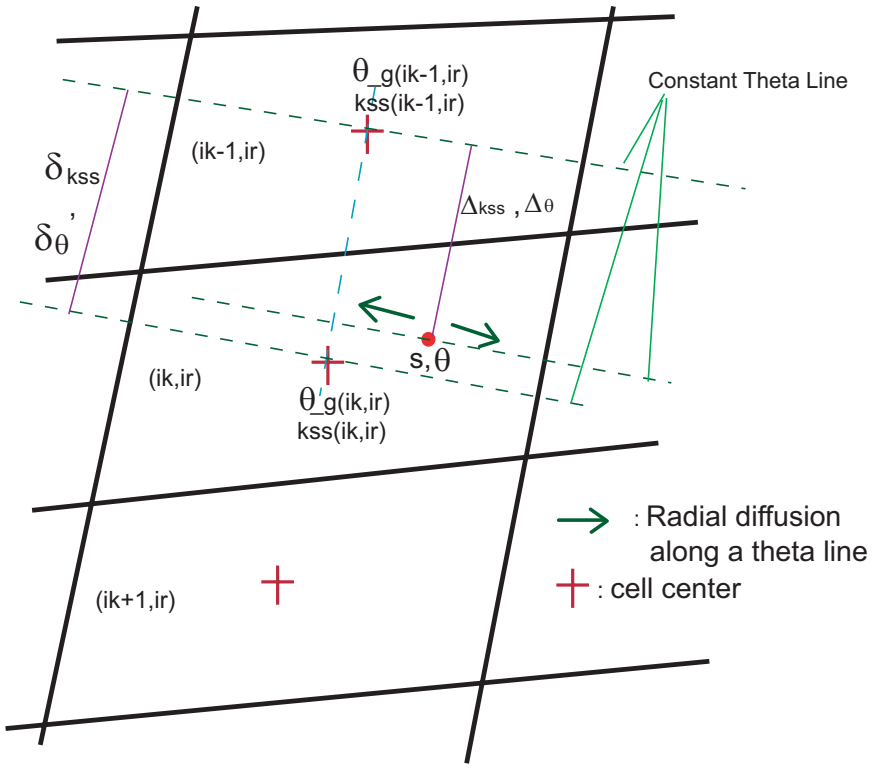

Figure B-4: The example of calculation of θ in the case of $s < kss(ik,ir)$.

Update s and vel

As the next step, the code calculates the changes in $s(m)$ and $vel(m/sec)$ due to the background plasma force acting on the impurity ion during the computational time step δt (usually, $\sim 0.1\mu sec$) as

$$
\begin{aligned}
s_{new} &= s_{old} + v_z^{old}\delta t + \frac{1}{2}\delta t^2 \frac{F}{m_z} && \text{(B.5)} \\
F &= \frac{m_z}{\delta t}\left(\frac{v_p - v_z^{old}}{\tau_s}\delta t + \sqrt{\frac{T_z}{m_z}}\sqrt{\frac{2\delta t}{\tau_{||}}} r_G + \frac{ZeE}{m_z} + \frac{\alpha_e}{m_z}\frac{dT_e}{ds} + \frac{\beta_i}{m_z}\frac{dT_z}{ds} \right) \\
&= \frac{m_z}{\delta t}\delta v_z && \text{(B.6)} \\
v_z^{new} &= v_z^{old} + \delta v_z && \text{(B.7)}
\end{aligned}
$$

The second term in parenthesis of the RHS of the force equation (A.6) is the diffusion in velocity space (i.e. the changes in v_z due to collisions between impurity ions and background plasmas), which substitues for the pressure gradient force[5]. Note that the parallel diffusion time $\tau_{||}$ is proportional to the impurity ion temperature, T_z. Thus the impurity ion temperature is cancelled out in this term.
At this point, DIVIMP checks if the ions strike the targets ($s = 0$ or $s = L_c$). If the ion reaches the divertor target, it ends its life and is stored as a recycling particle. The code then follows the next ion particle. Whether or not the updated s causes the change in ik will be checked later in the subroutine update_cross.

Subroutine update_cross

This subroutine returns a new set of the cell index (ik, ir) and stores the old one as $(ikcheck, ircheck)$.

a. The first process is to check if there is a change in the cell index ik due to the parallel transport, i.e. if updated s is greater than $ksb(ikcheck, ircheck)$ then ik is increased (the ion has moved forward or toward the outer target), or if

[5]P.C.Stangeby, Sec. 6.5.3, *The Plasma Boundary Of Magnetic Fusion Devices*

updated s is less than $ksb(ikcheck-1, ircheck)$ then ik is decreased (the ion has moved backward or toward the inner target).

Then a parameter $prekflag$ is recorded as $prekflag = ik - ikcheck$ to be used later in subroutine impflux

b. The $cross$ value is adjusted at the new cell based on the following relation

$$\frac{cross(ik, ircheck)}{cross(ikcheck, ircheck)} = \frac{dist(ik, ircheck)}{dist(ikcheck, ircheck)} \quad , \tag{B.8}$$

where $dist$ can be either $distin$ or $distout$.

c. The $cross$ (in unit of m) is updated with
$cross = cross \pm \sqrt{D_\perp \delta t}$.

d. Store the current value of (ik, ir) as $(ikold, irold)$ and then call the subroutine do_cfstep.

Subroutine do_cfstep

Subroutine do_cfstep determines if the particle moves to a new cell (ik, ir) due to the radial transport. If the updated $cross$(at step c) is greater than $distin(ikold, irold)$, then the particle moves radially inward (toward the core region), $irold \rightarrow ir = irold - 1$. If the $cross$ is less than $-distout(ikold, irold)$, then the particle moves radially outward (toward the wall region), $irold \rightarrow ir = irold + 1$. In non-orthogonal grid, cross field transport can cause a change in ik too, depending on s vlaue in the new cell (ik, ir) :

- If $s^{'} = kss(ikold, ir) - \frac{\theta_g(ikold, ir) - \theta}{\theta_g(ikold, ir) - \theta_g(ikold-1, ir)} \times (kss(ikold, ir) - kss(ikold - 1, ir))$ is less than $ksb(ikold - 1, ir)$, then the particle moves into the cell $ik = ikold - 1$.

- If $s' = kss(ikold, ir) + \dfrac{\theta - \theta_g(ikold, ir)}{\theta_g(ikold+1, ir) - \theta_g(ikold, ir)} \times (kss(ikold+1, ir) - kss(ikold, ir))$ is greater than $ksb(ikold, ir)$, then the particle moves into the cell $ik = ikold + 1$. In addition, for the calculation of face crossing, $kflag = (ik - ikold) + prekflag$ and $rflag = ir - irold$ is recorded here.

f. If ir has changed ($ir \neq irold$), then the s parameter is updated as either
$s = kss(ik, ir) - \dfrac{\theta_g(ik, ir) - \theta}{\theta_g(ik, ir) - \theta_g(ik-1, ir)} \times (kss(ik, ir) - kss(ik-1, ir))$ or
$s = kss(ik, ir) + \dfrac{\theta - \theta_g(ik, ir)}{\theta_g(ik+1, ir) - \theta_g(ik, ir)} \times (kss(ik+1, ir) - kss(ik, ir))$.

Appendix C

Approximation of Gas Leakage in DIVIMP Modeling

Alcator C-Mod has the intrinsic gas leakage from the divertor plenum to the main chamber. This intrinsic gas leakage occurs through the gaps provided by the gaps behind the mechanical structure. For example, some of the ports mounted around the machine vessel are used for the access of diagnostic instrument (called as *open ports* in Fig. C-1), which give rise to the intrinsic gas leakage. Approximate value of the intrinsic gas leak conductance is $\sim 20m^3/s$ [28]. The equivalent leakage area is, then, $\sim 0.08m^2$ for free-molecular. In addition to the intrinsic gas leakage (that can occur under normal operating conditions), additional gas leakage is added by opening the bypass flaps that are installed on the divertor. Total of 10 bypass flaps provide the gas leakage area of $\sim 0.08m^2$ which is comparable to the intrinsic gas leakage.

In DIVIMP modeling, the gas leakage is assumed to occur through the gaps uniformly distributed in toroidal direction (Fig. C-2). For the intrinsic gas leakage, the width of the gap is specified to $\delta_{leak} = 16mm$ which results in the equivalent gas leakage area of $2\pi R_c \delta_{leak} \sim 0.08m^2$ ($R_c = 0.76m$ is the major radius of the center of gas leak). For the open bypass model, the width of the gap is doubled.

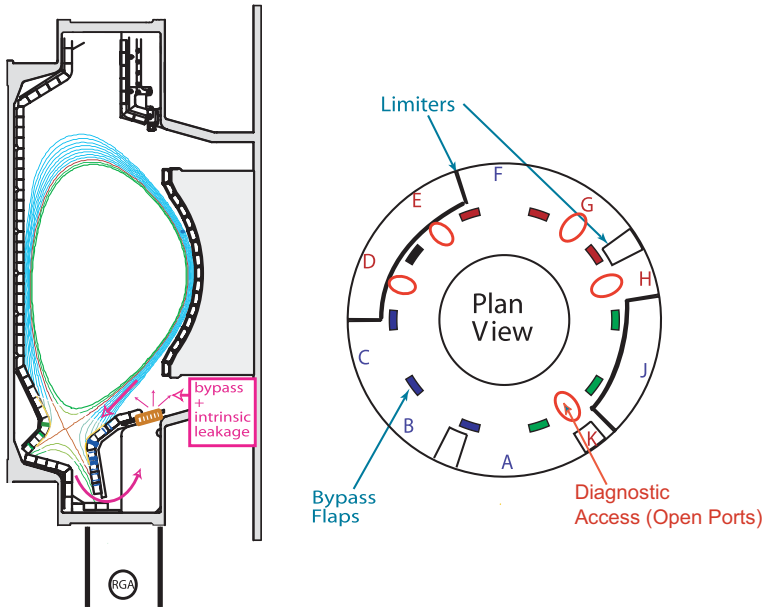

Figure C-1: Polidal and toroidal cross-sections of C-Mod. Diagnostic instruments are connected to D,E,G,H, and K ports. These open ports give rise to intrinsic gas leakages in C-Mod. Additional gas leakages occur when the bypass flappers are open.

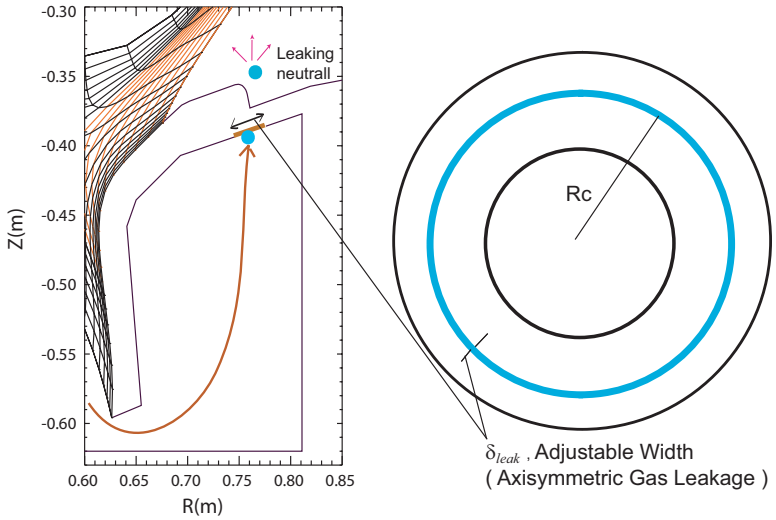

Figure C-2: DIVIMP modeling assumes axisymmetric gas leakage. Impurity neutrals in the plenum can leak through the specified line segment in to the main chamber. The width of the line segment can be adjusted.

Bibliography

[1] IPP Garching website
http://www.ipp.mpg.de/ippcms/eng/pr/fusion21/magnet/index.html

[2] John Wesson, *Tokamaks*, Clarendon Press, Oxford (1997)

[3] J. Roth, *Atmoic and Plasma-Material Interaction Processes in Controlled Thermonuclear Fusion*, Elsevier, Amsterdam (1993)

[4] D. E. Post, J. Nucl. Mater. 220-222 (1995) 143

[5] ITER official website, http://www.iter.org

[6] P. C. Stangeby and G. M. McCracken, Nucl. Fusion 30 (1990) 1225

[7] D. E. Post, R. Behrisch, and B. Stansfield, *Physics of Plasma-Wall Interactions in Controlled Fusion* pp.1-39, Plenum Press, New York (1986)

[8] I. H. Hutchinson, R. Boivin, F. Bombarda et al., Phys. Plas. 1 (1994) 1511

[9] M. V. Umansky, S. I. Krasheninnikov, B. Labombard, and J. L. Terry, Phys. Plasmas. 5 (1998) 3373

[10] J. L. Terry et al., Phys. Plasma 10 (2003) 1739

[11] M. Endler, J. Nucl. Mater. 266-269 (1999) 84

[12] B. A. Carreras, IEEE Trans. Plasma Sci. 25 (1997) 1281

[13] B. N. Rogers, J. F. Drake, and A. Zeiler, Phys. Rev. Lett. 81 (1998) 4396

[14] X. Q. Xu, R. H. Cohen, T. D. Rognlien, and J. R. Myra, Phys. Plasmas 7 (2000) 1951

[15] N. A. Uckan and the ITER Phsyics Group (compilers), *ITER Physics Design Guidelines*, IAEA, Vienna (1990)

[16] J. A. Goetz, B. Labombard, B. Lipschultz, et al., Phys. Plasmas 6 (1999) 1899

[17] A. Loarte, Plasma Phys. Control. Fusion 43 (2001) 183

[18] R. S. Granetz, G. M. McCracken, F. Bombarda, et al., J. Nucl. Mater. 241-243 (1997) 788

[19] G. M. McCracken, R. S. Granetz, B. Lipschultz, et al., J. Nucl. Mater. 241-243 (1997) 777

[20] J. A. Goetz, B. Lipschultz, C. S. Pitcher et al, J. Nucl. Mater. 266-269 (1999) 354

[21] Y. Wang, *A Study of Impurity Screening in Alcator C-Mod Plasmas*, Ph.D. Thesis, MIT (1996)

[22] J. Rice, et al., Rev. Sci. Inst. 66 (1995) 752

[23] R. A. Hulse, Nucl. Technol. Fusion 3 (1983) 259

[24] C. S. Pitcher, C. J. Boswell, T. Chung, et al., J. Nucl. Mater. 290-293 (2001) 812

[25] C. S. Pitcher, B. Labomard, R. Danforth, et al., Rev. Sci. Intr. 72, (2001) 103

[26] J. A. Goetz, et al., J. Nucl. Mater. 266-269 (1999)

[27] B. Lipschultz, B. Labombard, et. al., Plasma Phys. Control. Fusion 44 (2002) 733

[28] C. S. Pitcher, C. J. Boswell, et. al., Phys. Plasma 7 (2000) 1894

[29] J. A. Goetz, C. S. Pitcher, et. al., Nucl. Fusion 41 (2001) 1751

[30] P. C. Stangeby and J. D. Elder, J. Nucl. Mater. 220-223 (1995) 193

[31] P. C. Stangeby and J. D. Elder, *A guide to the DIVIMP code*, Univ. Toronto, 1995

[32] T. D. Rognlien et al., J. Nucl. Mater. 196-198 (1992) 347

[33] B. J. Braams, Technical Report 68, Next European Torus (1987)

[34] R. Simonini, G. Corrigan et al., Plasma Phys. 34 (1994) 368

[35] P. C. Stangeby, *The Plasma Boundary of Magnetic Fusion Devices*, IoP (2000) Bristol and Philadelphia

[36] L. L. Lao, J. R. Ferron et al., Nucl. Fusion 30 (1990) 1035

[37] R. Schneider, B. J. Braams, D. Reiter et al., Contrib. Plasma. Phys. 32 (1992) 450

[38] P. H. Summers, Atomic Data and Analysis Structure, JET, 1994

[39] L. Spitzer, *Physics of Fully Ionized Gases, 2nd ed*, New York, 1962

[40] W. Eckstein and H. Verbeek, *Data Compendium For Plasma-Surface Interactions*, Nucl. Fusion (1984) 12

[41] Y. Lin, Private communcations in C-Mod (MIT)

[42] *Numerical Recipes in C*, Cambridge Univ. Press (1992)

[43] G. F. Matthews, J. Nucl. Mater. 220-222 (1995) 104

[44] D. A. Knoll, S. I. Krasheninnikov, et al., Phys. Plasma 3 (1996)

[45] S. I. Krasheninnikov, A. Yu. Pigarov, D. A. Knoll, et al., Phys. Plasmas 4 (1997) 1638

[46] B. LaBombard, Private communications in C-Mod (MIT)

[47] D. Reiter, J. Nucl. Mater. 196-198 (1992) 80

[48] EIRENE home page, http://www.eirene.de

[49] B. LaBombard, S. Gangadhara, B. Lipschultz, and C.S. Pitcher, J. Nucl. Mater. 313-316 (2003) 995

[50] S. Lisgo, Ph.D. Thesis, University of Toronto (2003)

[51] C. J. Boswell, J. L. Terry, B. LaBombard, B. Lipshultz and J. A. Goetz, J. Nucl. Mater. 290-293 (20010 556

[52] T. Chung, C. S. Pitcher, B. Labombard, B. Lipschultz, et al., J. Nucl. Mater. 313-316 (2003) 990

[53] D. P. Stotler, B. LaBombard, V. A. Soukanovskii, et al., submitted to the 16th PSI conference (published to J. Nucl. Mater. in 2005)

[54] B. Lipschultz, D. Pappas, B. Labombard, J. Rice, D. Smith, S. Wukitch, Nucl. Fusion 41 (2000) 585

[55] K. Predrag, D. Schultz, T. Chung, Phys. Plasmas 10 (2003) 869

[56] 2003 APS Poster, http://www.psfc.mit.edu/people/labobmard/2003APS_Poster.pdf